

The Pennsylvania State University  
The Graduate School  
Department of Civil and Environmental Engineering

**DYNAMIC RESPONSE OF OVERLAY PAVEMENT DUE TO MOVING LOAD**

A Thesis in  
Civil Engineering  
by  
Xi Luo

© 2016 Xi Luo

Submitted in Partial Fulfillment  
of the Requirements  
for the Degree of

Master of Science

May 2016

The thesis of Xi Luo was reviewed and approved\* by the following:

Shelley Stoffels  
Professor of Civil Engineering  
Thesis Advisor

Farshad Rajabipour  
Associate Professor of Civil Engineering

Hai Huang  
Assistant Professor of Engineering

Patrick Fox  
Department Head of Civil and Environmental Engineering  
John A and Harriette K Shaw Professor

\*Signatures are on file in the Graduate School

## ABSTRACT

A full-scale accelerated pavement test on unbonded concrete overlays was conducted in 2006 to 2009, sponsored by the IPRF (Innovative Pavement Research Foundation), and performed at the Federal Aviation Administration (FAA) National Airfield Pavement Test Facility (NAPTF). Extensive strain gage data was collected by embedded strain gages both in the overlay and the underlay, due to tridem dual and tandem dual axle loads in a controlled distribution of wander paths. It provided new data and information, which has been used in this work to develop a concrete overlay pavement model in a manner that was not done before.

A semi-analytical model was conducted in this thesis to simulate dynamic behavior, specifically designed for airfield concrete overlay pavements, with consideration of multi-axle moving loads. Within the concrete overlay pavement model, interface condition is important to define. The interface conditions, from fully bonded to fully unbonded conditions, have a significant influence on dynamic responses of the pavement system, especially for the overlay and the underlay, and may also affect the corresponding performance and serviceability of pavement. . By using  $K_s$ , the shear reaction modulus, the interlayer could be seen virtually with its function remaining such that its shear stress could be obtained by multiplying  $K_s$  by relative displacement between overlay and underlay. All the bonding conditions could be described by relative displacement; when there is no relative displacement, the shear stress between the overlay and the underlay is also zero, which represents the unbonded condition. The fully bonded condition and partially bonded condition have similar mechanism. Characterization of load is another important factor affecting dynamic responses, so the loads were simulated as uniform constant pressure and harmonic load, respectively. In addition, the viscosity property of pavement layers below the underlay was considered in the model.

Governing equations were compiled for overlay and underlay from equilibrium relations. To get an analytical solution, Fourier Transform was performed. The closed-form of Inverse Fourier Transform seldom works out for complex kernel functions. Alternatively, one of the numerical methods, self-adaptive numerical integration algorithm, was tried and successfully worked for the final result, and reached agreement with examples in the literature. Then the model was verified with embedded strain gage data, after parameter study of  $K_s$ , harmonic load frequency and viscosity, and strain calculated by the model showed characteristics of strain history very clearly. The analytical model is effective and with good performance, which is much faster than numerical modeling. However, the particular analytical model in this thesis can only fit for a pavement system whose geometric shape is infinite plates. The fundamental approach is always appropriate; other constitutive models could be considered for further study, such as elasticity solutions under circular loaded area, rectangular loaded area, or strip loaded area.

## TABLE OF CONTENTS

List of Figures .....	vii
List of Tables .....	ix
Acknowledgements.....	x
Chapter 1 INTRODUCTION AND LITERATURE REVIEW .....	1
1.1 PROBLEM STATEMENT .....	1
1.1.1 GENERAL BACKGROUND .....	1
1.1.2 POTENTIAL CONTRIBUTION TO OVERLAY DESIGN .....	2
1.2 LITERATURE REVIEW .....	3
1.2.1 RIGID PAVEMENT MODELS .....	3
1.2.2 LOAD MODELING .....	6
1.2.3 BONDING CONDITIONS .....	7
1.2.4 PARAMETER OBTAINED .....	12
1.2.5 NUMERICAL CALCULATION METHODS .....	13
1.2.6 RESULT ANALYSIS .....	16
1.3 CONCLUSION AND MODELING PLAN OVERVIEW .....	18
Chapter 2 FULL SCALE TEST OF CC4 .....	20
2.1 BASIC INFORMATION .....	20
2.2 PAVEMENT SECTION CONFIGURATION .....	21
2.3 INSTRUMENT LOCATIONS .....	22
2.4 PAVEMENT TESTS .....	23
2.4.1 HWD TEST.....	23
2.4.2 MOVING LOAD TEST.....	24
Chapter 3 ANALYTICAL MODELING.....	27
3.1 INTRODUCTION .....	27
3.2 GOVERNING EQUATION .....	28
3.2.1 KIRCHHOFF-LOVE ASSUMPTIONS.....	28
3.2.2 GEOMETRIC DEFORMATION RELATIONSHIP .....	29
3.2.3 CONSTITUTIVE RELATIONSHIP .....	30
3.2.4 GOVERNING EQUATION .....	32
3.3 ANALYTICAL SOLUTION .....	35
3.4 LOAD EXPRESSION .....	37
3.5 CONCLUSION .....	41
Chapter 4 COEFFICIENTS BACKCALCULATION AND NUMERICAL SOLUTION .....	43

4.1 INTRODUCTION .....	43
4.2 PARAMETERS OBTAINED AND BACKCALCULATION .....	45
4.2.1 GEOMETRIC PARAMETERS .....	45
4.2.2 MECHANICAL PARAMETERS .....	46
4.3 NUMERICAL METHODOLOGY AND ITS VALIDATION.....	53
4.3.1 METHODOLOGY .....	56
4.3.2 VERIFICATION WITH EXAMPLE.....	57
4.4 NUMERICAL CALCULATION ANALYSIS .....	60
4.4.1 PARAMETER STUDY OF $K_s$ .....	61
4.4.2 PARAMETER STUDY OF LOAD FREQUENCY .....	66
4.4.3 PARAMETER STUDY OF VISCOSITY .....	69
4.4.4 ACCORDANCE CHECK.....	70
Chapter 5 CONCLUSION .....	74
5.1 SUMMARY .....	74
5.2 DISCUSSION AND RECOMMENDATION .....	75
REFERENCES .....	77
APPENDIX A STRAIN GAGE LOCATIONS .....	81
APPENDIX B STRAIN GAGE AND CALCULATED RESPONSES .....	82
APPENDIX C STRAIN GAGE AND CALCULATED RESPONSES .....	88
APPENDIX D MATLAB CODE SAMPLE.....	99

## LIST OF FIGURES

Figure 1-1 General Models .....	6
Figure 1-2 Two Models Simulated Concrete Layer as Slabs.....	9
Figure 2-1 End View and Side View of Baseline Experiment Design Configuration by Stoffels [21].....	21
Figure 2-2 Overlay Deformation with Vertical Load by Singh [27] .....	23
Figure 2-3 Gear Configurations by Stoffels [21] .....	24
Figure 2-4 Wander Patterns by Stoffels [21] .....	25
Figure 2-5 Embedded Strain Response History Example by Stoffels [21].....	26
Figure 3-1 Stress States Within Free Body Of Overlay .....	31
Figure 3-2 Equilibrium of Plate (Overlay) Element .....	33
Figure 3-3 Loading Positions of Wanders by Stoffels [21] .....	38
Figure 3-4 Geometry of Gear Configuration .....	38
Figure 4-1 Stress Distribution along Moving Axle.....	59
Figure 4-2 Stress Distribution along Moving Axle, from Kim [7] .....	60
Figure 4-3 Numerical Investigation Flow Chart .....	61
Figure 4-4 Parameter Study of Ks with the other Parameters as shown in Table 4-11 with Constant Load .....	62
Figure 4-5 Data of EG-O-N1-1 T, randomly selected track 0 pass on 7/25/2006 (embedded gage, overlay, test item N1, gauge 1, top of slab) .....	63
Figure 4-6 Data of EG-O-N1-2 T, randomly selected track 0 pass on 7/25/2006 (embedded gage, overlay, test item N1, gauge 2, top of slab) .....	63
Figure 4-7 Data of EG-O-N1-3 T, randomly selected track 0 pass on 7/25/2006 (embedded gage, overlay, test item N1, gauge 3, top of slab) .....	64
Figure 4-8 Model Result Corresponding to EG-O-N1-1 T.....	65
Figure 4-9 Model Result Corresponding to EG-O-N1-2 T.....	65
Figure 4-10 Model Result Corresponding to EG-O-N1-3 T.....	66

Figure 4-11 Dynamic Responses Due to Harmonic Loads with Different Frequencies (unit Hz) .....	67
Figure 4-12 Model Result Corresponding to EG-O-N1-1 T .....	67
Figure 4-13 Model Result Corresponding to EG-O-N1-2 T .....	68
Figure 4-14 Model Result Corresponding to EG-O-N1-3 T .....	68
Figure 4-15 Strain Varies with $c$ when $K_s=1.0E+8$ .....	69
Figure 4-16 Strain Varies with $c$ when $K_s=1.0E+12$ .....	70
Figure 4-17 Loading Plan and Coordinate Set by Yeh [22].....	71
Figure B-1 Data of EG-O-S1-1 B, randomly selected track 0 pass on 7/25/2006 (embedded gage, overlay, test item S1, gauge 1, bottom of slab).....	82
Figure B-2 Data of EG-O-S1-2 B, randomly selected track 0 pass on 7/25/2006 (embedded gage, overlay, test item S1, gauge 2, bottom of slab).....	82
Figure B-3 Data of EG-O-S1-3 B, randomly selected track 0 pass on 7/25/2006 (embedded gage, overlay, test item S1, gauge 3, bottom of slab).....	83
Figure B-4 Model Result of EG-O-S1, randomly selected track 0 pass on 7/25/2006 (embedded gage, overlay, test item S1, bottom of slab) .....	83
Figure B-5 Data of EG-O-S1-1 B, randomly selected track 0 pass on 8/01/2006 (embedded gage, overlay, test item S1, gauge 1, bottom of slab).....	84
Figure B-6 Data of EG-O-S1-2 B, randomly selected track 0 pass on 8/01/2006 (embedded gage, overlay, test item S1, gauge 2, bottom of slab).....	84
Figure B-7 Data of EG-O-S1-3 B, randomly selected track 0 pass on 8/01/2006 (embedded gage, overlay, test item S1, gauge 3, bottom of slab).....	84
Figure B-8 Model Result of EG-O-S1, randomly selected track 0 pass on 8/01/2006 (embedded gage, overlay, test item S1, bottom of slab) .....	85
Figure B-9 Data of EG-O-S1-1 B, randomly selected track 0 pass on 8/09/2006 (embedded gage, overlay, test item S1, gauge 1, bottom of slab).....	86
Figure B-10 Data of EG-O-S1-2 B, randomly selected track 0 pass on 8/09/2006 (embedded gage, overlay, test item S1, gauge 2, bottom of slab).....	86
Figure B-11 Data of EG-O-S1-3 B, randomly selected track 0 pass on 8/09/2006 (embedded gage, overlay, test item S1, gauge 3, bottom of slab).....	86
Figure B-12 Model Result of EG-O-S1, randomly selected track 0 pass on 8/09/2006 (embedded gage, overlay, test item S1, bottom of slab) .....	87



Figure C-1 Data of EG-O-N1-1 T, randomly selected track 0 pass on 7/25/2006 (embedded gage, overlay, test item N1, gauge 1, top of slab) .....	88
Figure C-2 Data of EG-O-N1-2 T, randomly selected track 0 pass on 7/25/2006 (embedded gage, overlay, test item N1, gauge 2, top of slab) .....	88
Figure C-3 Data of EG-O-N1-3 T, randomly selected track 0 pass on 7/25/2006 (embedded gage, overlay, test item N1, gauge 3, top of slab) .....	89
Figure C-4 Model Result of EG-O-N1, randomly selected track 0 pass on 7/25/2006 (embedded gage, overlay, test item N1, top of slab).....	89
Figure C-5 Data of EG-O-N2-1 T, randomly selected track 0 pass on 7/25/2006 (embedded gage, overlay, test item N2, gauge 1, top of slab) .....	90
Figure C-6 Model Result of EG-O-N2, randomly selected track 0 pass on 7/25/2006 (embedded gage, overlay, test item N2, top of slab).....	90
Figure C-7 Data of EG-O-N3-1 T, randomly selected track 0 pass on 7/25/2006 (embedded gage, overlay, test item N3, gauge 1, top of slab) .....	91
Figure C-8 Data of EG-O-N3-2 T, randomly selected track 0 pass on 7/25/2006 (embedded gage, overlay, test item N3, gauge 2, top of slab) .....	91
Figure C-9 Data of EG-O-N3, randomly selected track 0 pass on 7/25/2006 (embedded gage, overlay, test item N3, top of slab) .....	92
Figure C-10 Data of EG-O-S1-2 T, randomly selected track 0 pass on 7/25/2006 (embedded gage, overlay, test item S1, gauge 2, top of slab).....	93
Figure C-11 Data of EG-O-S1-3 T, randomly selected track 0 pass on 7/25/2006 (embedded gage, overlay, test item S1, gauge 3, top of slab).....	93
Figure C-12 Data of EG-O-S1, randomly selected track 0 pass on 7/25/2006 (embedded gage, overlay, test item S1, top of slab) .....	94
Figure C-13 Data of EG-O-S2-1 T, randomly selected track 0 pass on 7/25/2006 (embedded gage, overlay, test item S2, gauge 1, top of slab).....	95
Figure C-14 Data of EG-O-S2-2 T, randomly selected track 0 pass on 7/25/2006 (embedded gage, overlay, test item S2, gauge 2, top of slab).....	95
Figure C-15 Data of EG-O-S2-3 T, randomly selected track 0 pass on 7/25/2006 (embedded gage, overlay, test item S2, gauge 3, top of slab).....	95
Figure C-16 Model Result of EG-O-S2, randomly selected track 0 pass on 7/25/2006 (embedded gage, overlay, test item S2, top of slab) .....	96
Figure C-17 Data of EG-O-S3-1 T, randomly selected track 0 pass on 7/25/2006 (embedded gage, overlay, test item S3, gauge 1, top of slab).....	1

Figure C-18 Data of EG-O-S3-2 T, randomly selected track 0 pass on 7/25/2006 (embedded gage, overlay, test item S3, gauge 2, top of slab).....	1
Figure C-19 Data of EG-O-S3-3 T, randomly selected track 0 pass on 7/25/2006 (embedded gage, overlay, test item S3, gauge 3, top of slab).....	97
Figure C-20 Data of EG-O-S3, randomly selected track 0 pass on 7/25/2006 (embedded gage, overlay, test item S3, top of slab) .....	98

## LIST OF TABLES

Table 1-1 Parameters of Example.....	15
Table 2-1 Baseline Experiment Measured Thicknesses and Loading Configurations by Stoffels [21].....	22
Table 2-2 Starting Position of Each Track by Stoffels [21].....	25
Table 2-3 Loading Sequence by Stoffels [21] .....	26
Table 4-1 Geometric Parameters (mm).....	45
Table 4-2 CC4 Construction Schedule by Stoffels [21] .....	48
Table 4-3 BAKFAA Baseline Experiment Seed Moduli by Stoffels [21].....	48
Table 4-4 Moduli from HWD Testing on Underlay .....	49
Table 4-5 Moduli of Pavement System (Test Item N1).....	49
Table 4-6 Moduli of Pavement System (Test Item S1) .....	50
Table 4-7 Moduli of Pavement System (Test Item N2).....	50
Table 4-8 Moduli of Pavement System (Test Item S2) .....	51
Table 4-9 Moduli of Pavement System (Test Item N3).....	51
Table 4-10 Moduli of Pavement System (Test Item S3) .....	52
Table 4-11 Masses of Overlay and Underlay.....	52
Table 4-12 Parameters Provided by Kim [7] .....	58
Table 4-13 Parameter Values (7/25/2006, Test Item N1) .....	61
Table 4-14 Wander Pattern and Load Centerline of Every Track by Yeh [22] .....	71
Table 4-15 Comparison between Calculated Results and Overlay Bottom Strain for Test Item S1, with Varied Dates .....	72
Table 4-16 Comparison between Calculated Results and Strain of Every Item of Date 7/25/2006 .....	73

## ACKNOWLEDGEMENTS

Two years studying in PSU means a lot to me.

I learned to study as a graduate student in a field I was not that familiar with before, and not in my native language; I paid a lot, now I can say I am professional. And I also become a person who will never be easily depressed and can manage things more ordered and efficiently than before. All of these achievements can't be reached without the help of my professors, special thanks to Dr. Stoffels.

I also would like to thank Jeanne Michel and Charles Michel, who gave me a lot of encouragements when I really wanted to give up. And certainly thank my parents who always give me full love and support, also my friends, classmates, and Dr. Yeh Lin, who helped me in data analysis part.

## **Chapter 1 INTRODUCTION AND LITERATURE REVIEW**

### **1.1 PROBLEM STATEMENT**

#### **1.1.1 GENERAL BACKGROUND**

Airfield pavement evaluation and rehabilitation design procedures have continued to progress over the past several decades. Because of the need for smoothness, high skid resistance and absence of debris, overlays, including bonded overlays and unbonded overlays on rigid pavement or on flexible pavement, have many applications in the airfield pavement field. Overlay types and performance have thus been studied by many researchers. Unbonded concrete overlays, which are the focus of this research, refer to a type of pavement which has another concrete slab laid on the previous rigid pavement, in order to extend the serviceability of pavement with relatively less cost compared to that of rebuilding a new one, while still providing an entirely new concrete surface.

IPRF (Innovative Pavement Research Foundation) Project FAA-01-G-002-04-2 and Project IPRF 06-03 included full-scale testing conducted during 2006 through 2009, and were mainly concentrated on identification of the factors which have a large effect on the performance of airfield unbonded concrete overlays. The accelerated full-scale testing was conducted indoors at the FAA (Federal Aviation Administration) NAPTF (National Airfield Pavement Testing Facility), which collected both performance data, in terms of observed distress, and pavement responses as measured by instrumentation, with consideration of the interaction among pavement, load and environment factors such as moisture and temperature. There were several graduate theses, papers and project reports based on the data obtained from IPRF Projects FAA-01-G-002-

04-2 and 06-03. As of August 2015, the FAA is currently constructing additional test items at the NAPTF to complete the experiment prior to incorporation of the results into design procedures. Among the available sets of data, many of them could be used to investigate the distresses of pavement, and then to predict service year or improve understanding of overlay pavement. Strain data, which can be used to study the characteristics of stress distribution and stress pattern due to aircraft loads, provides a source of data for verification of modeling.

Modeling is an important branch of applications of full-scale accelerated pavement test (f-sAPT); there are types of models used for backcalculation, deflection analysis, stress and strain, fatigue, and pavement serviceability. With regard to mechanical analysis, elastic layer theory and finite element method have been the first choices [1]. This at least demonstrates that there is still modeling we can do to break the limitations which may appear in models mentioned in the literature review which follows. On the other hand, additional investigations, which hadn't been involved in f-sAPT, could be completed based on a reliable model. Further, such a model will potentially help with further research about unbonded overlays, but with different geometric design parameters. In conclusion, analytical modeling is reasonable to consider, both to validate and to further the understanding of the previous project, and to be a good tool for studying unbonded overlays. The preliminary development of such an analytical model is the objective of this thesis.

### **1.1.2 POTENTIAL CONTRIBUTION TO OVERLAY DESIGN**

There are two types of design methods could be used in airfield overlay pavement according to R.S. Rollings [3], Current Airfield Rigid Pavement Design and Improved Overlay Design, which could be defined as safe design and design predicting pavement performance. Both of them should use analytical modeling to calculate stress, strain and displacement within a

layered overlay system; a predictive performance model which is compatible with the analytical model will be established to evaluate the condition of pavement structure.

The basic thinking of safe design is to choose pavement thickness for some specific traffic amount and to keep the pavement below a predefined failure level in terms of slab cracking. The general procedure of safe design of rigid airfield pavements is to have a trial thickness of pavement, use an analytical model to calculate the tensile stress at the bottom of concrete slab, and then to utilize a fatigue relationship (stress/flexible strength vs. coverages or failure cycle curve). Finally, based on calculated stress and fatigue levels, the failure requirements should be checked; if not met, the trial thicknesses should be modified.

## **1.2 LITERATURE REVIEW**

All the literature resources reviewed here are focused around modeling of concrete unbonded overlays. For configuration of the unbonded overlay in the full-scale testing, material properties, load conditions and other details, the related information will be specified in the next chapter about experiment introduction. All the references utilized in the literature review will be mentioned in the chronological sequence of model conducting.

### **1.2.1 RIGID PAVEMENT MODELS**

Until now there has seldom been a direct overlay pavement model, but many of the rigid pavement models which are directly related to concrete overlays have been studied. The rigid pavement models in use, which can provide deflection, stress and strain calculations and so on, can be principally divided into two categories: FEM models and analytical models.

FEM is essentially a numerical method, and FEM models have been used relatively more frequently than any other models. For example, a commonly used computer program, EverFE (David and Mahoney, 1999), is a three-dimensional (3-D) finite element analysis software, which considers rigid pavement as a three-layer system: slab, base and subgrade. Dowels across slab joints, multi-axle loads, an unbonded condition between slab and base, and a changing trend of temperature along pavement thickness can also be specified in EverFE. Another often-used software is Everstress, which also solves problems using 3-D FEM, but doesn't limit to only three layers of pavement system, and can handle a more detailed configuration as well as contact area of the tires of each axle. Besides these special software applications for pavements only, commercial software ABAQUS and ANSYS and so on have also been used by many of the previous researchers. For example, Darestani [2] used ANSYS to do dynamic analysis both on bonded and unbonded JPCP and JRCP.

On the other hand, analytical modeling has also been of interest to many researchers. The analytical models often regarded as the first for rigid pavements were the Westergaard models, which simulated the concrete pavement system as a thin elastic plate resting on a bed of independent springs. Using the Westergaard models, all responses of interior loaded, edge loaded, and corner loaded slabs could be worked out. Underlying support was assumed to come from the reaction modulus  $k$ , or the stiffness of these springs in the Westergaard models [3]. The subsequently developed layered elastic models could do more than Westergaard models, since they idealized the pavement system as a set of homogenous, elastic layers, with uniform thickness of each layer, but assumed infinite extent so they could only be used to characterize interior loading. Ioannides & Khazanovich [4] expanded Burmister's analytical solution to a general case in which each layer of pavement system was seen as a Burmister layer, Kirchhoff plate or Winkler spring bed, which is a spring system without dashpot-represented viscosity of layer. Sun [5] utilized a 1-D model of the concrete pavement system which was simulated as infinite Euler



beam on Kelvin foundation, which is a row of springs with a viscous damping term. Kim & Roesset [6] published a model which characterized rigid pavement as a plate on elastic foundation by using thin plate theory. Kim et al. then developed a 3-D model considering a plate on viscoelastic foundation [7]. Additionally, Zaman et al. [8] modeled the concrete pavement as a thick plate laid on viscoelastic foundation using an FEM algorithm, and for thick plate, the shear deformation within plane is not negligible. The common point of all of these models above was using a series of springs to replace layers below the concrete layer. Other models directly simulated the entire system below the concrete layer as a half-space, as Figure 1-1 shows. They were basically the discrete method and the continuous method, which treat the research objective to be several individual elements and an entire system to deal with dynamic problems. For the continuous method, a beam resting on elastic half space model was proposed by Dieterman and Metrikine [9]. Cai et al. [10] improved the half space characterization from elastic to poroelastic medium, which considered the interaction between soil and porous water when the model was subjected to dynamic loading. Cai et al. also changed the concrete layer model from a beam to a plate. To summarize, these two general kinds of models presented were all used effectively by researchers for concrete pavement modeling.

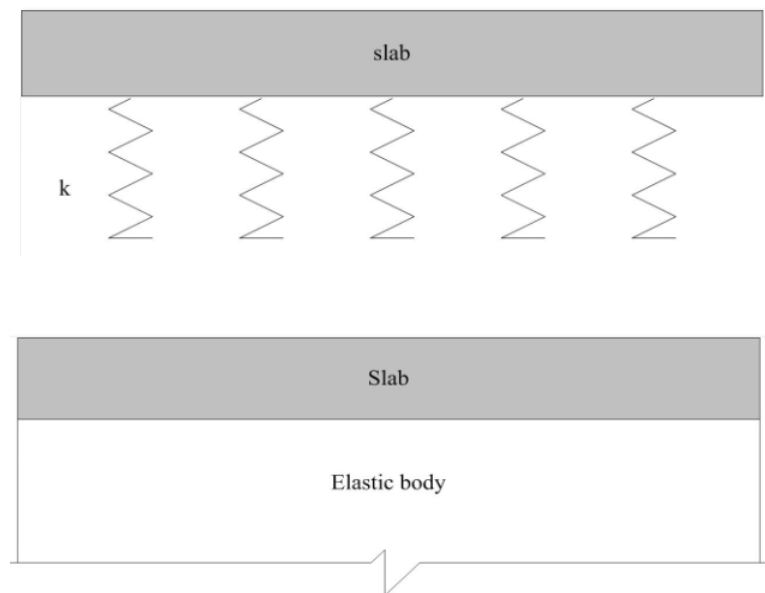


Figure 1-1 General Models

### 1.2.2 LOAD MODELING

Load modeling is another important part in the overall system model; according to different working situations, loads were mainly classified to be static or dynamic. In pavement tests, such as falling weight deflection tests, usually the load is considered to be a static load, ignoring the impulse effect. Static loads were also used in some of the earlier models, for the sake of simplicity. However, for the majority of working situations, dynamic loads of various kinds were of much more interest. Among all the dynamic loads, moving load models are the most appropriate to simulate vehicle loads, since cars, tracks and aircrafts always move along the pavement with different wander paths.

For moving loads, velocity is an important factor which should be considered. Some of the references listed previously [2], [6], [7], [10] all assumed the moving loads had a constant velocity or a sequence of ramp up velocities, and that the velocity of each pass was constant. In

terms of the characteristics of the moving load, the coordinate origin is fixed at some place on an axle.

There were mainly two approaches (concentrated load and pressure) to simulate moving load, one of them considered the moving load to be a concentrated load, line load, and the other used uniform pressure within rectangular area [11]. According to Kim [6], [7], [12], [13], the uniform pressure load form could also be divided into three kinds: constant load, harmonic load, and arbitrary amplitude variation load. All of them were verified to be reasonable to simulate traffic load under different situations. Additionally, combinations of load were also considered, for it was more practical for traffic load configurations; For example, tandem dual axle load was considered in many references such as [6], [7], [12], and dynamic responses were obtained both by direct method and superposition method. The latter superposition method is to calculate the dynamic response of each tire of each axle then accumulate them together, while the former direct method is to get the pressure caused by each tire of each axle, then calculate dynamic responses directly.

Yet another load form was suggested by Taheri et al. [14], who asserted that the deflection was caused by weight and inertia of aircraft and inertia of slab. Compared to the load models above, this model considered the inertia of aircraft, and aircraft was also simulated as a series of springs.

### **1.2.3 BONDING CONDITIONS**

This section will be developed following a logical sequence; the first aspect is how bonding conditions are usually considered in rigid pavement systems and overlay pavement systems, and its classification. Then, how analytical models are handled with consideration of

bonding conditions will be presented. Finally, the existing references will be listed about which analytical models consider perfect or imperfect bonding conditions in pavement systems.

Bonding conditions have not been much considered in analytical and numerical models of rigid pavement; they are usually seen as no bonding between layers, which is reasonable since materials of rigid pavement are almost all non-adhesive materials, and the interlock of particles could be ignored. However, for overlay pavement situations, bonding conditions seem to be important. There are three kinds of bonding conditions of overlay pavement, which are unbonded, partially bonded, and fully bonded overlays. An overlay is considered to be unbonded because no direct bond could be developed if a separator layer of asphalt concrete or other material is put between overlay and base slab (underlay). If a slab is cast on the base slab, it is considered as a partially bonded overlay. When the base slab surface is well treated by cold milling or other techniques and a bonding grout is used between base slab and overlay, the overlay is thought to be fully bonded [3]. These three bonding conditions, respectively, represent that relative horizontal movement happens between overlay and underlay with no radial stress between layers, less relative horizontal movement happens with more radial stress, and no horizontal movement happens with large radial stress in analytical models. During overlay construction in the f-sAPT project at NAPTF, there was a construction step to build an AC interlayer after underlay curing and before overlay placement. The AC interlayer was built about 1 inch thick and because of this interlayer, the pavement system was considered to be an unbonded overlay, making it necessary to consider an analytical model of overlay with bonding conditions.

Bonding conditions have significant effect on deformations of the layers connected by the bond, and their compatibility. There have been two fundamental approaches to consider deformation compatibility: equivalent slab and double slabs, which are shown in Figure 1-2 [3].

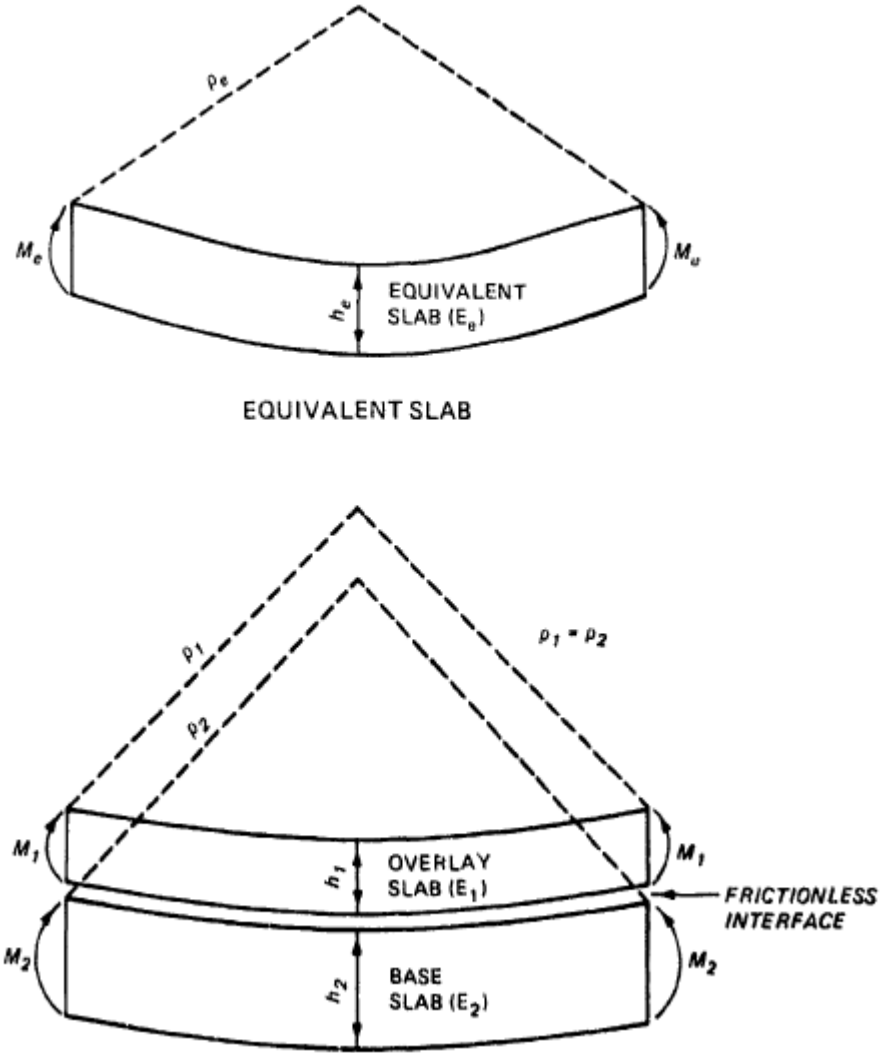


Figure 1-2 Two Models Simulated Concrete Layer as Slabs

Equivalent slab method means the overlay and underlay form a new slab which deforms equivalently to the two-layer slab system. According to Rollings [3], the curvature of the slab is obtained following simple beam theory:

$$\frac{1}{\rho_e} = \frac{M_e}{E_e I_e} \quad (1.1)$$

where  $\rho_e$ ,  $M_e$ ,  $E_e$ ,  $I_e$  are radius of curvature, moment, elasticity modulus and inertia moment of equivalent slab, respectively.

The equilibrium the pavement system should satisfy is:

$$M_e = M_1 + M_2 \quad (1.2)$$

where  $M_1, M_2$  are moments held by overlay and base slab, respectively.

Equations (1.1), and (1.2) alone are not enough to work out the solution of an overlay pavement system. To define equivalent slab, there are mainly three methods [3]:

i) Assuming equivalent slab rigidity equals to rigidities summation of overlay and underlay

$$E_e I_e = E_1 I_1 + E_2 I_2 \quad (1.3)$$

ii) Assuming equivalent tensile stress equals to tensile stress of base slab

$$\sigma_e = \sigma_2 \quad (1.4)$$

iii) Assuming equivalent tensile stress equals to tensile stress of overlay

$$\sigma_e = \sigma_1 \quad (1.5)$$

where the variables with subscript  $e, 1, 2$  represent the equivalent slab, overlay and base slab, respectively. With aforementioned relationships and some additional ones not listed by Rollings [3], equivalent stress could be calculated, and so also the stresses of overlay and base slab.

However, the bonding conditions seem to be not very clear in these equivalent slab models. In Tompkins et al. [15], a concept of slab equivalence was used to reduce bonded PCC-base or PCC-PCC-base pavement to a single slab with equivalent thickness. Taking PCC-base for example, this equivalent slab was determined by plate theory and relations proposed by Ioannides et al. [16]:

$$D_e = D_1 + D_2 \quad (1.6)$$

where  $D = \frac{Eh^3}{12(1-\nu^2)}$ , with the Poisson's ratio assumed as the same in all the slabs. Whether

equation (1.6) is accordance with (1.3) depends on where the neutral axle of the slab section is located. If there are full bonds between the PCC slabs, PCC and base performed together, neutral axis of the equivalent slab, which was evaluated from top of PCC, was:

$$x = \frac{\int_0^h E(z) z dz}{\int_0^h E(z) dz} = \frac{E_1 \frac{h_1^2}{2} + E_2 h_2 \left( \frac{h_2}{2} + h_1 \right)}{E_1 h_1 + E_2 h_2} \quad (1.7)$$

Equation (1.6) turns into

$$E_e h_e^3 = E_1 h_1^3 + E_2 h_2^3 + 12 \left[ E_1 h_1 \left( \frac{h_1}{2} - x \right)^2 + E_2 h_2 \left( h_1 + \frac{h_2}{2} - x \right)^2 \right] \quad (1.8)$$

where variables with subscript  $e$ , 1, 2 represent the equivalent slab, PCC and base slab, respectively. So the modulus and thickness could be worked out by equation (1.8); deflection, stress and stain could be obtained from plate theory and elasticity constitutive relationship.

On the other hand, the two slabs method is illustrated by the second diagram in Figure 1-2. The two slabs deform individually but with the same curvature, so a supplemental relationship other than equations (1.1) and (1.2) is:

$$\frac{1}{\rho} = \frac{M_1}{E_1 I_1} = \frac{M_2}{E_2 I_2} \quad (1.9)$$

For the unbonded condition, additional information is required. Also, for the partially bonded condition, the model couldn't be utilized as any of these because of the complexity. If overlay and underlay are simulated as two slabs, an imperfect bond between structures may provide some clues to an appropriate model; slip stiffness concept  $K$  was proposed by Girhammar et al.[17],

$$V = -K \Delta u \quad (1.10)$$

where  $V$  is the shear force between beam and column, and  $\Delta u$  is the relative horizontal displacement between beam and column. By assigning  $K = 0$ , there is no bond between members of a composite beam, while  $K = \infty$  means fully bonded.

There are similar concepts which have been applied in the pavement engineering field. According to Rollings [3], Westergaard proposed the basic method to estimate shear stress for overlay and underlay (the radial stresses), which is to consider the shear stress as a function of the

difference between the horizontal displacement of the layer directly above the interface and the layer directly below the interface. The program BISAR, which uses Westergaard approximation for interlayer conditions, performs well in layered pavement system [18]. Kruntcheva et al. [19] used BISAR to consider flexible pavement systems with unbonded, partially bonded, and full bonded condition between surface course and binder course. They assumed all the layers to be elastic bodies and compared the results from BISAR with those from an FEM program.

According to Hakim [20], equation (1.11) represents Goodman's constitutive law to describe the interface behavior,

$$\tau = K_s \Delta u \quad (1.11)$$

where,  $\Delta u$  is the relative horizontal displacement of the two faces at the interface.  $K_s$  is the horizontal shear reaction modulus at the interface. Although Kruntcheva [19], Hakim [20] considered only flexible pavements, the relationship could be used for overlay pavement because, first, this relationship doesn't refer to material properties but just the constitutive relationship, and second, all the materials were also seen as elastic bodies, which is what is typically assumed for rigid pavement.

#### 1.2.4 PARAMETER OBTAINED

Closed-form solutions usually can't be obtained because of the complexity of function; numerical solutions are used instead although they are approximation methods, which could be accurate if the numerical method applied and the intervals of input are appropriate. However, parameters should be prepared prior to the numerical calculation procedure.

In order to make the analytical model be consistent with the pavement in the unbonded overlay project, some of the parameters can be found directly from the project reports. For parameters like Young's modulus, reaction modulus, etc, they should be backcalculated from



Heavy weight deflectometer (HWD) data from project testing. A project report by S. Stoffels [21], and previous work by L. Yeh [22] already provided extensive work on backcalculation using the project data. Based on Stoffels [21], two programs, BAKFAA and ILL-BACK, were used to perform backcalculation and cross-verify the results. The models used by these two programs are based on different theories, BAKFAA is based on elastic theory and ILL-BACK is based on plate theory. Also, BAKFAA could define interface bonding conditions with the same method as BISAR but following a different way, which will be further explained in chapter 4. ILL-BACK can only model two-plate pavement systems; however, the equivalent slab method mentioned in section 1.2.3 could be used if there are more than two layers in models, both for bonded conditions and unbonded conditions. Hakim [20] completed a doctoral dissertation to do backcalculations of Young's moduli and an interface parameter, which represented bonding conditions, using BISAR. As described by Hall et al. [23], there is an algorithm to backcalculate reaction modulus,  $k$ , which could also be calculated using sensor data. That algorithm was not all obtained by in-situ experiments recently, but by relationships with other parameters such as CBR, Young's modulus and so on. Setiadji [24] undertook an extensive effort to build a modified correlation between  $k$  and Young's modulus of subgrade, and checked the correlation with LTPP data.

### **1.2.5 NUMERICAL CALCULATION METHODS**

In rigid pavement analytical models, there were many approaches to reach the final numerical solutions. But all of them were done after performing integral transform to governing equations and solving the equations under integral transform. The difficulty is that inverse integral transforms are not always easy to handle directly by equation derivation, thus numerical

methods were then conducted to solve this problem. The numerical methods which were used could be classified into two categories: Green's function method and direct integration method.

Green's function method is a generally applied method which could solve many of the problems. For example, it was used by L. Sun [5] to solve a problem which simulated the pavement system as a beam on viscoelastic subgrade. To work out Green's function, several integration methods could be chosen such as Fourier Transform, Laplace transform and Hankel transform.

On the other hand, Kim published a series of papers [6], [7], which used FFT (Fast Fourier Transform) techniques to calculate 2-D and 3-D Fourier Transform problems. FFT is essentially an algorithm to run Discrete Fourier Transform more efficiently. According to Kim [6], if the system doesn't have damping or just has a little damping, an exponential window method derived by Kausel & Roësset [25] from a similar concept in signal processing in the electrical engineering field should be used in case of spectral leakage.

There are still two other direct integration approaches which could be used, considered from a purely mathematical aspect. The first approach is to turn double integral to single integral, then use contour integration of complex function to replace improper integration. The other approach is self-adaptive numerical integration algorithm, which could be conducted using MATLAB. Some details of these methods will be specified in the following paragraphs.

For the first method, an existing example, which was a moving load exerting on an Euler beam laid on a Kelvin foundation, was worked out by H. Zhou [26]; he also displayed diagrams of several dynamic responses. This is a 1-D problem considered in analytical modeling and numerical calculation. However, the fundamental methodology would be the same, and it may be used in 2-D integration problems.

According to Zhou's analytical modeling results [26], the beam deflection caused by a moving constant line load is:

$$w = \frac{P}{2\pi} \int_{-\infty}^{\infty} \frac{\sin(\xi l)}{\xi l} \frac{e^{i\xi x}}{EI\xi^4 - mV^2\xi^2 + k - icV\xi} d\xi \quad (1.12)$$

integral kernel is  $F(\xi) = \frac{P}{2\pi} \frac{\sin(\xi l)}{\xi l} \frac{e^{i\xi x}}{EI\xi^4 - mV^2\xi^2 + k - icV\xi}$ , where  $P$  is the load,  $l$  is load length,  $EI$  is bending stiffness,  $m$  is mass of beam,  $c$  is viscous damping of underlayers,  $V$  is velocity of moving load,  $k$  is modulus of underlayers' reaction (stiffness of foundation per unit area). Values of these parameter are provided in Table 1-1. If the pavement system except the beam section is assumed to be an elastic model,  $c$  equals zero, which means no damping or slight damping.

Table 1-1 Parameters of Example

Parameters					
P	L	EI	M	$k$	V
10500 N	0.1 m	2300 Nm <sup>2</sup>	48.2 kg	689000000N/m <sup>2</sup>	100.68m/s

It can be summarized that the 1-D improper integration could be worked out by contour integration and residue theorem if the singularity points are countable (details are ignored here). The question of how to expand it to multi-dimensional integration problem still needs to be explored.

Going back to the second method, the self-adaptive integration algorithm, which is usually run by an existing MATLAB program, could solve both the 1-D problem and the multi-dimensional problem. From MATLAB version 2009a, function **quadgk** could handle 1-D oscillatory function with singularities on domain boundaries. And functions **quad2d** and **integral2**, developed in a later version of MATLAB, can also deal with functions with limited number of singularities to solve 2-D problems. More details of this method will be provided in Chapter 4 with examples.

### 1.2.6 RESULT ANALYSIS

The main purpose of the analytical model is to get the solutions of deflection, stress and strain. The sets of results run by the verified model should be analyzed in a parallel way as for the corresponding instrumentation data analysis, so investigation of how to develop an analysis of the instrumentation data is necessary.

Dynamic strain gage data provides direct measurement of pavement response to moving vehicle loads. The theses of L. Yeh [22] and V. Singh [27] have already used some of the instrumentation data from the full-scale unbonded overlay project. Lin Yeh [22] noted that the dynamic responses from loading in track 0 were the maximum responses, by evaluating average strain values of every track of the baseline experiment, which is thought to be reasonable because the strain gages were embedded along the path of track 0. Vishal Singh [27] successfully extracted useful data and then considered other characteristics of the responses (more than peak strain only) which would lead to pavement distresses and affect pavement performance; these response characteristics included, for example, duration, degree of recovery between axle peaks, and cumulative area of strain with time.

There has been some other research about analyzing dynamic strain data, although their research objects may be either rigid pavement or flexible pavement, they still may provide some clues to analyze strain gage data of our particular project. Burnham [28] did a best-fit curve and equation to correlate dynamic strain data with tire load proximity, which was the offset from sensor location to tire position. The pavement type was concrete pavement and dynamic strain data was peak strain values (compression or tension). Traffic could be started anywhere away from the roadway centerline, which is indicated in Figure 1-4. According to Figure 1-5, Burnham [28] reached the conclusion that maximum dynamic strain response did not occur when the reference point (center of outside tire) was at the location of the sensor.

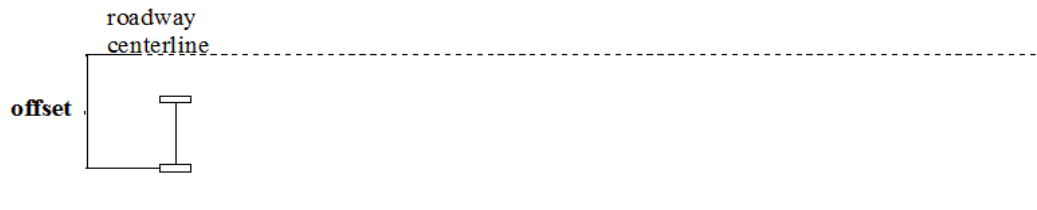


Figure 1-3 Tire Position Offset to Roadway Centerline

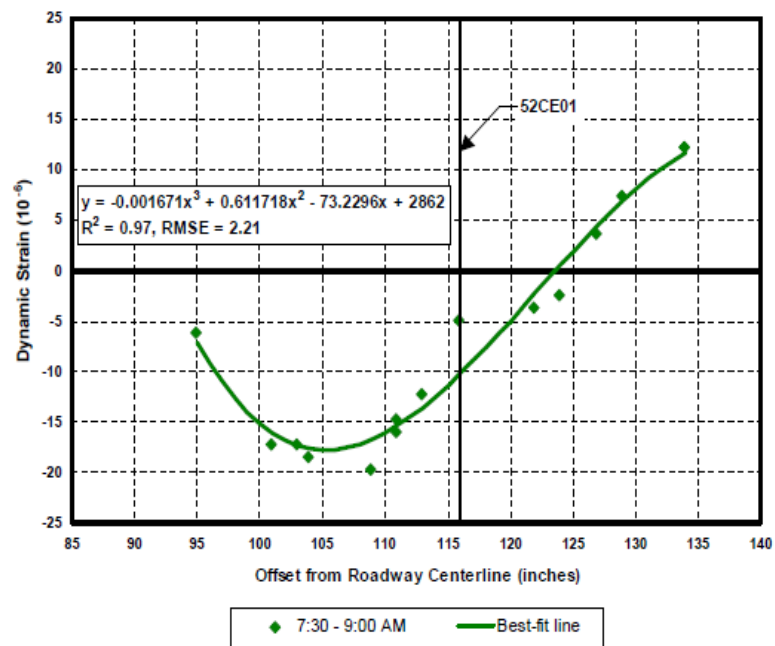


Figure 1-4 Dynamic Peak Strain versus Tire Offset for Axle 1, as Measured by Sensor 52CE01

by Burnham [28]

Darastani [2] demonstrated that vehicle speed would significantly affect the responses of an unbonded concrete pavement, as would traffic configuration, magnitude, frequency and

location of applied load, effect of subbase, reinforcement and shoulder. Tarr et al. [29] reached the conclusion through strain gage data analysis that structural responses of concrete pavement to vehicle load were highly affected by boundary conditions between concrete slab and subbase. Gokhale et al. [30] used 24 surface and embedded strain gauges to analyze the repeatability under different temperatures, tire pressures, applied load, and vehicle speeds. Embedded strain gauges and some surface strain gauges were installed right beneath the wheelpath; the other surface strain gauges were installed several inches off the wheelpath, longitudinally or transversely. But no further study about the effect induced by strain gauges of different positions was provided beyond repeatability verification. In research conducted by Gopalakrishnan et al. [31], horizontal strain gauge data was evaluated and dramatic peak strain responses of flexible pavement under aircraft loads were observed. The peak strain of each load pass was counted and the trend of peak strain change was studied; the number of load repetition could be used to evaluate fatigue of pavement.

### **1.3 CONCLUSION AND MODELING PLAN OVERVIEW**

Based on the literature review, there is no existing analytical model for concrete overlay pavement systems which considers all bonding conditions and viscoelastic material property. All bonding conditions refer to fully bonded, partially bonded and unbonding condition between overlay and underlay slabs, while the characterized viscoelastic body is assumed to simulate base layer and subgrade together.

The modeling work presented in this thesis was also conducted to be appropriate for Project FAA-01-G-002-04-2, the full-scale unbonded overlay experiment. Instrument data obtained by the project can be used for verification of the model. On the other hand, there may also be something this model could do for project result analysis. Previous works only considered strain gage data under track 0 (or track 0 together with track 1 and track -1), in which the

simulated traffic loads moved right above the embedded strain. Since the other tracks may also contribute to the damage of pavement, the contribution of other tracks may also be considered.

The flow chart for the development of this thesis model can be seen in Figure 1-6.

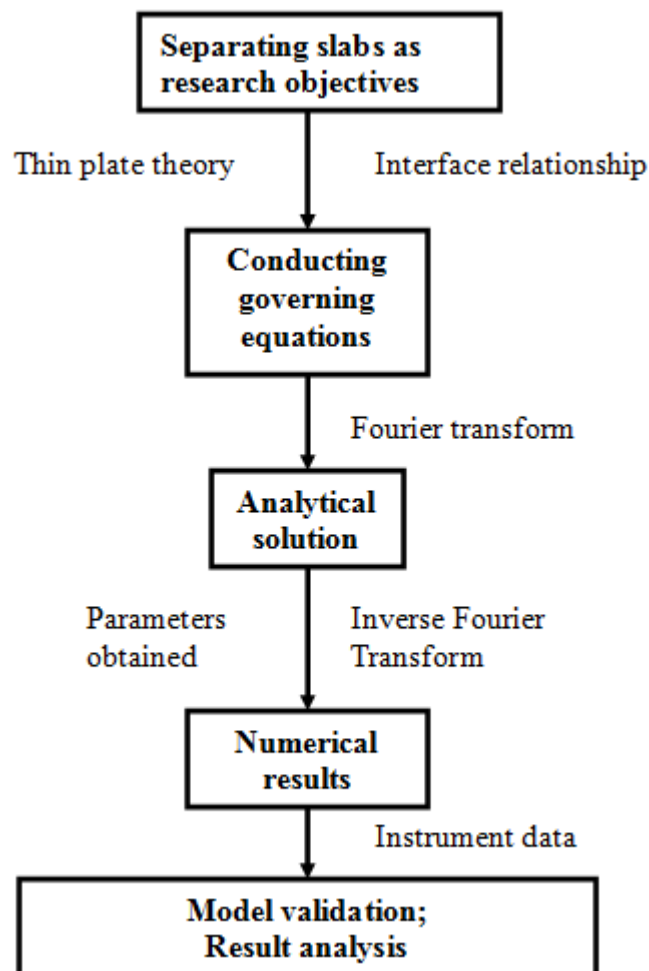


Figure 1-5 Flow Chart

The next chapter will provide the basic information about the full-scale unbonded overlay experiment, which will help provide the basis for the following chapters 3 and 4, analytical modeling and numerical modeling, respectively. The final chapter will be the summary and conclusions of the thesis, and possibilities for further research and model refinement.

## **Chapter 2 FULL SCALE TEST OF CC4**

### **2.1 BASIC INFORMATION**

IPRF (Innovative Pavement Research Foundation) Project FAA-01-G-002-04-2 was conducted at the Federal Aviation Administration (FAA) National Airfield Pavement Test Facility (NAPTF). The NAPTF databases are organized by Construction Cycles (CC); until now there is data from CC1 to CC6. The CC4 test item is Unbonded Rigid Overlay, and it was performed to improve the understanding of the influence of design parameters, thus enabling improvement of FAA design methods. The whole CC4 consisted of two separate phases, the Baseline Experiment and the SCI (Structural Condition Index) Validation Study. There were multiple objectives for both the Baseline Experiment and the SCI Validation Study; among all of them, the objectives to calibrate/validate structural responses and calibrate/validate gear effects were related to this thesis. Generally speaking, there were neither structure nor configuration changes between the Baseline Experiment and SCI Validation Study; therefore, the Baseline Experiment information is enough to achieve the goal of this thesis. Stoffels [21] and FAA [32] provided more explanation and information about the f-sAPT project. Only information related to the analytical modeling will be specified in following chapters, and those out of the topic area and situations which can't be considered in the ongoing analytical modeling, for example SCI investigation or temperature and moisture test and data, will not be illuminated.



Figure 2-1 End View and Side View of Baseline Experiment Design Configuration by Stoffels  
[21]

Table 2-1 Baseline Experiment Measured Thicknesses and Loading Configurations by Stoffels [21]

Test Item	Measured (and Design) Overlay Thickness, inches	Measured (and Design) Underlying Thickness, inches	Loading Configuration
North 1 (N1)	8.58 (9)	6.32 (6)	Triple Dual Tandem
North 2 (N2)	7.43 (7.5)	7.37 (7.5)	
North 3 (N3)	5.63 (6)	9.76 (10)	
South 1 (S1)	8.69 (9)	6.32 (6)	Dual Tandem
South 2 (S2)	7.34 (7.5)	7.65 (7.5)	
South 3 (S3)	5.71 (6)	9.8 (10)	

## 2.3 INSTRUMENT LOCATIONS

In this thesis, the only instrumentation result of interest is the embedded strain gage data. The strain gages in the longitudinal direction were located near the top and bottom of both overlay and underlay, where they could record almost the maximum compressive and tensile stress of each slab. Figure 2-2 depicts the situation of a vertical load exerted on an overlay pavement system. Horizontal positions of the strain gages are included in Appendix A.

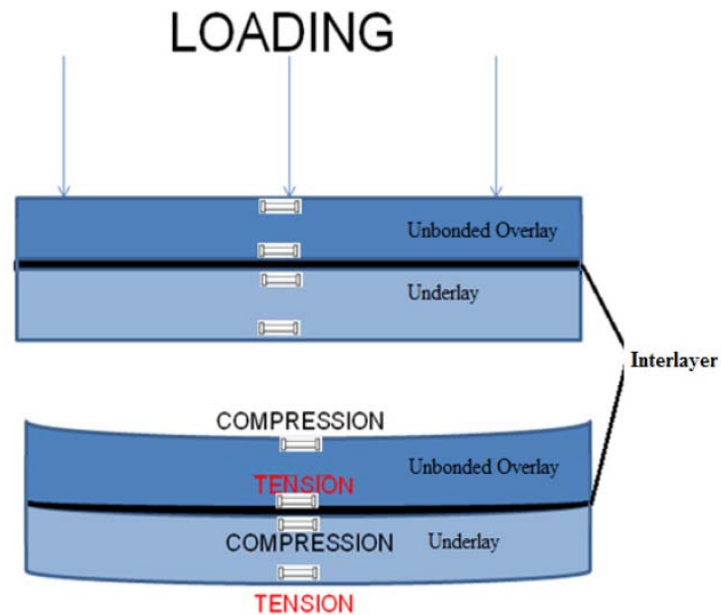


Figure 2-2 Overlay Deformation with Vertical Load by Singh [27]

## 2.4 PAVEMENT TESTS

### 2.4.1 HWD TEST

HWD (Heavy Weight Deflectometer) testing was repeated several times within one day and over several days over the course of the project. HWD testing was performed both right after underlay curing and overlay curing was finished. Deflection tests were conducted at center slab, slab corner and slab edge. Center slab testing was performed more in order to get the raw data to backcalculate moduli and monitor support conditions; the others were performed less frequently to test load transfer conditions between slabs. Locations of HWD testing are available in the project report appendix C [21].

### 2.4.2 MOVING LOAD TEST

Moving load testing was the central focus of this project; it simulated real traffic conditions but at an accelerated pace, and on pavement sections at the lower end of field thicknesses; therefore, there would be many passes until pavements fail. The loading carriage moved along the longitudinal direction with different wander paths (starting at different transverse positions). The gear configurations are shown in Figure 2-3, tridem dual axle gear and tandem dual gear loading was performed on test items in the North (N) and South (S), respectively.

The wander pattern had nine vehicle wander positions marked as tracks -4 to 4, which were shifted 10.25 inches from each other; the wanders were taken by each pass of different usage frequencies following a normal distribution. Wander usage frequencies were as Figure 2-4 shows, and the starting positions of each track are listed in Table 2-1.

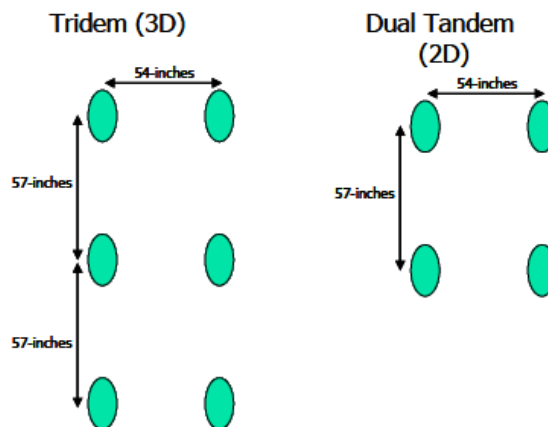


Figure 2-3 Gear Configurations by Stoffels [21]

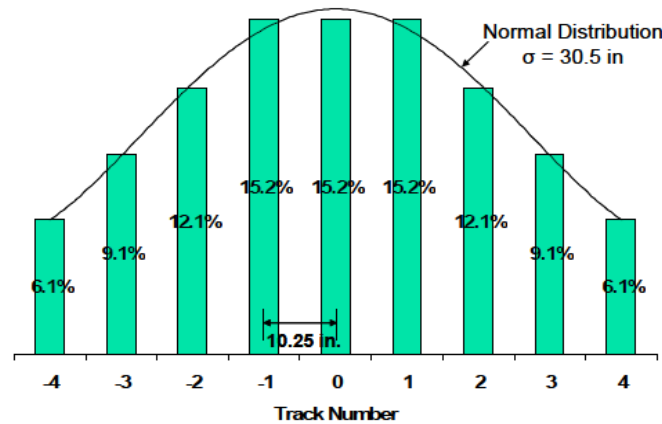


Figure 2-4 Wander Patterns by Stoffels [21]

Table 2-2 Starting Position of Each Track by Stoffels [21]

Track No.	Carriage Centerline Location (feet)	
	North	South
-4	-18.167	11.333
-3	-17.313	12.188
-2	-16.458	13.042
-1	-15.604	13.896
0	-14.750	14.750
1	-13.896	15.604
2	-13.042	16.458
3	-12.188	17.313
4	-11.333	18.167

Initially, a small number of tests with changing load level were conducted. The load sequence is in Table 2-2. According to Stoffels [21], seating load and gear response loading were applied to the overlay and underlay to test the linear position transducer (LPT) data. Interaction loading test was performed on the overlay to check if there were independent responses recorded in the adjacent test items. And the objective of ramp-up load test, also done on the overlay, was to examine the embedded strain gages and the stability of structure and gage response. Finally, the failure loading test was the target to get strain gage data; therefore, in subsequent sections about model verification, embedded strain data was selected for dates between 7/25/2006 to 10/31/2006. An example of embedded strain response history is shown in Figure 2-5.

Table 2-3 Loading Sequence by Stoffels [21]

Dates	Wanders	Wheel Loads (lbs)	Purpose
3/14/2006	44 passes	10000	Seating Load on Underlay
3/14/2006 to 3/15/2006	4	15000	Gear Response Loading on Underlay
3/15/2006	NA	10000	Static Loading on Underlay
5/22/2006 to 5/23/2006	88 passes	10000	Seating Load on Overlay
5/23/2006	NA	15000	Static Loading on Overlay
5/23/2006 to 5/24/2006	4	20000	Gear Response Loading on Overlay
7/6/2006	NA	20000	Interaction Loading
7/6/2006 to 7/12/2006	1	20000	Ramp-up Loading
	2	30000	
	3	40000	
7/25/2006 to 10/31/2006	Varied	50000	Failure Loading

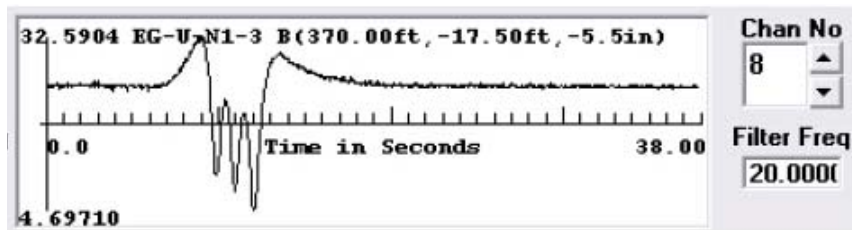


Figure 2-5 Embedded Strain Response History Example by Stoffels [21]

## Chapter 3 ANALYTICAL MODELING

### 3.1 INTRODUCTION

Since instruments can't measure and monitor pavement characteristics at all times and all places, analytical modeling helps with both verification and further understanding of the instrumentation data from the unbonded overlays. Therefore, the analytical model must be consistent with the pavement in the original project.

The analytical model could be separated into two parts, pavement system and load conditions. The pavement in the project is essentially a rigid pavement system, with concrete slabs modeled as thin plates, with the remaining layers modeled as viscoelastic or elastic foundation. According to the project report [21], the interaction between overlay and underlay was provided by a thin asphalt interlayer, such that the overlay and underlay slabs cannot be considered as a whole body, and the deformations of overlay over underlay were not the same as that of a whole body when subjected to load. As for adhesion, bonding conditions can be set as different constraint conditions in FEM software, or denoted by some coefficients such as Horizontal Shear Reaction Modulus  $K_s$  [19] and Interface Parameter  $I$  [33] and so on; more importantly, these two coefficients are dependent. The coefficient method was chosen in this paper because it is more productive to use and verify conditions from fully bonded, partially bonded, to nonbonded conditions by changing an input only. Moving loads are seen as constant or harmonic amplitude pressures within the contact area, with consideration of the effect of multi-axle loads.

The governing equations are high-order partial differential equations in this model; performing Fourier transforms reduces the order and turns differential equations to normal equations. The closed-form of Inverse Fourier transforms is not easy to work out, so numerical integration was used instead to get dynamic responses of pavement.

### 3.2 GOVERNING EQUATION

Elastic thin plate with small deformation theory is used in this mechanical model to simulate pavement slabs, both overlay and underlay. By making improvements to the traditional thin plate problem such as adding inertial term, reaction force from the layers underneath, and damping effect term, static equilibrium equations were turned into dynamic equilibrium equations [7]. Additionally, an adhesive effect is considered on the bottom surface of overlay and top surface of underlay, which makes the stress states different from that in Kim [7], which did not consider overlay, or thus the bonding condition. Therefore, it is necessary to derive governing equations from basic plate theory.

#### 3.2.1 KIRCHHOFF-LOVE ASSUMPTIONS

Before Kirchhoff-Love thin plate theory is used, some assumptions need to be clarified:

- 1) Deflection change along thickness could be ignored

$$w(x, y, z) = w(x, y) \quad (3.1)$$

- 2) Straight lines normal to the mid-surface remain straight and normal after deformation

$$\gamma_{xz} = \gamma_{yz} = 0 \quad (3.2)$$

where  $z$  is the axle along thickness, and original point is at the middle of plate thickness.

- 3) The thickness of the plate does not change during a deformation



$$\sigma_z = 0 \quad (3.3)$$

4) No deformation on central plane of plate

$$u(x, y, 0) = v(x, y, 0) = 0 \quad (3.4)$$

$u$  and  $v$  are displacement along  $x$  and  $y$  direction, respectively.

### 3.2.2 GEOMETRIC DEFORMATION RELATIONSHIP

According to elasticity mechanics, the geometric-deformation relationships are as from equation (3.5) to (3.9) show:

$$\varepsilon_x = \frac{\partial u}{\partial x} \text{ (3.5)}, \quad \varepsilon_y = \frac{\partial v}{\partial y} \text{ (3.6)}, \quad \gamma_{xz} = \frac{\partial u}{\partial z} + \frac{\partial w}{\partial x} \text{ (3.7)}, \quad \gamma_{yz} = \frac{\partial v}{\partial z} + \frac{\partial w}{\partial y} \text{ (3.8)}, \quad \gamma_{xy} = \frac{\partial v}{\partial x} + \frac{\partial u}{\partial y} \text{ (3.9)}$$

If equations (3.7) and (3.8) are substituted into equation (3.2)

$$\frac{\partial u}{\partial z} = -\frac{\partial w}{\partial x}, \quad \frac{\partial v}{\partial z} = -\frac{\partial w}{\partial y} \quad (3.10)$$

Integrating both sides, equation (3.10) turns into

$$u = -z \frac{\partial w}{\partial x}, \quad v = -z \frac{\partial w}{\partial y} \quad (3.11)$$

Then substituting equation (3.11) into equations (3.5), (3.6) and (3.9)

$$\varepsilon_x = -z \frac{\partial^2 w}{\partial x^2} \quad (3.12)$$

$$\varepsilon_y = -z \frac{\partial^2 w}{\partial y^2} \quad (3.13)$$

$$\gamma_{xy} = -2z \frac{\partial^2 w}{\partial x \partial y} \quad (3.14)$$

Based on equations (3.12), (3.13) and (3.14), it can be understood that  $w$  will be the only unknown variable in equilibrium equations.

### 3.2.3 CONSTITUTIVE RELATIONSHIP

Similarly, taking elasticity mechanics together with Kirchhoff-Love assumption (3.3), the stress-strain relationships are:

$$\varepsilon_x = \frac{1}{E}(\sigma_x - \nu\sigma_y) \quad (3.15)$$

$$\varepsilon_y = \frac{1}{E}(\sigma_y - \nu\sigma_x) \quad (3.16)$$

$$\gamma_{xy} = \frac{2(1+\nu)}{E}\tau_{xy} \quad (3.17)$$

Expressed as stresses, these relationships become

$$\sigma_x = -\frac{Ez}{1-\nu^2} \left( \frac{\partial^2 w}{\partial x^2} + \nu \frac{\partial^2 w}{\partial y^2} \right) \quad (3.18)$$

$$\sigma_y = -\frac{Ez}{1-\nu^2} \left( \frac{\partial^2 w}{\partial y^2} + \nu \frac{\partial^2 w}{\partial x^2} \right) \quad (3.19)$$

$$\tau_{xy} = -\frac{Ez}{1+\nu} \frac{\partial^2 w}{\partial x \partial y} \quad (3.20)$$

From equations (3.18), (3.19) and (3.20),  $\sigma_x$ ,  $\sigma_y$ ,  $\tau_{xy}$  are all linearly related to  $z$ , which will also lead into moment and torsion.

For pavement overlay, one can select a free body from the whole plate, as can be seen in Figure 3-1. The resulting moment equations are as follow in equations (3.21), (3.22) and (3.23).

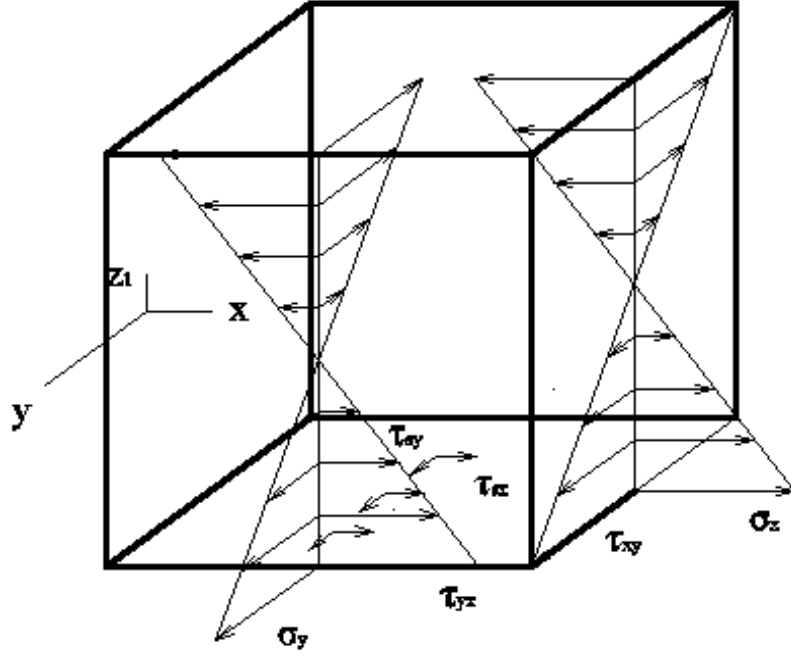


Figure 3-1 Stress States Within Free Body Of Overlay

$$M_{x1} = \int_{-h_1/2}^{h_1/2} \sigma_{x1} z_1 dz_1 + \tau_{sx1} \cdot \frac{h_1}{2} = -D_1 \left( \frac{\partial^2 w_1}{\partial x^2} + \nu_1 \frac{\partial^2 w_1}{\partial y^2} \right) - \frac{h_1}{2} K_s \left( \frac{h_1}{2} \frac{\partial w_1}{\partial x} + \frac{h_2}{2} \frac{\partial w_2}{\partial x} \right) \quad (3.21)$$

$$M_{y1} = \int_{-h_1/2}^{h_1/2} \sigma_{y1} z_1 dz_1 + \tau_{sy1} \cdot \frac{h_1}{2} = -D_1 \left( \frac{\partial^2 w_1}{\partial y^2} + \nu_1 \frac{\partial^2 w_1}{\partial x^2} \right) - \frac{h_1}{2} K_s \left( \frac{h_1}{2} \frac{\partial w_1}{\partial y} + \frac{h_2}{2} \frac{\partial w_2}{\partial y} \right) \quad (3.22)$$

$$M_{xy} = \int_{-h_1/2}^{h_1/2} \tau_{xy} z_1 dz_1 = -D_1 (1 - \nu_1) \frac{\partial^2 w_1}{\partial x \partial y} \quad (3.23)$$

where

$$D_1 = \frac{E_1 h_1^3}{12(1 - \nu_1^2)}$$

Then the resulting shear stresses and shear force between underlay and overlay are:

$$\tau_{sx1} = K_s (u_1 - u_2) = K_s \left( z_1 \frac{\partial w_1}{\partial x} - z_2 \frac{\partial w_2}{\partial x} \right) = K_s \left( -\frac{h_1}{2} \frac{\partial w_1}{\partial x} - \frac{h_2}{2} \frac{\partial w_2}{\partial x} \right) \quad (3.24)$$

$$\tau_{sy1} = K_s (u_1 - u_2) = K_s \left( z_1 \frac{\partial w_1}{\partial y} - z_2 \frac{\partial w_2}{\partial y} \right) = K_s \left( -\frac{h_1}{2} \frac{\partial w_1}{\partial y} - \frac{h_2}{2} \frac{\partial w_2}{\partial y} \right) \quad (3.25)$$

$$\tau_{sy1} = K_s (v_1 - v_2) = K_s \left( -\frac{h_1}{2} \frac{\partial w_1}{\partial y} - \frac{h_2}{2} \frac{\partial w_2}{\partial y} \right) \quad (3.26)$$

$$Q_{x1} = \int_{-h_1/2}^{h_1/2} \tau_{xz1} dz_1 \quad (3.27)$$

$$Q_{y1} = \int_{-h_1/2}^{h_1/2} \tau_{yz1} dz_1 \quad (3.28)$$

While for pavement underlay, the adhesive stress is on top surface, resulting in equations (3.29) through (3.33).

$$\tau_{sx2} = K_s (u_2 - u_1) = K_s \left( \frac{h_2}{2} \frac{\partial w_2}{\partial x} + \frac{h_1}{2} \frac{\partial w_1}{\partial x} \right) \quad (3.29)$$

$$\tau_{sy2} = K_s (v_2 - v_1) = K_s \left( \frac{h_2}{2} \frac{\partial w_2}{\partial y} + \frac{h_1}{2} \frac{\partial w_1}{\partial y} \right) \quad (3.30)$$

$$M_{x2} = \int_{-h_2/2}^{h_2/2} \sigma_{x2} z_2 dz_2 + \tau_{sx2} \cdot \frac{h_2}{2} = -D_2 \left( \frac{\partial^2 w_2}{\partial x^2} + \nu_2 \frac{\partial^2 w_2}{\partial y^2} \right) + \frac{h_2}{2} K_s \left( \frac{h_2}{2} \frac{\partial w_2}{\partial x} + \frac{h_1}{2} \frac{\partial w_1}{\partial x} \right) \quad (3.31)$$

$$M_{y2} = \int_{-h_2/2}^{h_2/2} \sigma_{y2} z_2 dz_2 + \tau_{sy2} \cdot \frac{h_2}{2} = -D_2 \left( \frac{\partial^2 w_2}{\partial y^2} + \nu_2 \frac{\partial^2 w_2}{\partial x^2} \right) + \frac{h_2}{2} K_s \left( \frac{h_2}{2} \frac{\partial w_2}{\partial y} + \frac{h_1}{2} \frac{\partial w_1}{\partial y} \right) \quad (3.32)$$

$$M_{xy2} = \int_{-h_2/2}^{h_2/2} \tau_{xy2} z_2 dz_2 = -D_2 (1 - \nu_2) \frac{\partial^2 w_2}{\partial x \partial y} \quad (3.33)$$

where

$$D_2 = \frac{E_2 h_2^3}{12(1 - \nu_2^2)}$$

$$Q_{x2} = \int_{-h_2/2}^{h_2/2} \tau_{xz2} dz_2 \quad (3.34)$$

$$Q_{y2} = -\int_{-h_2/2}^{h_2/2} \tau_{yz2} dz_2 \quad (3.35)$$

### 3.2.4 GOVERNING EQUATION

Dynamic force and reaction force are considered together with static forces in an element cut from a plate, the situation of overlay as is shown in Figure 3-2. Equilibriums are only selected in forces along the  $z$  direction, and moment about the  $x$  and  $y$  axes, so only forces and moments of these directions are drawn here and indicated in equations (3.36), while neglecting the others.

Assuming  $dx=dy$  in the free body of interest,  $x$  and  $y$  coordinates are consistent in both underlay and overlay, but the origin points of  $z$  axle are the middle points of them, respectively.

When equilibrium relationship is considered in overlay, the rest of the pavement including underlay is considered as a spring system with damping, while equilibrium in underlay, only base and subgrade is taken into consideration to give reaction force.

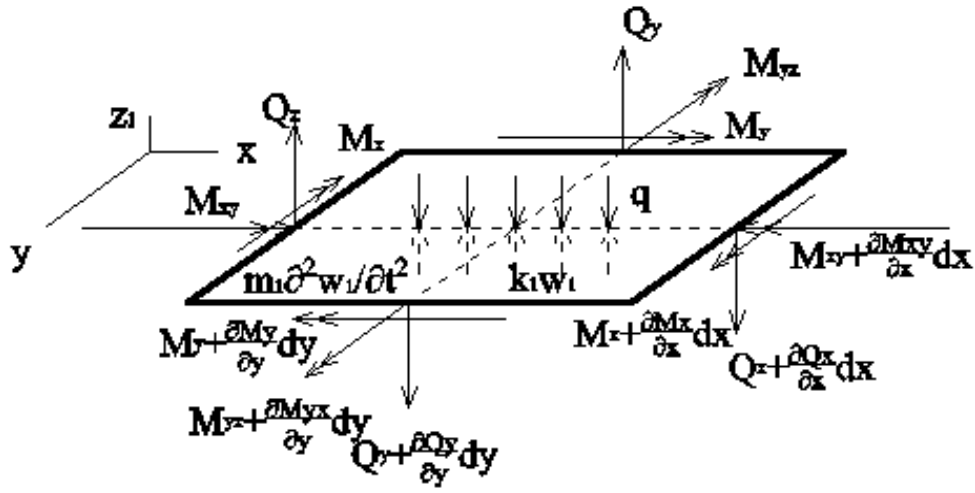


Figure 3-2 Equilibrium of Plate (Overlay) Element

$$\begin{aligned}\sum F_z &= 0 \\ \sum (M)_x &= 0 \\ \sum (M)_y &= 0\end{aligned}\quad (3.36)$$

For overlay, these equations turn into:

$$-\frac{\partial Q_{x1}}{\partial x} - \frac{\partial Q_{y1}}{\partial y} + m_1 \ddot{w}_1 + k_1 w_1 - q = 0 \quad (3.37)$$

$$Q_{y1} - \frac{\partial M_{y1}}{\partial y} - \frac{\partial M_{xy1}}{\partial x} = 0 \quad (3.38)$$

$$Q_{x1} - \frac{\partial M_{x1}}{\partial x} - \frac{\partial M_{yx1}}{\partial y} = 0 \quad (3.39)$$

where  $k_I$  is reaction modulus of underlay,  $m_I$  is mass per unit area of overlay.

Substituting equations (3.38) and (3.39) into equation(3.37), the governing equation for the overlay is:

$$D_1 \nabla^4 w_1 + \frac{h_1}{2} K_s \left( \frac{h_1}{2} \frac{\partial^3 w_1}{\partial x^3} + \frac{h_2}{2} \frac{\partial^3 w_2}{\partial x^3} \right) + \frac{h_1}{2} K_s \left( \frac{h_1}{2} \frac{\partial^3 w_1}{\partial y^3} + \frac{h_2}{2} \frac{\partial^3 w_2}{\partial y^3} \right) + m_1 \ddot{w}_1 + k_1 w_1 - q = 0 \quad (3.40)$$

where

$$\nabla^4 w_i = \frac{\partial^4 w_i}{\partial x^4} + 2\nu_i \frac{\partial^4 w_i}{\partial x^2 \partial y^2} + \frac{\partial^4 w_i}{\partial y^4}, i = 1, 2$$

Similarly, for the underlay, if the rest of the layers of the pavement (base, subbase, subgrade) can be seen as an entire body, and is simulated with a viscoelastic model, the equilibrium equations are:

$$-\frac{\partial Q_{x2}}{\partial x} - \frac{\partial Q_{y2}}{\partial y} + m_2 \ddot{w}_2 + k_2 w_2 + c \dot{w}_2 = 0 \quad (3.41)$$

$$Q_{y2} - \frac{\partial M_{y2}}{\partial y} - \frac{\partial M_{xy2}}{\partial x} = 0 \quad (3.42)$$

$$Q_{x2} - \frac{\partial M_{x2}}{\partial x} - \frac{\partial M_{yx2}}{\partial y} = 0 \quad (3.43)$$

where  $m_2$  is mass per unit area of underlay,  $k_2$  is reaction modulus of viscoelastic model,  $c$  is the viscous coefficient of viscoelastic model. The governing equation of the overlay is:

$$D_2 \nabla^4 w_2 - \frac{h_2}{2} K_s \left( \frac{h_2}{2} \frac{\partial^3 w_2}{\partial x^3} + \frac{h_1}{2} \frac{\partial^3 w_1}{\partial x^3} \right) - \frac{h_2}{2} K_s \left( \frac{h_2}{2} \frac{\partial^3 w_2}{\partial y^3} + \frac{h_1}{2} \frac{\partial^3 w_1}{\partial y^3} \right) + m_2 \ddot{w}_2 + k_2 w_2 + c \dot{w}_2 = 0 \quad (3.44)$$

A moving coordinate  $x' = x - Vt$  instead of fixed coordinate  $x$  is used here to turn a moving load problem to static load problem in calculation. Assuming vehicle loads move with a constant velocity  $V$ , then changing  $w_1(x, y, t)$ ,  $w_2(x, y, t)$  to  $w_1(x', y, t)$ ,  $w_2(x', y, t)$  with relation:

$$\frac{\partial w_i}{\partial x} = \frac{\partial w_i}{\partial x'} \frac{\partial x'}{\partial x} = \frac{\partial w_i}{\partial x'}, i = 1, 2 \quad (3.45)$$

giving,

$$\frac{\partial^{(n)} w_i}{\partial x^{(n)}} = \frac{\partial^{(n)} w_i}{\partial x'^{(n)}}, i = 1, 2 \quad (3.46)$$

and,

$$\frac{\partial w_i(x, y, t)}{\partial t} = \frac{\partial w_i(x', y, t)}{\partial t} + \frac{\partial w_i(x', y, t)}{\partial x'} \frac{\partial x'}{\partial t} = \frac{\partial w_i(x', y, t)}{\partial t} - V \frac{\partial w_i(x', y, t)}{\partial x'}, i = 1, 2 \quad (3.47)$$

$$\frac{\partial w_i^2(x, y, t)}{\partial t^2} = \frac{\partial w_i^2(x', y, t)}{\partial t^2} - 2V \frac{\partial w_i^2(x', y, t)}{\partial t \partial x'} + V^2 \frac{\partial w_i^2(x', y, t)}{\partial x'^2}, i = 1, 2 \quad (3.48)$$

By substituting equations (3.46), (3.47) and (3.48) into equations (3.40) and (3.44), the equation group could be rewritten as

$$\begin{aligned} D_1 \nabla^4 w_1 + \frac{h_1}{2} K_s \left( \frac{h_1}{2} \frac{\partial^3 w_1}{\partial x'^3} + \frac{h_2}{2} \frac{\partial^3 w_2}{\partial x'^3} \right) + \frac{h_1}{2} K_s \left( \frac{h_1}{2} \frac{\partial^3 w_1}{\partial y'^3} + \frac{h_2}{2} \frac{\partial^3 w_2}{\partial y'^3} \right) \\ + m_1 \left( \frac{\partial w_1^2}{\partial t^2} - 2V \frac{\partial w_1^2}{\partial t \partial x'} + V^2 \frac{\partial w_1^2}{\partial x'^2} \right) + k_1 w_1 - q = 0 \end{aligned} \quad (3.49)$$

$$\begin{aligned} D_2 \nabla^4 w_2 - \frac{h_2}{2} K_s \left( \frac{h_2}{2} \frac{\partial^3 w_2}{\partial x'^3} + \frac{h_1}{2} \frac{\partial^3 w_1}{\partial x'^3} \right) - \frac{h_2}{2} K_s \left( \frac{h_2}{2} \frac{\partial^3 w_2}{\partial y'^3} + \frac{h_1}{2} \frac{\partial^3 w_1}{\partial y'^3} \right) \\ + m_2 \left( \frac{\partial w_2^2}{\partial t^2} - 2V \frac{\partial w_2^2}{\partial t \partial x'} + V^2 \frac{\partial w_2^2}{\partial x'^2} \right) + k_2 w_2 + c \left( \frac{\partial w_2}{\partial t} - V \frac{\partial w_2}{\partial x'} \right) = 0 \end{aligned} \quad (3.50)$$

### 3.3 ANALYTICAL SOLUTION

In order to solve the governing equations, double and triple dimensional Fourier Transform Integration should be performed to decrease the order of partial differential equations, according to Kim [7] and Cai [10]. The Fourier transform pair is defined as:

$$\tilde{f}(\xi) = \int_{-\infty}^{\infty} f(x) e^{-i\xi x} dx$$

$$f(x) = \frac{1}{2\pi} \int_{-\infty}^{\infty} \tilde{f}(\xi) e^{i\xi x} d\xi$$

Applying Fourier Transform to both sides of equations (3.49) and (3.50), both of the equations were solved following a sequence of time domain transformed to frequency domain, moving coordinate  $x'$  to  $\xi$ , and fixed coordinate  $y$  to  $\zeta$ .

During the procedure, derivatives of Fourier Transform are the critical step:

$$f^{(n)}(x) = (i\xi)^n \tilde{f}(x), \text{ when } f(-\infty) \rightarrow 0$$

which can be proved by changing the complex term of the kernel function from exponential form to trigonometric form,

$$e^{i\xi x} = \cos(\xi x) + i \sin(\xi x)$$

After transform, governing equations change to a normal two-variable equation group:

$$D_1 W_1 (\xi^2 + \zeta^2)^2 - \frac{h_1 K_s}{4} i (h_1 W_1 + h_2 W_2) (\xi^3 + \zeta^3) - m_1 (\Omega - V \xi)^2 W_1 + k_1 W_1 - Q = 0$$

$$D_2 W_2 (\xi^2 + \zeta^2)^2 + \frac{h_2 K_s}{4} i (h_1 W_1 + h_2 W_2) (\xi^3 + \zeta^3) - m_2 (\Omega - V \xi)^2 W_2 + k_2 W_2$$

$$+ i (\Omega - V \xi) c W_2 = 0$$

where

$$W_i(\xi, \zeta, \Omega) = \int_{-\infty}^{\infty} \int_{-\infty}^{\infty} \int_{-\infty}^{\infty} w_i(x', y, t) e^{-ix'\xi} e^{-iy\zeta} e^{-it\Omega} dx' dy dt, i = 1, 2,$$

$$\tilde{F}(\xi, \zeta, \Omega) = \int_{-\infty}^{\infty} \int_{-\infty}^{\infty} \int_{-\infty}^{\infty} q e^{-ix'\xi} e^{-iy\zeta} e^{-it\Omega} dx' dy dt$$

By solving the equation group, one obtains

$$W_1 = \frac{\tilde{F} b}{ab - \frac{h_1^2 h_2^2 K_s^2}{16} (\xi^3 + \zeta^3)^2} \quad (3.51)$$

$$W_2 = \frac{-\frac{h_1 h_2 K_s i}{4} (\xi^3 + \zeta^3) \tilde{F}}{ab - \frac{h_1^2 h_2^2 K_s^2}{16} (\xi^3 + \zeta^3)^2} \quad (3.52)$$



in which,  $a = D_1 (\xi^2 + \zeta^2)^2 - \frac{h_1^2 K_s}{4} i (\xi^3 + \zeta^3) - m_1 (\Omega - V\xi)^2 + k_1$ ,

$$b = D_2 (\xi^2 + \zeta^2)^2 + \frac{h_2^2 K_s}{4} i (\xi^3 + \zeta^3) - m_2 (\Omega - V\xi)^2 + k_2 + ic(\Omega - V\xi)$$

If parameter  $K_s$  is yielded to 0, which means unbonded condition,  $b$  is the same as the denominator of deflection in Kim [7], which somewhat verifies equations (3.51) and (3.52).

### 3.4 LOAD EXPRESSION

Gear configurations in the unbonded overlay f-sAPT Baseline Experiment were dual tandem and dual tridem gears, as briefly summarized in chapter 2. Although they didn't exactly match the precise dimensions of specific commercial airplanes, they approximated gears of commonly used heavy passenger aircraft. The geometry of the gear configurations is from the project report [21], as was illustrated in Figure 2-3.

The other important thing is the transverse coordinate of the initial position, as the multiple-axle load moved following a straight line path which was parallel to the edge of the pavement slab. The transverse positions varied with passes, and these passes consisted of a wander pattern varying with subsequent passes to simulate real traffic conditions, as shown in Figure 3-3. Therefore, initial coordinates of load should be taken into consideration in the load expression. Tire load is assumed as a constant or harmonic square (rectangular) pressure, and the geometry of gear configuration is as Figure 3-4 shows.

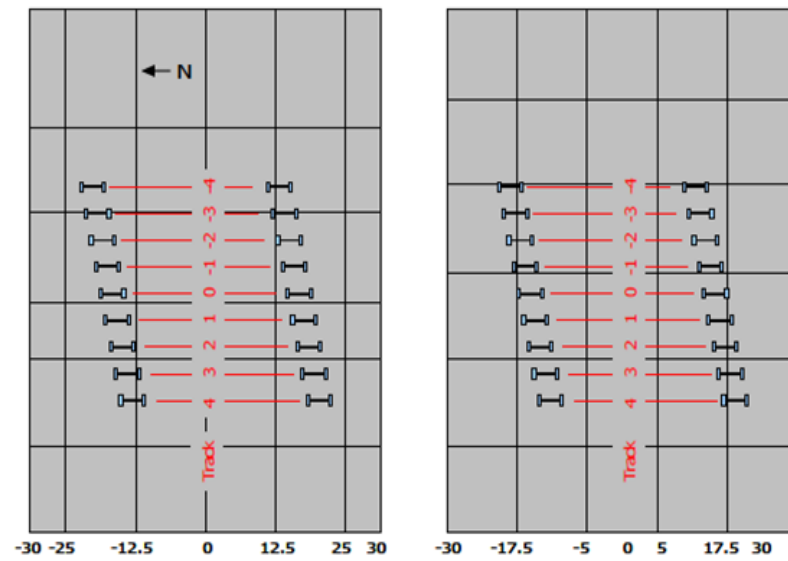


Figure 3-3 Loading Positions of Wanders by Stoffels [21]

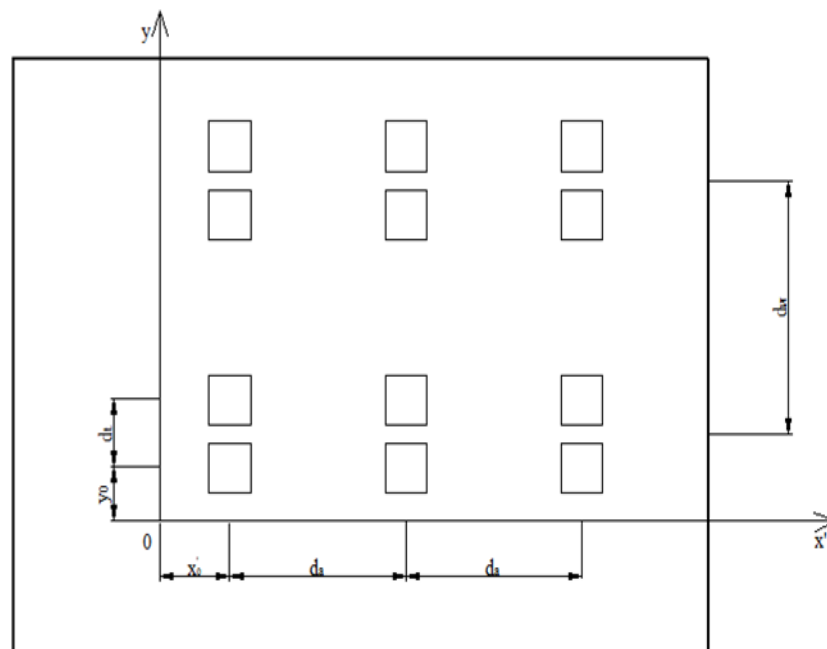


Figure 3-4 Geometry of Gear Configuration

Heaviside Step Function could describe the load condition appropriately, with the form,

$$H(f(x)) = \begin{cases} 1, & f(x) > 0 \\ 0, & f(x) < 0 \end{cases}$$

Each gear pressure is written all in the form of:

$$F = \frac{P}{4l_1l_2} H\left(l_1^2 - (x' - x'_c)^2\right) H\left(l_2^2 - (y - y_c)^2\right) f(t) \quad (3.53)$$

where  $(x'_c, y_c)$  is the coordinates of gear pressure center and  $(x'_0, y_0)$  represents the coordinates of one of the tire centers (for this purpose, the right outer tire of the last axle is chosen), which could describe different wander positions of the vehicle by taking different values.  $l_1, l_2$  are edges along the x and y axes of assumed rectangular contact area.

For the first axle, load center coordinates are:

$$\begin{aligned} x'_c &= x'_0, y_c = y_0 \\ x'_c &= x'_0, y_c = y_0 + d_t \\ x'_c &= x'_0, y_c = y_0 + d_w \\ x'_c &= x'_0, y_c = y_0 + d_w + d_t \end{aligned}$$

The gear pressures could be obtained separately. Since the whole system is linear, a superposition of gear pressures to get the whole load exerted by one axle of vehicle results in:

$$\begin{aligned} F_1 &= \sum_i^4 F_{1i} \\ &= \frac{P}{4l_1l_2} f(t) \left( H\left(l_1^2 - (x' - x'_0)^2\right) H\left(l_2^2 - (y - y_0)^2\right) \right. \\ &\quad + H\left(l_1^2 - (x' - x'_0)^2\right) H\left(l_2^2 - (y - (y_0 + d_t))^2\right) \\ &\quad + H\left(l_1^2 - (x' - x'_0)^2\right) H\left(l_2^2 - (y - (y_0 + d_w))^2\right) \\ &\quad \left. + H\left(l_1^2 - (x' - x'_0)^2\right) H\left(l_2^2 - (y - (y_0 + d_w + d_t))^2\right) \right) \end{aligned} \quad (3.54)$$

The second and third axle loads have the same form as that of first axle, by substituting the center coordinates,

$$\begin{aligned} x'_{c2} &= x'_0 + d_a \\ x'_{c3} &= x'_0 + 2d_a \end{aligned}$$

Then, total load of dual tandem gears is:

$$F_{\text{tandem}} = \sum_{i=1}^2 F_i \quad (3.55)$$

whereas for tridem gears:

$$F_{\text{tridem}} = \sum_{i=1}^3 F_i \quad (3.56)$$

Since pavement deflection is now under Fourier Transform, the same procedure is also needed for load,

$$\tilde{F} = \frac{P}{4l_1 l_2} \int_{-\infty}^{\infty} \int_{-\infty}^{\infty} \int_{-\infty}^{\infty} H\left(l_1^2 - (x' - x_c')^2\right) H\left(l_2^2 - (y - y_c)^2\right) f(t) e^{-ix'\xi} e^{-iy\zeta} e^{-i\Omega t} d\xi d\zeta dt \quad (3.57)$$

where

$$\begin{aligned} \int_{-\infty}^{\infty} H\left(l_1^2 - (x' - x_c')^2\right) e^{-ix'\xi} dx' &= \int_{x_c' - l_1}^{x_c' + l_1} e^{-ix'\xi} dx' = \frac{2e^{-ix_c'\xi} \sin \xi l_1}{\xi} \\ \tilde{F} &= P \frac{e^{-ix_c'\xi} \sin \xi l_1}{\xi l_1} \frac{e^{-iy\zeta} \sin \zeta l_2}{\zeta l_2} \int_{-\infty}^{\infty} f(t) e^{-i\Omega t} dt \end{aligned} \quad (3.58)$$

if  $f(t)$  is a constant, assuming  $f(t) = 1$ , Fourier Transform of a constant is,

$$\int_{-\infty}^{\infty} e^{-i\Omega t} dt = 2\pi\delta(\Omega)$$

then,

$$\tilde{F} = 2\pi P \frac{e^{-ix_c'\xi} \sin \xi l_1}{\xi l_1} \frac{e^{-iy\zeta} \sin \zeta l_2}{\zeta l_2} \delta(\Omega) \quad (3.59)$$

The Fourier Transform of dual tandem and tridem gear loads are as shown,

$$\begin{aligned} \tilde{F}_{\text{tandem}} &= P \frac{\sin \xi l_1}{\xi l_1} \frac{\sin \zeta l_2}{\zeta l_2} e^{-ix_0'\xi} e^{-iy_0\zeta} \left(1 + e^{-id_a\zeta}\right) \left(1 + e^{-id_l\zeta} + e^{-id_w\zeta} + e^{-i(d_l+d_w)\zeta}\right) \int_{-\infty}^{\infty} f(t) e^{-i\Omega t} dt \end{aligned} \quad (3.60)$$

which is consistent with the result of Kim [7], so the method is considered to be appropriate to use. Similarly,

$$\begin{aligned} & \tilde{F}_{\text{tridem}} \\ &= P \frac{\sin \xi l_1}{\xi l_1} \frac{\sin \zeta l_2}{\zeta l_2} e^{-ix_0 \xi} e^{-iy_0 \zeta} \left(1 + e^{-id_a \xi} + e^{-2id_a \xi}\right) \left(1 + e^{-id_t \zeta} + e^{-id_w \zeta} + e^{-i(d_t + d_w) \zeta}\right) \int_{-\infty}^{\infty} f(t) e^{-i\Omega t} dt \end{aligned} \quad (3.61)$$

When  $f(t) = 1$ , which means a constant moving load,

$$\begin{aligned} & \tilde{F}_{\text{tandem}} \\ &= 2\pi P \frac{\sin \xi l_1}{\xi l_1} \frac{\sin \zeta l_2}{\zeta l_2} e^{-ix_0 \xi} e^{-iy_0 \zeta} \left(1 + e^{-id_a \xi}\right) \left(1 + e^{-id_t \zeta} + e^{-id_w \zeta} + e^{-i(d_t + d_w) \zeta}\right) \delta(\Omega) \end{aligned} \quad (3.62)$$

$$\begin{aligned} & \tilde{F}_{\text{tridem}} \\ &= 2\pi P \frac{\sin \xi l_1}{\xi l_1} \frac{\sin \zeta l_2}{\zeta l_2} e^{-ix_0 \xi} e^{-iy_0 \zeta} \left(1 + e^{-id_a \xi} + e^{-2id_a \xi}\right) \left(1 + e^{-id_t \zeta} + e^{-id_w \zeta} + e^{-i(d_t + d_w) \zeta}\right) \delta(\Omega) \end{aligned} \quad (3.63)$$

When the gear pressure is harmonic load, assuming there is no phase lag among axles, which also means all the axles start to work together,  $f(t) = e^{i\Omega_0 t}$ ,  $\Omega_0$  is a certain value of frequency,

$$\begin{aligned} & \tilde{F}_{\text{tandem}} \\ &= 2\pi P \frac{\sin \xi l_1}{\xi l_1} \frac{\sin \zeta l_2}{\zeta l_2} e^{-ix_0 \xi} e^{-iy_0 \zeta} \left(1 + e^{-id_a \xi}\right) \left(1 + e^{-id_t \zeta} + e^{-id_w \zeta} + e^{-i(d_t + d_w) \zeta}\right) \delta(\Omega - \Omega_0) \end{aligned} \quad (3.64)$$

$$\begin{aligned} & \tilde{F}_{\text{tridem}} \\ &= 2\pi P \frac{\sin \xi l_1}{\xi l_1} \frac{\sin \zeta l_2}{\zeta l_2} e^{-ix_0 \xi} e^{-iy_0 \zeta} \left(1 + e^{-id_a \xi} + e^{-2id_a \xi}\right) \cdot \\ & \quad \left(1 + e^{-id_t \zeta} + e^{-id_w \zeta} + e^{-i(d_t + d_w) \zeta}\right) \delta(\Omega - \Omega_0) \end{aligned} \quad (3.65)$$

### 3.5 CONCLUSION

Dynamic responses of an unbonded overlay under Fourier Transform are obtained in this chapter. At first, a governing equation group, which is actually dynamic equilibrium equations of overlay and underlay, is worked out by using Kirchhoff plate theory, elasticity constitutive

relationships and a bonding constitutive relationship. Then, Fourier Transform is performed to solve the equation group to get deflections of the slabs directly; the load expression remains unknown by the end of this step.

Load expression under Fourier Transform is the key point to the next step. Dynamic responses under Inverse Fourier Transform are dependent on different kinds of load expressions. Dual tandem and dual tridem gear loads are considered, respectively, as they were the load configurations actually utilized in the f-sAPT project. The load is simulated as both constant pressure and harmonic pressure.

## **Chapter 4 COEFFICIENTS BACKCALCULATION AND NUMERICAL SOLUTION**

### **4.1 INTRODUCTION**

Chapter 3 reaches to the step of doing Inverse Fourier Transform to get the results for pavement dynamic responses including deflection, stress and strain. However, it is difficult to get a closed-form or full analytical solution because kernel functions can not always be integrated to a certain integrand. Therefore, approximate methods, such as numerical methods, are used instead, which is as accurate as analytical method and more efficient if intervals are defined appropriately. Therefore, numerical methods could also provide a good result without a certain expression of dynamic response function with changeable variables, but a set of function values will be obtained which is equivalent to that aforementioned function, with variable values substituted.

With respect to doing numerical analysis, a prerequisite is needed which requires all the pavement parameters to be determined through an inverse analysis, or backcalculation, procedure. For the parameters which were verified to be sensitive, Stoffels [21] and Yeh [22] used HWD test data and software BAKFAA and ILL-BACK to backcalculate elastic moduli of every layer. Additionally, by using BAKFAA, the interface parameter  $l$  could also to be backcalculated. The value of  $l$  varies from 0 to 1, representing from unbonded condition to fully bonded condition. More importantly, there is correlation between interface spring stiffness (also defined as Horizontal Shear Reaction Modulus)  $K_s$ , which was defined and utilized in the analytical model in last chapter, and  $l$  denoted by Hayhoe [33]. It can be concluded that BAKFAA could be used to work out the parameters needed in numerical calculation.

Numerical integration could start after exact values of parameters are determined. Kim [7],[12] and Cai [10] used FFT (Fast Fourier Transform) techniques, and provided diagrams which showed dynamic responses varying along both moving and fixed axles. Direct integration known as self-adaptive numerical integration algorithm was also used by Jiang [11]. Although any of the methods mentioned above could be used to calculate the final numerical results, since the program MATLAB is used to perform the integration for this thesis, self-adaptive numerical integration algorithm is considered the most convenient way and is selected. Certainly, an example worked out by self-adaptive numerical integration algorithm is needed to compare with the same problem worked out by other methods. To specify the situation in this thesis, the problem from a reference will be worked out by self-adaptive numerical integration algorithm and compared with that by FFT. Only if they are in highly substantial agreement, the self-adaptive numerical integration algorithm could be verified and used in further calculations and numerical analysis.

Finally, the dynamic response data obtained by the developed model and by the f-sAPT project instrumentation are compared to evaluate the consistency and accuracy of the thesis model. The strain gauge data history recorded is chosen as an example. During this data analysis procedure, peak values of strain, recovery and cumulative area are among the most interesting and relevant parameters.

In the following sections, section 4.2 provides all the parameters needed in numerical calculation, including those obtained directly from the project report, those rearranged from previous researches which were also about the same project, and the remaining ones calculated from HWD data. Section 4.3 mainly focuses on how to do numerical calculations to deal with this problem; the methodology is presented first, then the problem in a reference is tried to see if the results will also match. After a positive comparison is obtained, dynamic response history diagrams obtained by modeling and experiment are evaluated to see the consistency, in section



4.4, as a form of model verification. Then, numerical analysis and conclusions are provided in sections 4.5 and 4.6, respectively.

## 4.2 PARAMETERS OBTAINED AND BACKCALCULATION

### 4.2.1 GEOMETRIC PARAMETERS

There are two categories of parameters needed in numerical calculation, geometric parameters and mechanical parameters. For the geometric parameters, all could be found in project report [21], except the contact areas assumed in analytical model are squares but rather than circular or elliptical areas, so an approximation is made. Tire contact area mentioned in Stoffels [21] was 214.6 in<sup>2</sup>; two of the squares together were taken as having the same area as that in the f-sAPT testing, ignoring the distance between dual tires, so the resulting edge of square is 10.36 inches. While other geometrical parameters were assigned directly from the project report [21], values of these parameters, which could also be found in Figure 2-3, and are summarized in Table 4-1 in SI units.

Table 4-1 Geometric Parameters (mm)

$x_0$	$y_0$	$l_1$	$l_2$	$d_t$	$d_w$	$d_a$
0	0	263.144	263.144	263.144	1371.6	1447.8

#### 4.2.2 MECHANICAL PARAMETERS

On the other hand, mechanical parameters are calculated using the program BAKFAA and the HWD data. Key techniques in BAKFAA are layered elastic analysis program LEAF and an error minimization method [22].

HWD provided fundamentally response data; HWD testing was conducted many times during the CC4 unbonded overlay experiment, so there is a large amount of data sets and only part of them are useful here. Deflections of all 12 slabs of the six test items which are results of center slab testing, including data of six sensors in the deflection basin area which are at 0 inches, 11.81 inches, 23.62 inches and 35.43 inches (0mm, 300mm, 600mm and 900mm) away from the center of deflection plate, are shown in Appendix D of project report [21]. The HWD data extended from 6/22/2006 to 11/20/2006, which is almost the same time as failure load testing mentioned in chapter 2. All of these make data in Appendix D [21] appropriate for mechanical parameters backcalculation, at the same time monitoring how support conditions changed.

LEAF allows relative horizontal movement between two layers at an interface by assuming uniformly distributed shear springs to connect the two layers. To reduce the complexity of computation, LEAF and BAKFAA use variable  $l$ , but not  $K_s$ , to describe bonding condition with relationship between  $l$  and  $K_s$  [33]:

$$K_s = \frac{l}{1-l} \quad (4.1)$$

For fully bonded layers,  $K_s$  is close to infinity,  $l=1$ , which means no relative movement, while for fully unbonded layers,  $K_s=0$ ,  $l=0$ , which means no shear stress between layers. Except for these two extreme situations, for different partially bonded situations,  $K_s$  varies from 0 to infinity, and  $l$  varies from 0 to 1.

By inputting thickness of each layer and seed values of mechanical parameters, backcalculation can be done to match HWD data provided with criteria that RMS need to be smaller than 0.1. The root mean square (RMS) is the difference between measured and calculated sensor deflections, which is defined as:

$$RMS = \sqrt{\frac{1}{n} \sum_{i=1,n} (z_{mi} - z_{ci})^2}$$

$z_{mi}$  = deflection measured by sensor  $i$

$z_{ci}$  = deflection calculated at location of sensor  $i$

$n$  = number of sensors

The modulus backcalculation could be taken from previous work such as Stoffels [21]. As for  $k$  value, it can be estimated from other properties like CBR, resilient modulus and elastic modulus [24], and according to the requirements in the previous chapter, both values of the layers below the underlay and of the layers below the overlay are needed. According to Table 4-2, within the CC4 HWD raw data, there are results from 3/15/2006, which is the date that underlay slab testing was performed, so the deflections obtained could be used to backcalculate  $k$  of layers below underlay. Data after 7/24/2006 are used to backcalculate  $k$  of layers below the overlay.

Table 4-2 CC4 Construction Schedule by Stoffels [21]

<b>Activity</b>	<b>Date</b>
Subgrade preparation by FAA	Nov. 28, 2005 – Jan. 24, 2006
Subbase construction	Jan. 31 - Feb. 2, 2006
Underlying pavement instrumentation	Feb. 13 – 17
Underlying pavement construction set up (forms, paver, & other mob activities)	Feb. 20 – 23
Paving of underlying pavement	Feb. 27 – 28
Cut joints	Feb. 28 – Mar. 2
Curing of underlying pavement	Feb. 28 – Mar. 10
Underlying slab testing	Mar. 13 – 16
Overlay instrumentation	Mar. 20 – 24
AC interlayer paving	Mar. 22
Overlay pavement construction set-up	Mar. 27 – 28
Overlay concrete paving	Mar. 29
Cut joints	Mar. 29 – 30
Demobilization	Mar. 30 – 31
Curing of overlay pavement	Mar. 30 – May 8
Overlay surface instrumentation	May 8 – 12
Final construction activities (shoulder fill, insert backer rod, etc)	May 8 – 12

Table 4-3 BAKFAA Baseline Experiment Seed Moduli by Stoffels [21]

<b>LAYER</b>	<b>E (ksi)</b>	<b>v</b>	<b>INTERFACE PARAMETER</b>	<b>LAYER CHANGEABLE</b>
CONCRETE OVERLAY	4000	0.15	1	Yes
ASPHALT INTERLAYER	200	0.4	0	Yes
UNDERLYING SLAB	4000	0.15	0	Yes
SUBBASE	40	0.45	0	Yes
SUBGRADE	39.41	0.45	0	Yes

For backcalculation, thicknesses of layers were as-built, and thickness of subgrade in BAKFAA is assumed to be 0, which represents an infinite layer. Seed moduli are as shown in the last three rows of Table 4-3. Backcalculation results for the underlay are as Table 4-4 shows, noting that the interface parameters were all 0 when calculating the underlay modulus.

Table 4-4 Moduli from HWD Testing on Underlay

	N1	S1	N2	S2	N3	S3
$E_{UL}$ (psi)	1,039,813	707,071	720,579	442,294	313,400	266,986
$E_{BA}$ (psi)	9,392	43,020	5,033	24,318	19,667	17,024
$E_{Sub}$ (psi)	31,779	25,758	37,774	28,383	27,856	27,725
RMS (mils)	1.7096	1.4666	1.8291	1.2638	1.1349	1.0696
$k$ (pci)	276.9356	234.5334	317.509	253.2493	249.5219	248.5931
$k$ (N/m <sup>3</sup> )	75,173,376	63,663,420	86,186,909	68,743,798	67,732,006	67,479,886

The  $k$ -values in Table 4-4 are calculated by  $E_{sub} = 26k^{1.264}$ , which will be used as  $k_2$ .

For  $k_1$ , the values are as Table 4-5 to 4-10 show, where the data of date 8/1/2006 is directly from the project report [21].

Table 4-5 Moduli of Pavement System (Test Item N1)

N1				
Date	$E_{OL}$ (Pa)	$E_{UL}$ (Pa)	$E_{Sub}$ (Pa)	$k$ (N/m <sup>3</sup> )
7/25/2006	4.14E+10	4.77E+10	2.94E+08	9.48E+07
8/1/2006*	1.99E+10	1.81E+10	-	5.89E+07
8/9/2006	3.36E+10	3.04E+10	2.30E+08	7.81E+07
8/15/2006	3.18E+10	2.77E+10	2.20E+08	7.54E+07
10/10/2006	2.71E+10	2.04E+10	1.97E+08	6.92E+07
11/7/2006	2.62E+10	2.15E+10	1.88E+08	6.67E+07

Table 4-6 Moduli of Pavement System (Test Item S1)

S1				
Date	$E_{OL}$ (Pa)	$E_{UL}$ (Pa)	$E_{Sub}$ (Pa)	$k(N/m^3)$
7/25/2006	4.51E+10	5.47E+10	2.92E+08	9.44E+07
8/1/2006*	3.05E+10	2.73E+10	-	7.22E+07
8/9/2006	3.50E+10	3.11E+10	2.42E+08	8.12E+07
8/15/2006	3.46E+10	3.32E+10	2.41E+08	8.11E+07
10/10/2006	3.11E+10	2.80E+10	2.20E+08	7.55E+07
11/7/2006	4.14E+10	3.19E+10	2.26E+08	7.71E+07

Table 4-7 Moduli of Pavement System (Test Item N2)

N2				
Date	$E_{OL}$ (Pa)	$E_{UL}$ (Pa)	$E_{Sub}$ (Pa)	$k(N/m^3)$
7/25/2006	4.42E+10	6.51E+10	3.10E+08	9.89E+07
8/1/2006*	2.59E+10	2.37E+10	-	7.14E+07
8/9/2006	3.42E+10	3.15E+10	2.58E+08	8.55E+07
8/15/2006	2.86E+10	2.99E+10	2.36E+08	7.96E+07
10/10/2006	3.28E+10	2.60E+10	2.38E+08	8.03E+07
11/7/2006	3.02E+10	2.97E+10	2.10E+08	7.27E+07

Table 4-8 Moduli of Pavement System (Test Item S2)

S2				
Date	$E_{OL}$ (Pa)	$E_{UL}$ (Pa)	$E_{Sub}$ (Pa)	k(N/m <sup>3</sup> )
7/25/2006	4.62E+10	5.92E+10	3.24E+08	1.02E+08
8/1/2006*	3.12E+10	3.16E+10	-	7.79E+07
8/9/2006	4.07E+10	3.99E+09	2.69E+08	8.83E+07
8/15/2006	4.63E+10	3.71E+10	2.69E+08	8.83E+07
10/10/2006	3.87E+10	3.56E+10	2.56E+08	8.49E+07
11/7/2006	3.88E+10	3.48E+10	2.19E+08	7.53E+07

Table 4-9 Moduli of Pavement System (Test Item N3)

N3				
Date	$E_{OL}$ (Pa)	$E_{UL}$ (Pa)	$E_{Sub}$ (Pa)	k(N/m <sup>3</sup> )
7/25/2006	4.60E+10	6.00E+10	3.09E+08	9.88E+07
8/1/2006*	2.47E+10	2.41E+10	-	6.51E+07
8/9/2006	3.52E+10	3.91E+10	2.61E+08	8.63E+07
8/15/2006	3.01E+10	3.22E+10	2.40E+08	8.08E+07
10/10/2006	3.45E+10	2.87E+10	2.51E+08	8.36E+07
11/7/2206	3.24E+10	3.70E+10	2.46E+08	8.23E+07

Table 4-10 Moduli of Pavement System (Test Item S3)

S3				
Date	$E_{OL}$ (Pa)	$E_{UL}$ (Pa)	$E_{Sub}$ (Pa)	k(N/m <sup>3</sup> )
7/25/2006	4.19E+10	4.19E+10	3.05E+08	9.76E+07
8/1/2006*	2.59E+10	2.35E+10	-	7.41E+07
8/9/2006	4.06E+10	4.06E+10	2.56E+08	8.49E+07
8/15/2006	4.09E+10	4.09E+10	2.59E+08	8.57E+07
10/10/2006	3.30E+10	3.30E+10	2.52E+08	8.41E+07
11/7/2006	4.80E+10	4.80E+10	2.47E+08	8.26E+07

Average unit weights of structural sections 1, 2 and 3 are 150.8 1bf/ft<sup>3</sup>, 155.2 1bf/ft<sup>3</sup> and 154.7 1bf/ft<sup>3</sup> respectively, which could be found from project report [20]. The mass terms used in the analytical model are mass per unit area of overlay and underlay; by multiplying with thicknesses obtained from Table 2-1, the mass terms are as Table 4-11 shows.

Table 4-11 Masses of Overlay and Underlay

	Section 1		Section 2		Section 3	
	N1	S1	N2	S2	N3	S3
H <sub>1</sub> (m)	0.217932	0.220726	0.188722	0.186436	0.143002	0.145034
H <sub>2</sub> (m)	0.160528	0.160528	0.187198	0.19431	0.247904	0.24892
m <sub>1</sub> (kg/m <sup>2</sup> )	548.1818	555.2098	468.2382	462.5664	350.2205	355.197
m <sub>2</sub> (kg/m <sup>2</sup> )	387.7682	387.7682	465.3873	483.0683	614.3235	616.8412

Then parameters about the bonding condition between the overlay and the underlay will be considered, interface parameter  $l$  set in BAKFAA is 1, so  $K_s$  is close to infinity. The range of



$K_s$  is from 10 to  $10^5$  MN/m<sup>2</sup>[19], so one can try  $10^2$  MN/m<sup>2</sup> at first, then other values could be assigned to see if there are significant value changes in dynamic response terms.

#### 4.3 NUMERICAL METHODOLOGY AND ITS VALIDATION

From section 3.3, deflection expressions under Fourier transform of overlay and underlay are:

$$W_1 = \frac{\tilde{F} b}{ab - \frac{h_1^2 h_2^2 K_s^2}{16} (\xi^3 + \zeta^3)^2}$$

$$W_2 = \frac{-\frac{h_1 h_2 K_s i}{4} (\xi^3 + \zeta^3) \tilde{F}}{ab - \frac{h_1^2 h_2^2 K_s^2}{16} (\xi^3 + \zeta^3)^2}$$

in which,

$$a = D_1 (\xi^2 + \zeta^2)^2 - \frac{h_1^2 K_s}{4} i (\xi^3 + \zeta^3) - m_1 (\Omega - V \xi)^2 + k_1,$$

$$b = D_2 (\xi^2 + \zeta^2)^2 + \frac{h_2^2 K_s}{4} i (\xi^3 + \zeta^3) - m_2 (\Omega - V \xi)^2 + k_2 + ic (\Omega - V \xi)$$

For  $F$ , external load expressions under Fourier transform were obtained in Chapter 3. For constant pressure, tandem dual axle load and tridem dual axle load are:

$$\tilde{F}_{\text{tandem}} = 2\pi P \frac{\sin \xi l_1}{\xi l_1} \frac{\sin \zeta l_2}{\zeta l_2} e^{-ix_0 \xi} e^{-iy_0 \zeta} (1 + e^{-id_a \xi}) (1 + e^{-id_t \zeta} + e^{-id_w \zeta} + e^{-i(d_t + d_w) \zeta}) \delta(\Omega)$$

$$\tilde{F}_{\text{tridem}} = 2\pi P \frac{\sin \xi l_1}{\xi l_1} \frac{\sin \zeta l_2}{\zeta l_2} e^{-ix_0 \xi} e^{-iy_0 \zeta} (1 + e^{-id_a \xi} + e^{-2id_a \xi}) (1 + e^{-id_t \zeta} + e^{-id_w \zeta} + e^{-i(d_t + d_w) \zeta}) \delta(\Omega)$$

On the other hand, for harmonic load, tandem dual axle load and tridem dual axle load are:

$$\begin{aligned} \tilde{F}_{\text{tandem}} &= 2\pi P \frac{\sin \xi l_1}{\xi l_1} \frac{\sin \zeta l_2}{\zeta l_2} e^{-ix_0 \xi} e^{-iy_0 \zeta} \left(1 + e^{-id_a \xi}\right) \left(1 + e^{-id_t \zeta} + e^{-id_w \zeta} + e^{-i(d_t + d_w) \zeta}\right) \delta(\Omega - \Omega_0) \end{aligned}$$

$$\begin{aligned} \tilde{F}_{\text{tridem}} &= 2\pi P \frac{\sin \xi l_1}{\xi l_1} \frac{\sin \zeta l_2}{\zeta l_2} e^{-ix_0 \xi} e^{-iy_0 \zeta} \left(1 + e^{-id_a \xi} + e^{-2id_a \xi}\right) \cdot \\ &\quad \left(1 + e^{-id_t \zeta} + e^{-id_w \zeta} + e^{-i(d_t + d_w) \zeta}\right) \delta(\Omega - \Omega_0) \end{aligned}$$

$W_1 e^{i\xi x'} e^{i\zeta y} e^{i\Omega t}$ ,  $W_2 e^{i\xi x'} e^{i\zeta y} e^{i\Omega t}$  are the kernel functions of Inverse Fourier Transform. The

ultimate deflection expressions needed are:

$$w_1 = \frac{1}{8\pi^3} \int_{-\infty}^{\infty} \int_{-\infty}^{\infty} \int_{-\infty}^{\infty} W_1 e^{i\xi x'} e^{i\zeta y} e^{i\Omega t} d\xi d\zeta d\Omega \quad (4.2)$$

$$w_2 = \frac{1}{8\pi^3} \int_{-\infty}^{\infty} \int_{-\infty}^{\infty} \int_{-\infty}^{\infty} W_2 e^{i\xi x'} e^{i\zeta y} e^{i\Omega t} d\xi d\zeta d\Omega \quad (4.3)$$

when load condition is constant pressure, giving

$$\int_{-\infty}^{\infty} \delta(\Omega) e^{i\Omega t} d\Omega = 1 \quad (4.4)$$

So the deflection expression due to tandem axle load turns into

$$\begin{aligned} w_1(x', y) &= \frac{1}{4\pi^2} \int_{-\infty}^{\infty} \int_{-\infty}^{\infty} \frac{P \frac{\sin \xi l_1}{\xi l_1} \frac{\sin \zeta l_2}{\zeta l_2} e^{-ix_0 \xi} e^{-iy_0 \zeta} \left(1 + e^{-id_a \xi}\right)}{ab - \frac{h_1^2 h_2^2 K_s^2}{16} (\xi^3 + \zeta^3)^2} \\ &\quad \cdot \left(1 + e^{-id_t \zeta} + e^{-id_w \zeta} + e^{-i(d_t + d_w) \zeta}\right) b e^{i\xi x'} e^{i\zeta y} d\xi d\zeta \\ w_2(x', y) &= -\frac{1}{4\pi^2} \int_{-\infty}^{\infty} \int_{-\infty}^{\infty} \frac{P \frac{\sin \xi l_1}{\xi l_1} \frac{\sin \zeta l_2}{\zeta l_2} e^{-ix_0 \xi} e^{-iy_0 \zeta} \left(1 + e^{-id_a \xi}\right)}{ab - \frac{h_1^2 h_2^2 K_s^2}{16} (\xi^3 + \zeta^3)^2} \\ &\quad \cdot \left(1 + e^{-id_t \zeta} + e^{-id_w \zeta} + e^{-i(d_t + d_w) \zeta}\right) \cdot \frac{h_1 h_2 K_s i (\xi^3 + \zeta^3)}{4} e^{i\xi x'} e^{i\zeta y} d\xi d\zeta \end{aligned} \quad (4.5)$$

(4.6)

On the other hand, if the tandem axle load is harmonic, then deflection is

$$w_1(x', y, t) = \frac{1}{4\pi^2} \int_{-\infty}^{\infty} \int_{-\infty}^{\infty} \frac{P \frac{\sin \xi l_1}{\xi l_1} \frac{\sin \zeta l_2}{\zeta l_2} e^{-ix_0 \xi} e^{-iy_0 \zeta} (1 + e^{-id_a \xi})}{ab - \frac{h_1^2 h_2^2 K_s^2}{16} (\xi^3 + \zeta^3)^2} \cdot (1 + e^{-id_t \xi} + e^{-id_w \zeta} + e^{-i(d_t + d_w) \zeta}) b e^{i\xi x'} e^{i\zeta y} e^{i\Omega_0 t} d\xi d\zeta \quad (4.7)$$

$$w_2(x', y, t) = -\frac{1}{4\pi^2} \int_{-\infty}^{\infty} \int_{-\infty}^{\infty} \frac{P \frac{\sin \xi l_1}{\xi l_1} \frac{\sin \zeta l_2}{\zeta l_2} e^{-ix_0 \xi} e^{-iy_0 \zeta} (1 + e^{-id_a \xi})}{ab - \frac{h_1^2 h_2^2 K_s^2}{16} (\xi^3 + \zeta^3)^2} \cdot (1 + e^{-id_t \xi} + e^{-id_w \zeta} + e^{-i(d_t + d_w) \zeta}) \cdot \frac{h_1 h_2 K_s i (\xi^3 + \zeta^3)}{4} e^{i\xi x'} e^{i\zeta y} e^{i\Omega_0 t} d\xi d\zeta \quad (4.8)$$

where  $a = D_1 (\xi^2 + \zeta^2)^2 - \frac{h_1^2 K_s}{4} i (\xi^3 + \zeta^3) - m_1 (\Omega_0 - V\xi)^2 + k_1$ ,

$b = D_2 (\xi^2 + \zeta^2)^2 + \frac{h_2^2 K_s}{4} i (\xi^3 + \zeta^3) - m_2 (\Omega_0 - V\xi)^2 + k_2 + ic (\Omega_0 - V\xi)$

according to the results of [26].

For tridem dual axle load, the deflection expressions have similar forms as equations (4.5) to (4.8), the force term in integrands are not listed here.

Except deflection, other dynamic responses such as stress and strain are also of concern.

From elastic theory,

$$\sigma_x(x', y, t) = -\frac{Ez}{1-\nu^2} \left( \frac{\partial^2 w}{\partial x'^2} + \nu \frac{\partial^2 w}{\partial y^2} \right) \quad (4.9)$$

$$\sigma_y(x', y, t) = -\frac{Ez}{1-\nu^2} \left( \frac{\partial^2 w}{\partial y^2} + \nu \frac{\partial^2 w}{\partial x'^2} \right) \quad (4.10)$$

Then deflection expressions could be substituted to equations (4.9) and (4.10),

$$\sigma_{xi}(x', y, t) = \frac{1}{8\pi^3} \frac{Ez}{1-\nu^2} \int_{-\infty}^{\infty} \int_{-\infty}^{\infty} \int_{-\infty}^{\infty} (\xi^2 + \nu \zeta^2) W_i e^{i\xi x'} e^{i\zeta y} e^{i\Omega t} d\xi d\zeta dt \quad (4.11)$$

$$\sigma_{yi}(x', y, t) = \frac{1}{8\pi^3} \frac{Ez}{1-\nu^2} \int_{-\infty}^{\infty} \int_{-\infty}^{\infty} \int_{-\infty}^{\infty} (\nu \xi^2 + \zeta^2) W_i e^{i\xi x'} e^{i\zeta y} e^{i\Omega t} d\xi d\zeta dt \quad (4.12)$$

where  $i=1, 2$ . When substituting different load terms  $\tilde{F}$ , of tandem or tridem axle, and of constant or harmonic load, equations (4.11) and (4.12) describe all the situations considered in this paper. Strain expressions then are obtained by constitutive relationship of elasticity.

#### 4.3.1 METHODOLOGY

From all the dynamic responses expressions listed above it is noticed that they are essentially the same problem, which is a two-dimensional numerical integration problem with several parameters  $x', y, t$ , which could describe dynamic response of any positions on slabs, both underlay and overlay, and at any time it happened during a pass. Differences of mechanical properties between passes of the same day are ignored. For passes of different days, the mechanical parameters are changed, which ensure modeling conducted in this paper to match the data recorded by instruments.

The fundamental idea to solve numerical integration problem is a matter of discretion. 1-D numerical integration could be done by many methods, such as Simpson's rule and the Trapezoidal rule. Many multiple-dimensional numerical integration methods, which are available in references like Nakamura [34], usually separate the multiple-dimension integration to a combination of several 1-D integrations, and each 1-D integration is solved by approximation methods including those mentioned above. The procedure is such as:

$$\int_a^b \int_{c(x)}^{d(x)} f(x, y) dy dx = \int_a^b g(x) dx \quad (4.13)$$

where  $g(x) = \int_{c(x)}^{d(x)} f(x, y) dy$ , we can solve 1-D integration in sequence.

However, there is another approach to treat integration on plane, which is to use designed formula for divided sub-planes. An important thing in numerical integration that may affect the accuracy is the singularity problem. Therefore, the algorithm used should moderate or eliminate

the influence of those singularities. **quad2d**, a function in MATLAB, now satisfies all the requirements, and will be performed to do quadrature in this paper. According to Shampine [35], **quad2d** needs the integration field to be a generalized rectangle, for which one of the integration domains is constant and the other is vectorized as function of variable of constant domain. **quad2d** could deal with oscillated function with counted discontinuities, since it is developed in collaboration with function **quadgk**, which is 1-D adaptive quadrature based on a Gauss-Kronrod pair (15<sup>th</sup> and 7<sup>th</sup> order formulas), known as a way to integrate functions that are singular at finite endpoints. **Integral2** is also used to perform numerical calculation, and performs even better than **quad2d**.

Besides, Inverse Fourier Transform is improper integration problem. As is mentioned in Nakamura [34], the value of kernel function must be at least 0 when the variable goes to infinity, which all the dynamic response expressions in this thesis satisfy. Then,  $X$ ,  $Y$  could be used to replace infinity, as equations (4.14) and (4.15) show,

$$I = \int_{-\infty}^{\infty} \int_{-\infty}^{\infty} f(x, y) dx dy \quad (4.14)$$

$$I = \int_{-Y}^Y \int_{-X}^X f(x, y) dx dy \quad (4.15)$$

Relatively small values could be found based on the criteria that when  $X$  is increased to  $1.5X$ ,  $I$  should not change, and when  $X$  is changed to  $X/1.5$ ,  $I$  could change simultaneously;  $Y$  is fixed during the whole procedure [34]. Vice versa for  $Y$  when  $X$  is fixed.

### 4.3.2 VERIFICATION WITH EXAMPLE

After the methodology is decided, an example provided by Kim [7] is run using the MATLAB program, and a comparison is conducted with the dynamic response diagram in the reference Kim [7]. Stress expression will come from equations (4.11) and (4.12), assigning  $K_s$  to 0, which represents the unbonded condition. If the result run in this thesis reasonably matches that

from Kim [7], it can roughly demonstrate the rationality of the model. Parameters obtained from Kim [7] are listed in Table 4-12, together with setting of the remaining parameters to 0 except  $k_2$ , which is used to avoid denominator equaling to 0. The dynamic response chosen to do comparison here is the longitudinal stress on the surface of slab. Stress distribution is along the moving axle and at  $y=0.028\text{m}$ .

Table 4-12 Parameters Provided by Kim [7]

$E_I(\text{pa})$	$\nu_I$	$M_I(\text{kg/m}^2)$	$H_I(\text{m})$	$K_s(\text{N/m}^3)$	$V(\text{m/s})$	$P(\text{N})$
2.756E+10	0.15	708	0.3048	0	11.11	20E+3
$d_l(\text{m})$	$d_w(\text{m})$	$d_a(\text{m})$	$D_2(\text{N}^*\text{m})$	$h_2(\text{m})$	$m_2(\text{kg/m}^2)$	$k_I(\text{N/m}^3)$
0.33	1.88	1.32	0	0	0	136E+6
$D_I(\text{N}^*\text{m})$	$L_I(\text{m})$	$l_2(\text{m})$	$k_2(\text{N/m}^3)$	$z(\text{m})$	$c(\text{Pa}^*\text{s/m})$	
6.6531E+7	0.1778/2	0.2032/2	1	0.1524	0	

The expression for longitudinal stress is:

$$\sigma_{x'i}(x', y, t) = \frac{1}{4\pi^2} \frac{Ez}{1-\nu^2} \int_{-\infty}^{\infty} \int_{-\infty}^{\infty} \frac{P \frac{\sin \xi l_1}{\xi l_1} \frac{\sin \zeta l_2}{\zeta l_2} e^{-ix_0 \xi} e^{-iy_0 \zeta}}{ab - \frac{h_1^2 h_2^2 K_s^2}{16} (\xi^3 + \zeta^3)^2} \cdot \left(1 + e^{-id_a \xi}\right) \left(1 + e^{-id_l \zeta} + e^{-id_w \zeta} + e^{-i(d_l + d_w) \zeta}\right) be^{i\xi x'} e^{i\zeta y} d\xi d\zeta \quad (4.16)$$

From which it is noticed that the singularities will be on two lines,

$$\xi = 0$$

$$\zeta = 0$$

For the other factor of the denominator,  $ab - \frac{h_1^2 h_2^2 K_s^2}{16} (\xi^3 + \zeta^3)^2$ , we cannot plot a surface

of it to see whether there are any zeros because it is a complex function, but a set of individual

points  $(\xi, \zeta)$  could be substituted in the denominator to check for zeros. This procedure is also done by MATLAB, and the result is no zeros.

Next step is to decide the upper and lower boundaries of integration; here  $(-15, 15)$  is enough for both dimensions. The result is depicted in Figure 4-1; the  $x$  axis represents the distance away from the center line of the tandem axle. As can be seen, it is reasonably consistent with the lightest line of Figure 4-2 from Kim [7], which had entirely the same situation as that depicted in Figure 4-1.

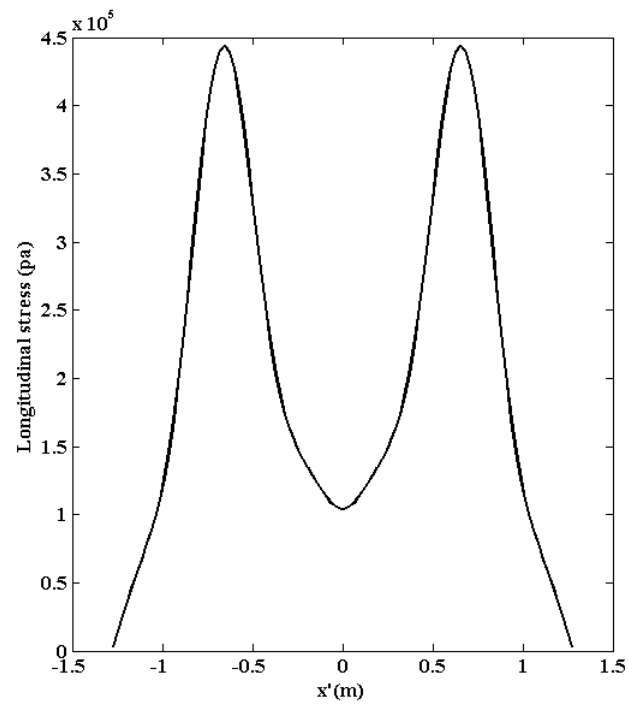


Figure 4-1 Stress Distribution along Moving Axle

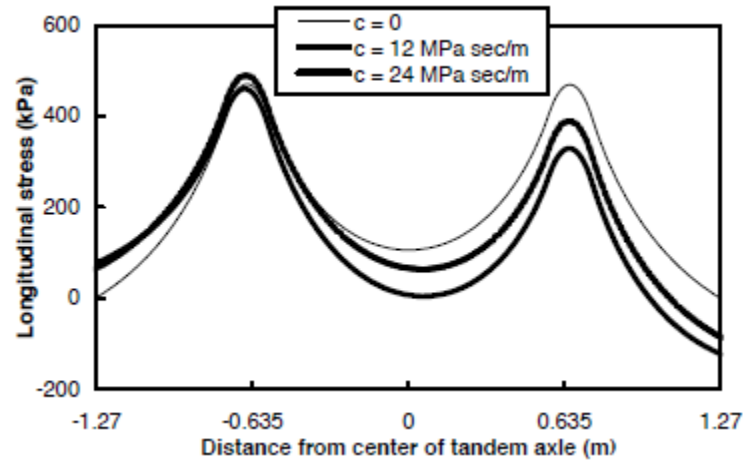


Figure 4-2 Stress Distribution along Moving Axle, from Kim [7]

These two diagrams demonstrate that if there isn't any viscosity considered in modeling, the stress response is symmetric with respect to the center line of loads. And the methodology is considered acceptable to be used in the following numerical calculations.

#### 4.4 NUMERICAL CALCULATION ANALYSIS

According to Stoffels [20], vehicle speed in the NAPTF CC4 unbonded overlay project is fixed at 3 mile/hour. Failure load is also a constant value, which is 50,000 lbs per combined wheel, (222411N/combined wheel), so these two factors are excluded from the following numerical investigation. However, load type, mechanical properties of each item, and positions of embedded strain gage should be taken into consideration. The logic flow chart is shown in Figure 4-3.



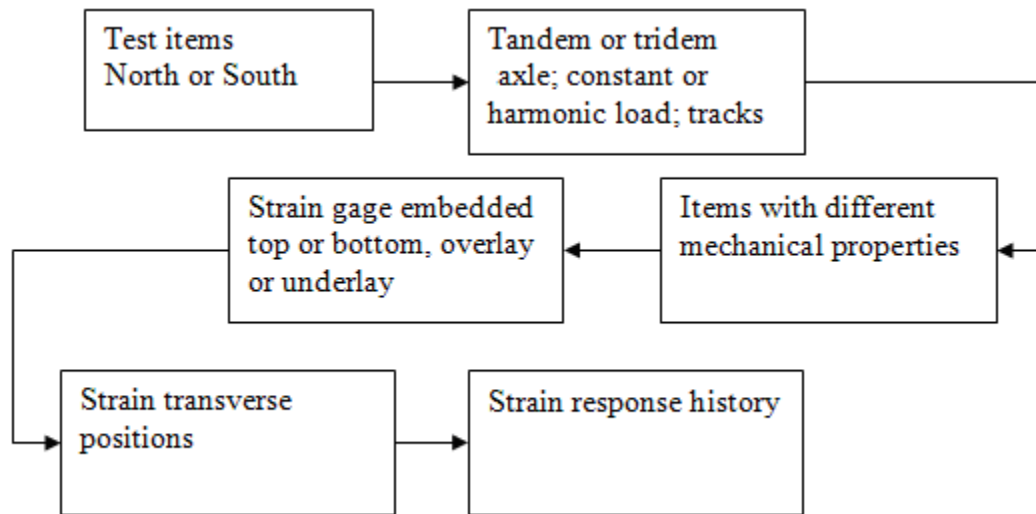


Figure 4-3 Numerical Investigation Flow Chart

The following sections will consider some strain responses with different parameters, which may contribute to the matching process of the model with strain gage responses. The parameters to be considered are shear reaction modulus  $K_s$ , frequency of harmonic load, as well as the viscosity term for the layers beneath the underlay slab.

#### 4.4.1 PARAMETER STUDY OF $K_s$

The top strain gage data from North Test Item 1 (N1) under track 0 is chosen to check the accuracy of modeling.

Table 4-13 Parameter Values (7/25/2006, Test Item N1)

$E_1(\text{pa})$	$h_1(\text{m})$	$v_1$	$D_1$	$m_1(\text{kg/m}^2)$	$k_1(\text{N/m}^3)$	$V(\text{m/s})$	$K_s(\text{N/m}^3)$
4.14E+10	0.2179	0.15	36515228	548.1818	9.48E+07		
$E_2(\text{pa})$	$h_2(\text{m})$	$v_2$	$D_2$	$m_2(\text{kg/m}^2)$	$k_2(\text{N/m}^3)$	1.341	varied
4.77E+10	0.1605	0.15	16813010	387.7682	7.60E+07		

According to Kruntcheva [19],  $K_s$  more than  $10^6 \text{ MN/m}^3$  is considered to be a fully bonded situation. From Figure 4-4, it can be concluded that bonding condition significantly affects strain responses ( $K_s$  is in units of  $\text{N/m}^3$ ); 0 represents strain right below the center of the outer tire of the last axle of a tridem axle load.

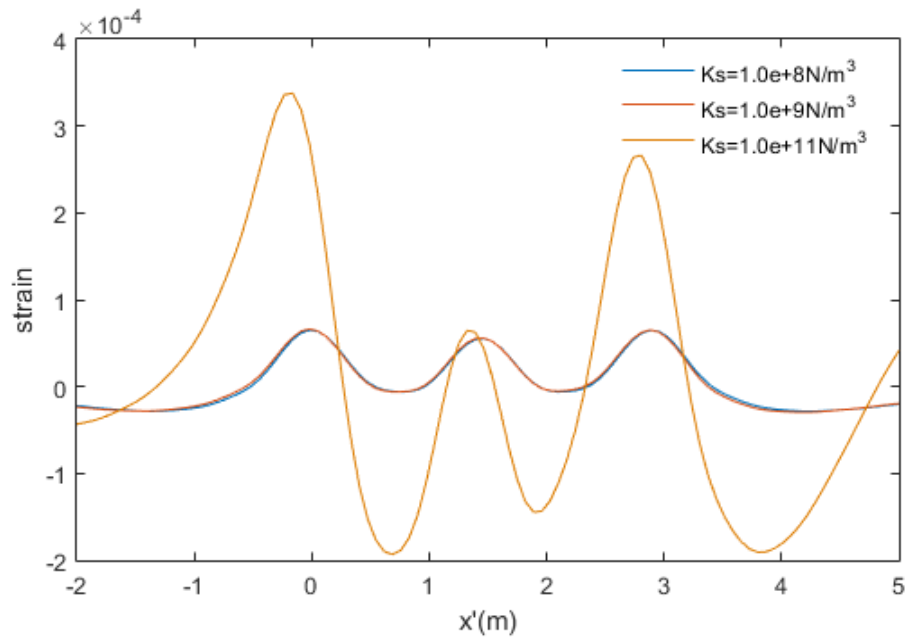


Figure 4-4 Parameter Study of  $K_s$  with the other Parameters as shown in Table 4-11 with Constant Load

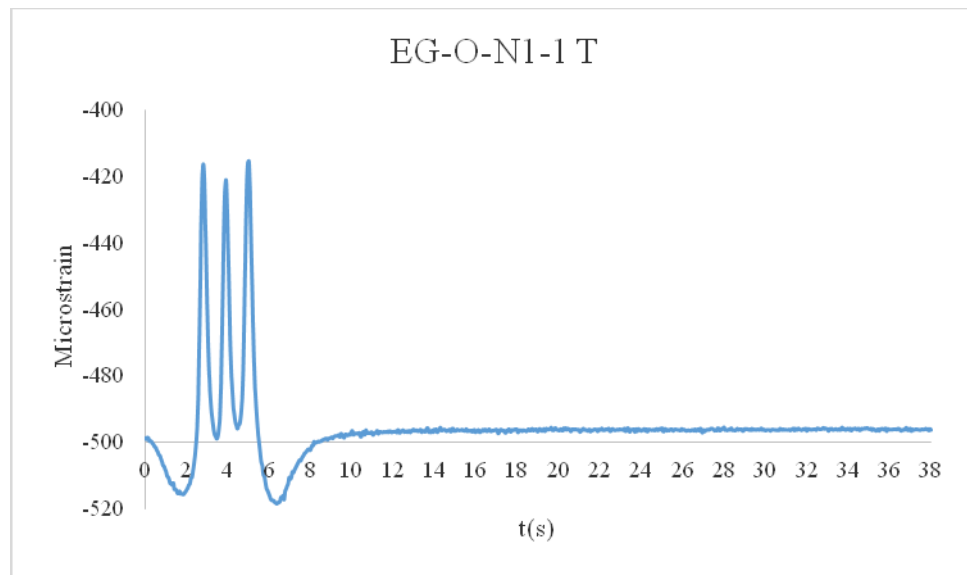


Figure 4-5 Data of EG-O-N1-1 T, randomly selected track 0 pass on 7/25/2006 (embedded gage, overlay, test item N1, gauge 1, top of slab)

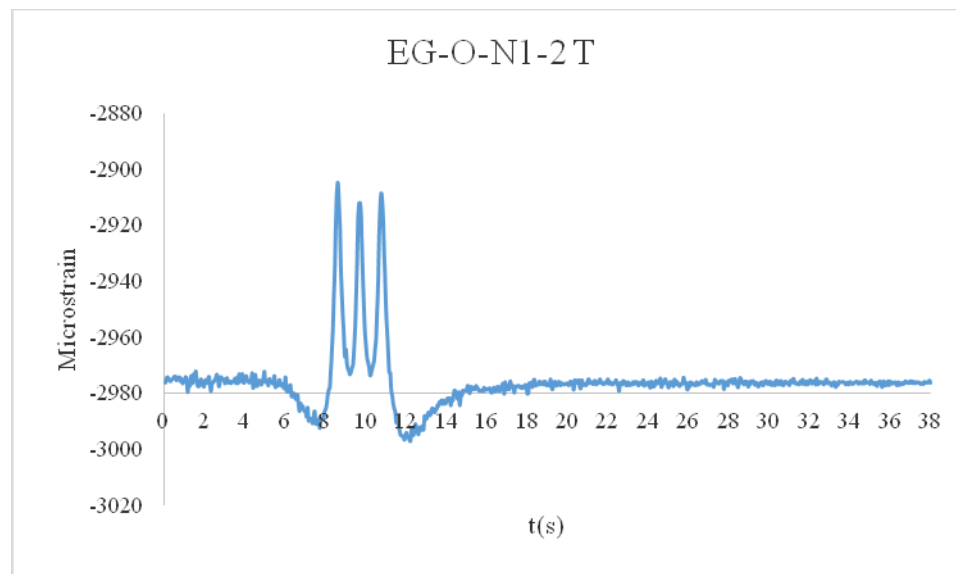


Figure 4-6 Data of EG-O-N1-2 T, randomly selected track 0 pass on 7/25/2006 (embedded gage, overlay, test item N1, gauge 2, top of slab)

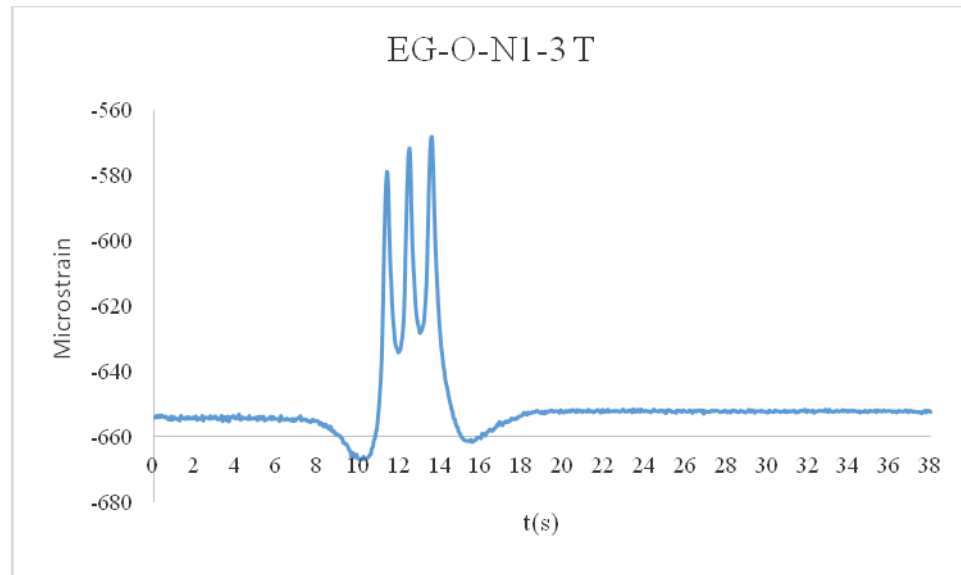


Figure 4-7 Data of EG-O-N1-3 T, randomly selected track 0 pass on 7/25/2006 (embedded gage, overlay, test item N1, gauge 3, top of slab)

While in strain gage history data of N1, as shown in Figure 4-4 to 4-7, the range of strain data is about  $10^{-4}$ , to which the curves of  $Ks$  equal to  $1.0E+8$  N/m<sup>3</sup> and  $1.0E+9$  N/m<sup>3</sup> are closer. It is assumed that  $Ks=1.0E+8$  for the item N1 and any of the other items, and assumed that the interface condition will not change with loading pass processing. From appendix A, coordinates of strain gages EG-O-N1-1 T, EG-O-N1-2 T, and EG-O-N1-3 T are (338.75, -17.38(assumed)), (363.25, -17.38) and (376.25, -17.67), respectively, with units in feet. From this, it can be confirmed that the y coordinate is that of interest; however, the x coordinate can't be assured after the moving load has begun. Therefore, it was assumed that the first peak happened when the first axle load passed the embedded gage. The results run by the model are presented as Figures 4-8 to 4-10; the response distributions are of accordance. They all have three peaks which are caused by the three axles, pre-stress area, post stress area, and partial recovery between axles, as that described by Singh [27]. But constant load also makes no differences in the calculated responses in item N1 at the locations of strain gages EG-O-N1-1 T, EG-O-N1-2 T, and EG-O-N1-3 T.

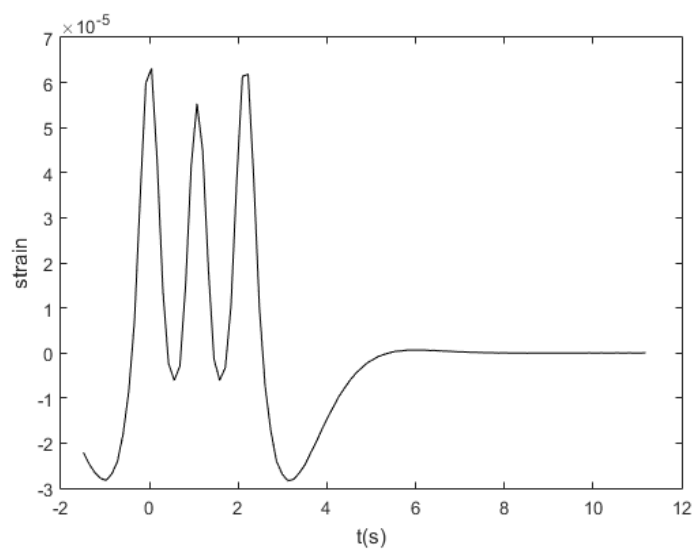


Figure 4-8 Model Result Corresponding to EG-O-N1-1 T

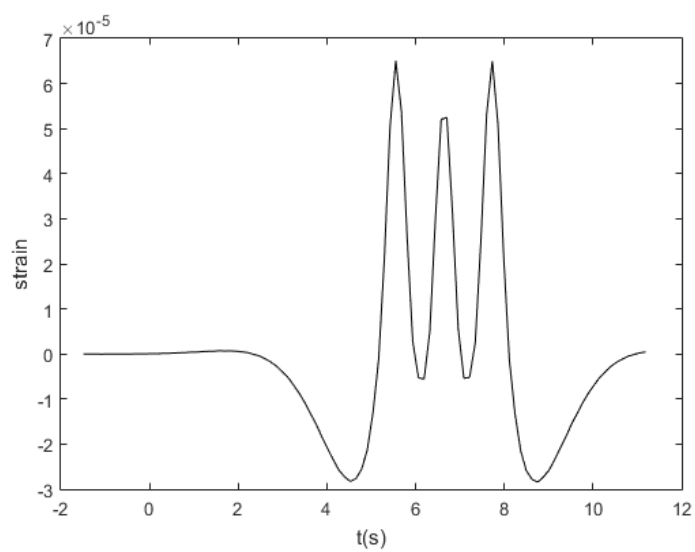


Figure 4-9 Model Result Corresponding to EG-O-N1-2 T

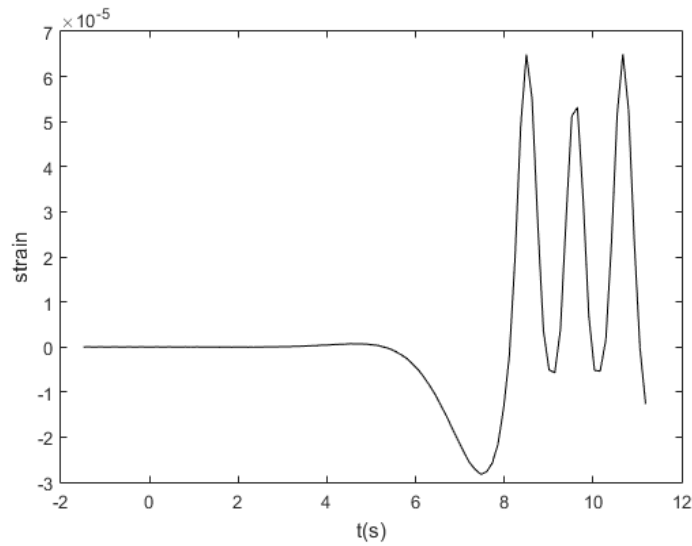


Figure 4-10 Model Result Corresponding to EG-O-N1-3 T

#### 4.4.2 PARAMETER STUDY OF LOAD FREQUENCY

All of the preceding discussion is under constant moving stress, so the response distribution shapes are always the same by all the three strain gages. If harmonic moving load is of consideration because of the effect of mechanical vibration given by traffic engine and applied by wheel rotation, as well as toughness of pavement itself, the top strain response of overlay is both related to the distance between load and the point of interest, and to time.

Figure 4-11 shows the dynamic response due to harmonic loads with different frequencies. The styles are random with the frequency increasing, except the one whose frequency is 0.1, which has a decaying trend of three peak strains and the values of the peak strains are much closer to those of the strain gages. Because of harmonic load rather than constant load, the strain response could show differences at different locations on slab. If the assigned frequency equals to 0.1, then the results of Figure 4-8 to 4-10 change to those in Figures 4-12 to 4-14.

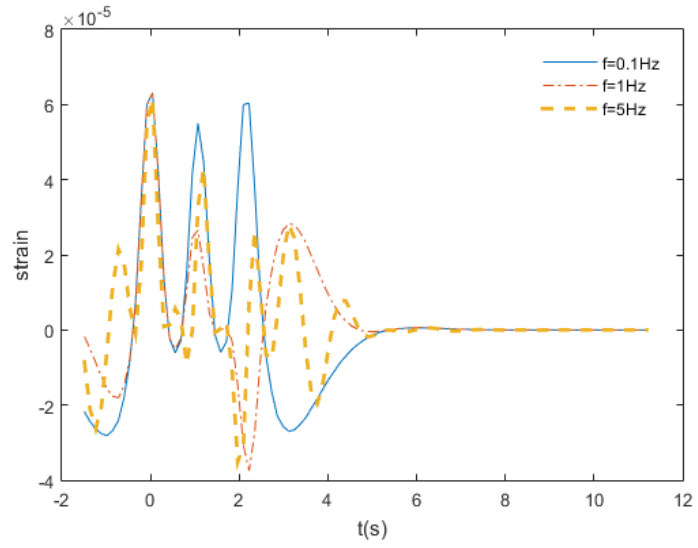


Figure 4-11 Dynamic Responses Due to Harmonic Loads with Different Frequencies (unit Hz)

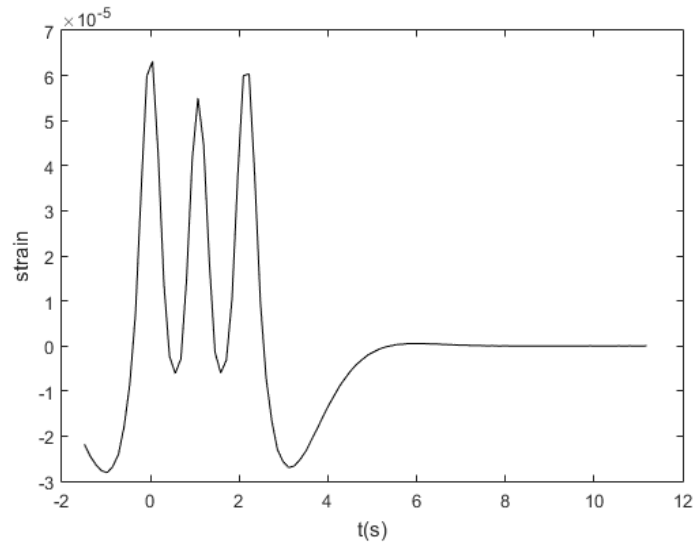


Figure 4-12 Model Result Corresponding to EG-O-N1-1 T

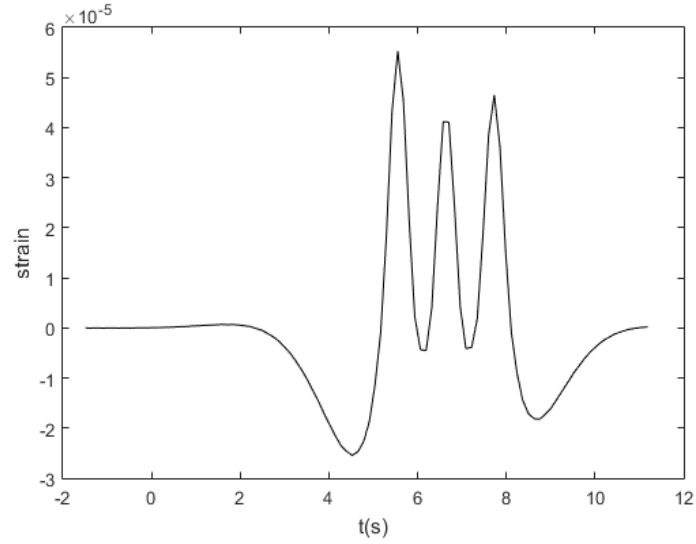


Figure 4-13 Model Result Corresponding to EG-O-N1-2 T

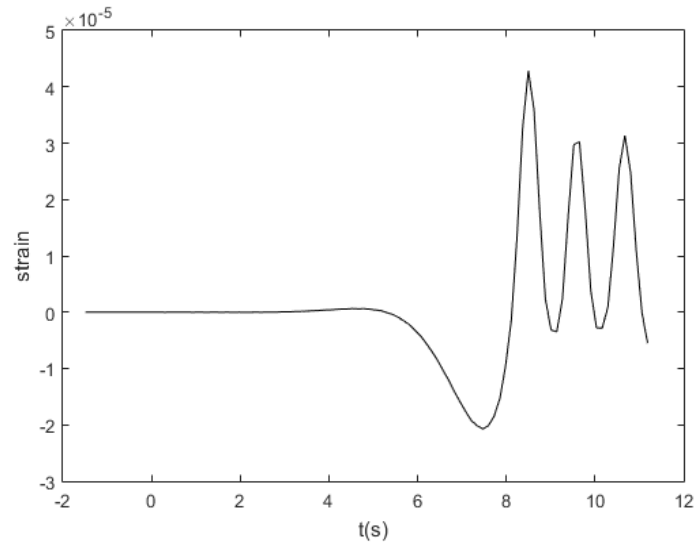


Figure 4-14 Model Result Corresponding to EG-O-N1-3 T

The dynamic responses of different fixed points on the slab are not the same when considering the load to be harmonic, and they show different types of shapes in strain distribution along time, which is much more similar to the records from the strain gages. In addition, not only the shape, but the absolute values of the strain become less than that of considering load to be constant, which also illustrate the energy consuming during load processing is larger of exerting



harmonic load than that of constant pressure. It can be concluded that load type is a very important factor to consider in modeling.

#### 4.4.3 PARAMETER STUDY OF VISCOSITY

Viscosity  $c$  is yielded to 0 in previous studies; however, it is necessary to consider in an overlay pavement system, as there is only partial recovery of deformation right after the load passes, which indicates a delay of recovery or non-reversible deformation happens. Viscosity could be considered by using a parameter of viscous damping constant  $c$ , while material damping could also be considered here, which is ignored and the details could be found in Kim [7]. When  $K_s$  is assigned to a relatively small value,  $c$  doesn't have much contribution to dynamic response, which can be seen in Figure 4-15. While  $K_s$  increases,  $c$  shows significant contribution to dynamic response, as Figure 4-16 shows.

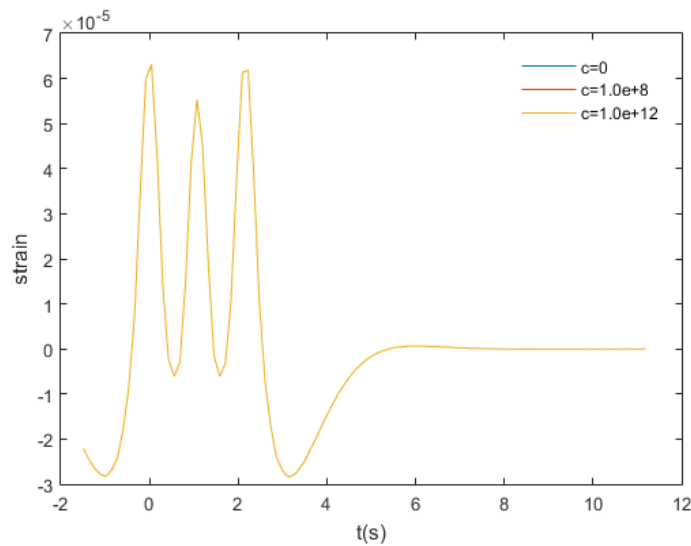


Figure 4-15 Strain Varies with  $c$  when  $K_s=1.0E+8$

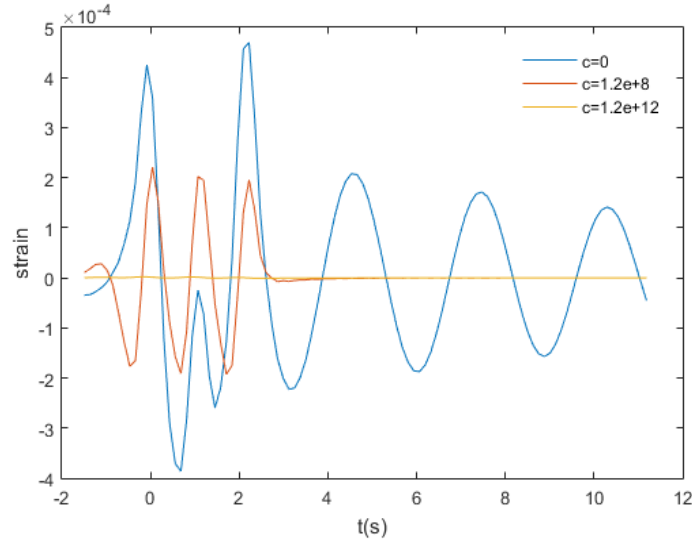
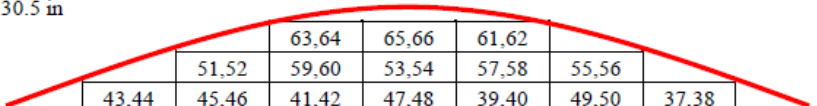


Figure 4-16 Strain Varies with  $c$  when  $K_s=1.0E+12$

#### 4.4.4 ACCORDANCE CHECK

The model is conformed to the most beneficial situation according to the parameter studies to check the accuracy, which indicates that constant load, small viscosity,  $K_s$  equal to  $1.0E+8$ ,  $c$  assigned to 0 and bottom strains of overlay are of interest (for bottom strain run by model, it is the same magnitude as top strain but with a negative sign). Although there are large amounts of data from every strain gage from every pass on each day, the comparison step needs both the backcalculation results for parameters in the analytical model and the load test record. As an example with timely and consistent data available for both the strain gages and HWD, the strain gage data for Test Item S1 at the bottom of the overlay for the dates 7/25/2006, 8/1/2006, and 8/9/2006 are appropriate to choose. On the other hand, dynamic responses of each item of a particular day, 7/25/2006, will also be checked, which may make the accordance check be of larger range.

Table 4-14 Wander Pattern and Load Centerline of Every Track by Yeh [22]

Track Frequencies	6.1%	9.1%	12.1%	15.2%	15.2%	15.2%	12.1%	9.1%	6.1%
Wander Pattern Diagram	Normal Distribution $\sigma = 30.5$ in								
									
		43,44	45,46	41,42	47,48	39,40	49,50	37,38	
	19,20	35,36	21,22	33,34	23,24	31,32	25,26	29,30	27,28
	1,2	17,18	3,4	15,16	5,6	13,14	7,8	11,12	9,10
Track Number	-4	-3	-2	-1	0	1	2	3	4
North Loading Centerline Location (ft)	-18.167	-17.313	-16.458	-15.604	-14.750	-13.896	-13.042	-12.188	-11.333
South Loading Centerline Location (ft)	11.333	12.188	13.042	13.896	14.750	15.604	16.458	17.313	18.167

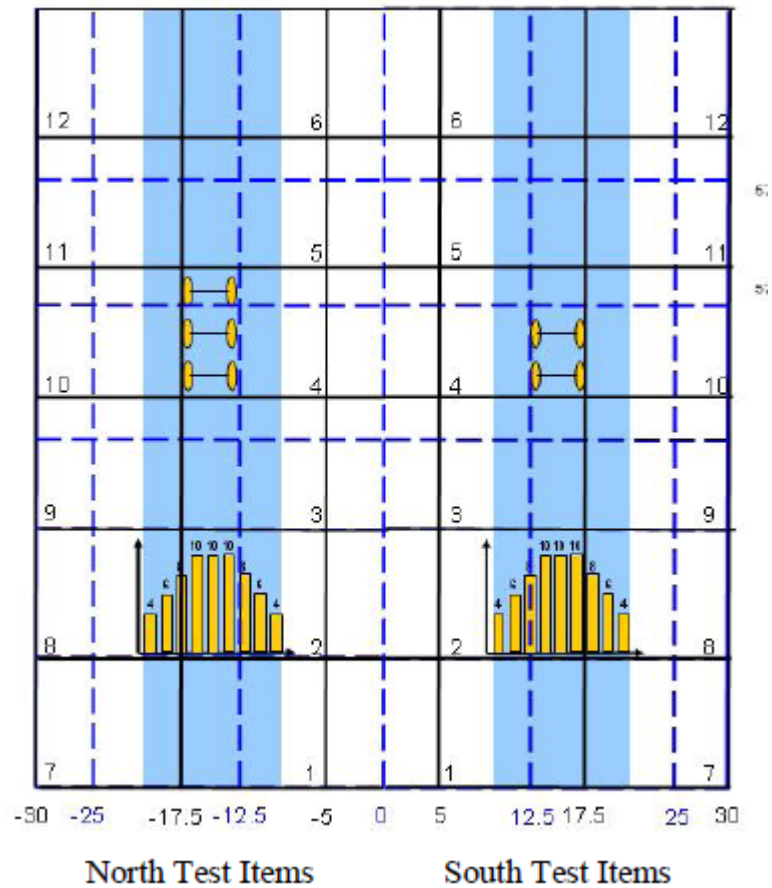


Figure 4-17 Loading Plan and Coordinate Set by Yeh [22]

Data from the strain gages always included residual strain from the beginning of the test, while only peak strain relative to residual strain and strain range are of interest. It is noticed that when the strain is calculated based on elastic theory, strain is linearly increasing with the distance

away from centroid of the section, which means the vertical position of strain gage is very important. The thickness of slab is about 20cm, and strain gage itself is about 2cm, which is also needed to be entirely covered by concrete. However, no compensation of embedment depth is made here. The comparison example is shown in Table 4-15; because of the part of the existing residual strain which existed before the failure load test, we can only compare the relative peak strain and the range of strain. Peak strain is calculated relative to baseline value, which is the average value of all the strain data since steady state. To specify, average values are obtained from the data from 10s to 38s, from 16s to 38s, and from 18s to 38s. On the other hand, strain range is just the difference between the maximum and minimum values of strain.

Table 4-15 Comparison between Calculated Results and Overlay Bottom Strain for Test Item S1, with Varied Dates

7/25/2006	EG-O-S1-1 B	EG-O-S1-2 B	EG-O-S1-3 B	Calculated Results
Relative Peak Strain	-54.73	-80.78	-57.58	-68.45
Strain Range	72.43	100.24	81.25	93.92
8/1/2006	EG-O-S1-1 B	EG-O-S1-2 B	EG-O-S1-3 B	Calculated Results
Relative Peak Strain	-31.34	-89.75	-64.77	-98.03
Strain Range	55.39	65.87	36.44	134.48
8/9/2006	EG-O-S1-1 B	EG-O-S1-2 B	EG-O-S1-3 B	Calculated Results
Relative Peak Strain	-29.31	-72.12	-51.32	-85.87
Strain Range	57.68	99.57	78.52	117.82

Data of the same gage varies in a large range, as indicated in Yeh [22]. However, from Table 4-15, one can conclude that the calculated results are closer to the gage data of the EG-O-S1-2 B than any other ones, and further studies should be done which consider the load as harmonic load, or viscosity of layers under slabs, to get more accurate results.

Then strain responses of each item of the date 7/25/2006 are to be checked. The strain of each gage of one pass can be found in appendix C, as well as the results calculated by the models. For the majority of the test items, the peak strains are acceptable but not so as the strain range, because strain responses calculated are always larger than those recorded. And for some of the test items, both peak strain and strain range are not comparable, which may result from the strain gage embedment depth, harmonic load effect or viscosity effect.

Table 4-16 Comparison between Calculated Results and Strain of Every Item of Date 7/25/2006

N1	EG-O-N1-1 T	EG-O-N1-2 T	EG-O-N1-3 T	Calculated Result
Relative Peak Strain	80.77	71.77	83.71	74.73
Strain Range	103.09	92.56	98.64	112.36
N2	EG-O-N2-1 T	EG-O-N2-2 T	EG-O-N2-3 T	Calculated Result
Relative Peak Strain	61.24	-	-	75.6
Strain Range	70.31	81.14	-	105.7
N3	EG-O-N3-1 T	EG-O-N3-2 T	EG-O-N3-3 T	Calculated Result
Relative Peak Strain	71.38	79.85	-	111.4
Strain Range	85.71	96.51	-	151.67
S1	EG-O-S1-1 T	EG-O-S1-2 T	EG-O-S1-3 T	Calculated Result
Relative Peak Strain	-	60.28	79.08	68.40
Strain Range	-	74.42	96.36	93.90
S2	EG-O-S2-1 T	EG-O-S2-2 T	EG-O-S1-3 T	Calculated Result
Relative Peak Strain	46.13	54.29	66.57	80.72
Strain Range	55.77	62.68	76.18	110.77
S3	EG-O-S3-1 T	EG-O-S3-2 T	EG-O-S3-3 T	Calculated Result
Relative Peak Strain	68.69	58.30	98.34	121.5
Strain Range	89.09	68.77	129.63	164.71

## Chapter 5 CONCLUSION

### 5.1 SUMMARY

A full-scale accelerated pavement test on unbonded concrete overlays was conducted in 2006 to 2009, sponsored by the IPRF (Innovative Pavement Research Foundation), and performed at the Federal Aviation Administration (FAA) National Airfield Pavement Test Facility (NAPTF). Extensive strain gage data was collected by embedded strain gages both in the overlay and the underlay, due to tridem dual and tandem dual axle loads in a controlled distribution of wander paths. It provided new data and information, which has been used in this work to develop a concrete overlay pavement model in a manner that was not done before.

A semi-analytical model was conducted in this thesis to simulate dynamic behavior, specifically designed for airfield concrete overlay pavements, with consideration of multi-axle moving loads. Within the concrete overlay pavement model, interface condition is important to define. The interface conditions, from fully bonded to fully unbonded conditions, have a significant influence on dynamic responses of the pavement system, especially for the overlay and the underlay, and may also affect the corresponding performance and serviceability of pavement. . By using  $K_s$ , the shear reaction modulus, the interlayer could be seen virtually with its function remaining such that its shear stress could be obtained by multiplying  $K_s$  by relative displacement between overlay and underlay. All the bonding conditions could be described by relative displacement; when there is no relative displacement, the shear stress between the overlay and the underlay is also zero, which represents the unbonded condition. The fully bonded condition and partially bonded condition have similar mechanism. Characterization of load is another important factor affecting dynamic responses, so the loads were simulated as uniform

constant pressure and harmonic load, respectively. In addition, the viscosity property of pavement layers below the underlay was considered in the model.

Governing equations were compiled for overlay and underlay from equilibrium relations. To get an analytical solution, Fourier Transform was performed. The closed-form of Inverse Fourier Transform seldom works out for complex kernel functions. Alternatively, one of the numerical methods, self-adaptive numerical integration algorithm, was tried and successfully worked for the final result, and reached agreement with examples in the literature. Then the model was verified with embedded strain gage data, after parameter study of  $K_s$ , harmonic load frequency and viscosity, and strain calculated by the model showed characteristics of strain history very clearly.

## **5.2 DISCUSSION AND RECOMMENDATION**

There are many further objectives to achieve with the built model. First of all, it is commonly believed that the more strain is, the more distress it may bring about to pavement. From this model strain response of fixed points, where the strain gages are embedded, under different tracks, could be utilized to see how the strain peak (magnitude) is affected by the relative distance from loading path to the point investigated.

Additionally, effort may be taken to break the limitation coming from parameters which were obtained from backcalculation results. Although strain response is sensitive to change with interface condition changing, surface deflection is not, which is the source of HWD data. HWD data is often used to backcalculate the Young's modulus and reaction modulus of pavement system, and there will be no difference if we change the interface parameter of BAKFAA. But logically, the model as built could be used for further backcalculations if there is an appropriate methodology applied.

In this thesis, load is characterized as either constant pressure or uniform harmonic load within the tire contact area, but there is another method, may be more practical to simulate load, which is to see load as varied magnitude load. To solve the governing equation, a 3-D numerical function should be used. Or inertia term of aircraft should be taken into consideration later.

At last, for the pavement structure itself, the dowels from slab to slab were ignored, which may contribute some to the inaccuracy of the model. Further, neither the viscosity nor the environmental effects such as moisture and temperature were fully evaluated, which may be good topics to consider for further model enhancement.



## REFERENCES

- [1] Steyn, W. J. (2012). *Significant findings from full-scale accelerated pavement testing* (Vol. 433). Transportation Research Board.
- [2] Darestani, M. Y. (2007). Response of concrete pavements under moving vehicular loads and environmental effects.
- [3] Rollings, R. S. (1988). *Design of overlays for rigid airport pavements*. Federal Aviation Administration Washington DC.
- [4] Ioannides, A. M., & Khazanovich, L. (1998). General formulation for multilayered pavement systems. *Journal of transportation engineering*, 124(1), 82-90.
- [5] Sun, L. (2002). A closed-form solution of beam on viscoelastic subgrade subjected to moving loads. *Computers & structures*, 80(1), 1-8.
- [6] Kim, S. M., & Roesset, J. M. (1998). Moving loads on a plate on elastic foundation. *Journal of Engineering Mechanics*, 124(9), 1010-1017.
- [7] Kim, S. M., Won, M., & Frank McCullough, B. (2002). Dynamic stress response of concrete pavements to moving tandem-axle loads. *Transportation Research Record: Journal of the Transportation Research Board*, (1809), 32-41.
- [8] Zaman, M., Taheri, M. R., & Alvappillai, A. (1991). Dynamic response of a thick plate on viscoelastic foundation to moving loads. *International journal for numerical and analytical methods in geomechanics*, 15(9), 627-647.
- [9] Dieterman, H. A., & Metrikine, A. (1996). The equivalent stiffness of a half-space interacting with a beam. Critical velocities of a moving load along the beam. *EUROPEAN JOURNAL OF MECHANICS SERIES A SOLIDS*, 15, 67-90.
- [10] Cai, Y., Cao, Z., Sun, H., & Xu, C. (2009). Dynamic response of pavements on poroelastic half-space soil medium to a moving traffic load. *Computers and Geotechnics*, 36(1), 52-60.

- [11] Jiang, J. Q., Zhou, H. F., & Zhang, T. Q. (2006). Steady State Response of Infinite Plate on Visco-elastic Foundation Subjected to Moving Load [J]. *China Journal of Highway and Transport*, 1, 001.
- [12] Kim, S. M., & McCullough, B. F. (2003). Dynamic response of plate on viscous Winkler foundation to moving loads of varying amplitude. *Engineering Structures*, 25(9), 1179-1188.
- [13] Kim, S. M. (1996). *Dynamic response of pavement systems to moving loads*.
- [14] Taheri, M. R., Zaman, M. M., & Alvappillai, A. (1990). Dynamic response of concrete pavements to moving aircraft. *Applied Mathematical Modelling*, 14(11), 562-575.
- [15] Tompkins, D., Saxena, P., Khazanovich, L., & Gotlif, A. (2012). Modification of Mechanistic-Empirical Pavement Design Guide Procedure for Two-Lift Composite Concrete Pavements. *Transportation Research Record: Journal of the Transportation Research Board*, (2305), 14-23.
- [16] Ioannides, A. M., Khazanovich, L., & Becque, J. L. (1992). Structural evaluation of base layers in concrete pavement systems. *Transportation Research Record*, (1370).
- [17] Girhammar, U. A., & Gopu, V. K. (1993). Composite Beam - Columns with Interlayer Slip—Exact Analysis. *Journal of Structural Engineering*.
- [18] Strickland, D. (2001). Shell Pavement Design Software for Windows. *The Asphalt Yearbook 2001*.
- [19] Kruntcheva, M. R., Collop, A. C., & Thom, N. H. (2005). Effect of bond condition on flexible pavement performance. *Journal of Transportation Engineering*, 131(11), 880-888.
- [20] Hakim, B. A. (1997). *An improved backcalculation method to predict flexible pavement layers moduli and bonding condition between wearing course and base course* (Doctoral dissertation, Liverpool John Moores University).

- [21] Stoffels, S., Morian, D., Ioannides, A., Wu, S., Sadasivam, S., Yeh, L. and Yin H. (2008). Improved Overlay Design Parameters for Concrete Airfield Pavements, Innovative Pavement Research Foundation (IPRF) Project FAA-01-G-002-04-02.
- [22] Yeh, L. (2011). *Modified mechanistic-empirical airfield unbonded concrete overlay traffic prediction model* (Doctoral dissertation, The Pennsylvania State University).
- [23] Hall, K. T., Darter, M. I., Hoerner, T. E., & Khazanovich, L. (1997). *LTPP data analysis. Phase I: Validation of guidelines for K-value selection and concrete pavement performance prediction* (No. FHWA-RD-96-198).
- [24] SETIADJI, B. H. (2009). *Closed-form backcalculation algorithms for pavement analysis* (Doctoral dissertation).
- [25] Kausel, E., & Roësset, J. M. (1992). Frequency domain analysis of undamped systems. *Journal of Engineering Mechanics*.
- [26] Zhou H. Study on Dynamic Response of Structures and Ground Subjected to Moving Loads[D]. Hangzhou: Zhejiang University, 2005.
- [27] Singh, V. K. (2010). *Strain-Response Characterization for Unbonded Concrete Overlays Subjected to Heavy Aircraft Gear with Multiple Axles*(Doctoral dissertation, The Pennsylvania State University).
- [28] Burnham, T. (2004) Load Proximity Correlation of Dynamic Strain Measurements in Concrete Pavement, Proceedings of the 2nd international conference on Accelerated Pavement Testing, Minneapolis, Minn., Sep. 26-29, 2004.
- [29] Tarr, S. M., Okamoto P. A., Sheehan M. H., Packard R. G. (1999) Bond Interaction between Concrete Pavement and Lean Concrete Slab, *Transportation Research Record*, 1668, pp.9-17.
- [30] Gokhale, S., Byron, T., Iyer, S., and Choubane, B.(2009) Evaluation of Pavement Strain Gauge Repeatability, Results from Accelerated Pavement Testing, *Transportation Research*

*Record: Journal of the Transportation Research Board*, No. 2094, Transportation Research Board of the National Academies, Washington, D.C., 2009, pp.30–40.

[31] Gopalakrishnan, K., Thompson, M.R. (2006) Effect of Dynamic Aircraft Gear Loads on Asphalt Concrete Strain Responses, *Journal of ASTM International*, Vol. 3, No. 8, p 17.

[32] <http://www.airporttech.tc.faa.gov/Airport-Pavement/National-Airport-Pavement-Test-Facility-/NAPTF-Databases/Construction-Cycle-4>

[33] Hayhoe, G. F. (2002). *LEAF: A new layered elastic computational program for FAA pavement design and evaluation procedures* (pp. 1-15). Federal Aviation Administration.

[34] Nakamura, S. (1995). *Numerical analysis and graphic visualization with MATLAB*. Prentice-Hall, Inc..

[35] Shampine, L. F. (2008). Matlab program for quadrature in 2D. *Applied Mathematics and Computation*, 202(1), 266-274.

**NORTH**

X			Y		
EG-O-S1-1 B	338.83	17.58	LPT-O-N1-9	338.67	-11.83
EG-O-S1-2 B	363.92	17.87	LPT-O-N1-10	363.92	-11.75
EG-O-S1-3 B	376.33	17.88	LPT-O-N1-11	332.83	-6.25
EG-O-N1-2 B	363.918	-17.38	LPT-O-N1-12	345.25	-6.5
EG-O-N1-3 B	375.6	-17.67	LPT-O-N1-13	368	-6.42
LPT-O-N1-1	332.92	-28.17	LPT-O-N1-14	370.67	-7.25
LPT-O-N1-2	357.25	-29	LPT-O-S1-1	332.75	5.58
LPT-O-N1-3	320.42	-17.42	LPT-O-S1-2	369.67	5.58
LPT-O-N1-4	332.83	-17.42	LPT-O-S1-3	338.68	11.75
LPT-O-N1-7	369.67	-17.42	LPT-O-S1-4	363.83	11.5
LPT-O-N1-8	370.83	-17.58	LPT-O-S1-5	332.92	17.58
			LPT-O-S1-6	369.75	17.5

EG-O-S2-1 B	428.75	17.5	LPT-O-N2-11	428.83	-11.83
EG-O-S2-2 B	441.25	17.42	LPT-O-N2-12	466.17	-11.83
EG-O-S2-3 B	465.58	17.67	LPT-O-N2-13	423	-5.58
EG-O-N2-1 B	428.5	-17.67	LPT-O-N2-14	434.42	-5.58
EG-O-N2-2 B	441.92	-17.58	LPT-O-N2-15	435.5	-5.58
EG-O-N2-3 B	466.42	-17.58	LPT-O-N2-16	480.33	-5.58
LPT-O-N2-1	422.92	-28.17	LPT-O-N2-17	472.42	-5.5
LPT-O-N2-2	435.25	-29	LPT-O-S2-1	423.17	5.58
LPT-O-N2-3	460.17	-29	LPT-O-S2-2	435.58	5.58
LPT-O-N2-5	422.92	-17.42	LPT-O-S2-3	480.42	5.87
LPT-O-N2-6	434.33	-17.5	LPT-O-S2-4	428.92	11.5
LPT-O-N2-7	435.33	-17.58	LPT-O-S2-5	466.33	11.33
LPT-O-N2-8	459.08	-17.92	LPT-O-S2-6	423.08	17.71
LPT-O-N2-9	480.25	-17.92	LPT-O-S2-7	435.58	17.83
LPT-O-N2-10	472.25	-17.33	LPT-O-S2-8	460.42	17.58

EG-O-S3-1 B	518.83	17.5
EG-O-S3-2 B	543.67	17.58
EG-O-S3-3 B	566.08	17.67
EG-O-N3-1 B	518.83	-17.67
EG-O-N3-2 B	543.67	-17.58
EG-O-N3-3 B	566.08	-17.75
LPT-O-N3-1	512.75	-29
LPT-O-N3-2	537.92	-29
LPT-O-N3-4	512.83	-17.92
LPT-O-N3-6	537.25	-17.67
LPT-O-N3-7	537.83	-17.67
LPT-O-N3-8	549.83	-17.42
LPT-O-N3-9	518.83	-11.58
LPT-O-N3-10	544	-11.92
LPT-O-N3-11	513	-5.58
LPT-O-N3-13	537.75	-5.58
LPT-O-N3-14	548.67	-5.33
LPT-O-S3-1	512.75	5.87
LPT-O-S3-2	537.92	5.75
LPT-O-S3-3	518.67	11.67
LPT-O-S3-4	541.58	11.67
LPT-O-S3-5	512.83	17.33
LPT-O-S3-6	537.92	17.75

NORTH

OVERLAY 75' AT SIX 12' 6" INTERVALS	15'	OVERLAY 75' AT SIX 12' 6" INTERVALS	15'
-------------------------------------	-----	-------------------------------------	-----

**APPENDIX B**  
**STRAIN GAGE AND CALCULATED RESPONSES**

7/25/2006

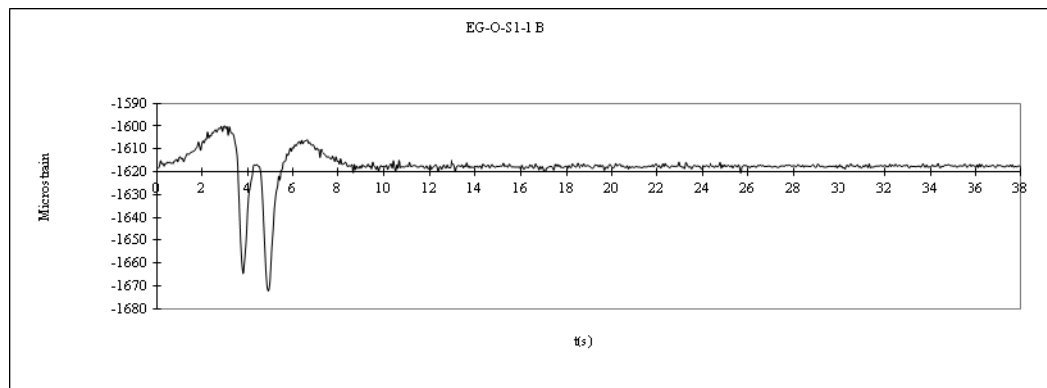


Figure B-1 Data of EG-O-S1-1 B, randomly selected track 0 pass on 7/25/2006 (embedded gage, overlay, test item S1, gauge 1, bottom of slab)

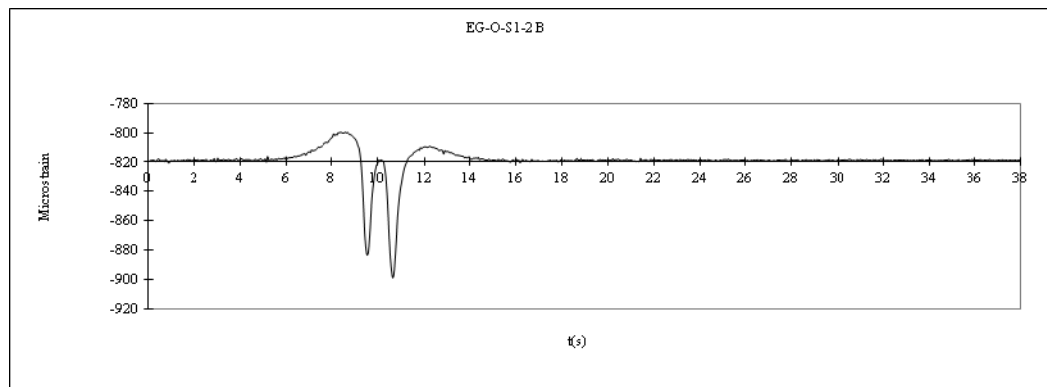


Figure B-2 Data of EG-O-S1-2 B, randomly selected track 0 pass on 7/25/2006 (embedded gage, overlay, test item S1, gauge 2, bottom of slab)

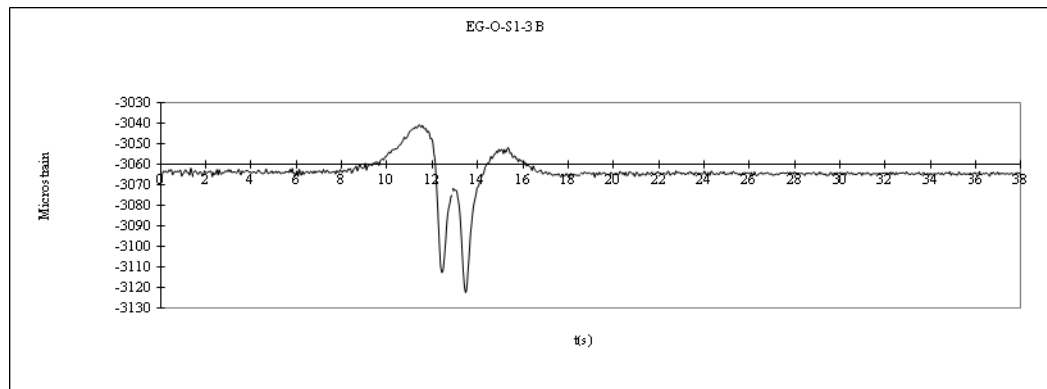


Figure B-3 Data of EG-O-S1-3 B, randomly selected track 0 pass on 7/25/2006 (embedded gage, overlay, test item S1, gauge 3, bottom of slab)

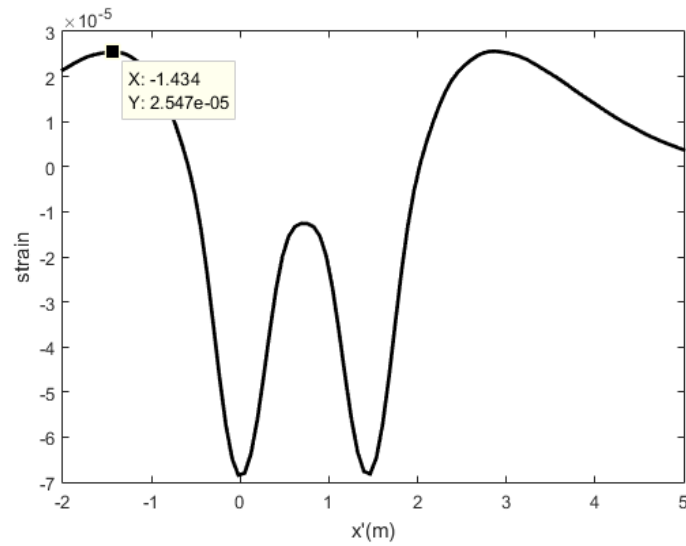


Figure B-4 Model Result of EG-O-S1, randomly selected track 0 pass on 7/25/2006 (embedded gage, overlay, test item S1, bottom of slab)

8/01/2006

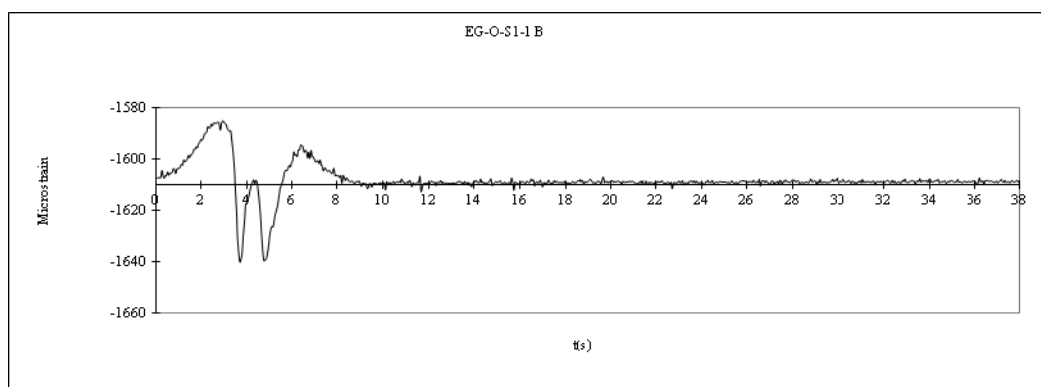


Figure B-5 Data of EG-O-S1-1 B, randomly selected track 0 pass on 8/01/2006 (embedded gage, overlay, test item S1, gauge 1, bottom of slab)

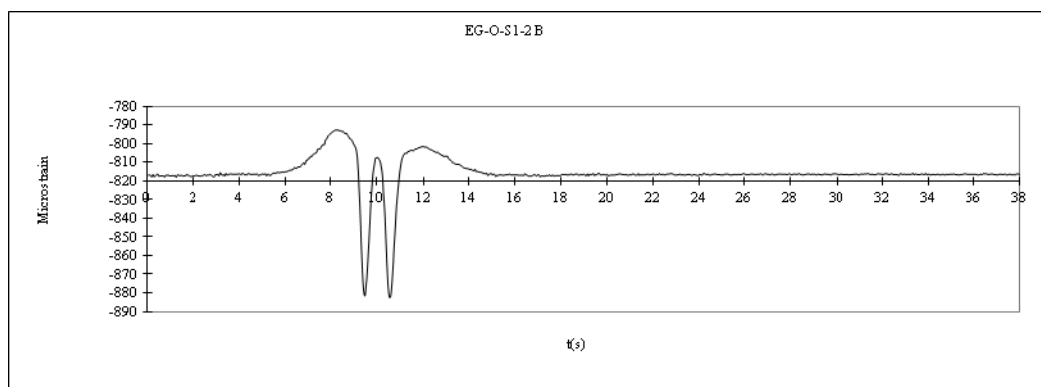


Figure B-6 Data of EG-O-S1-2 B, randomly selected track 0 pass on 8/01/2006 (embedded gage, overlay, test item S1, gauge 2, bottom of slab)

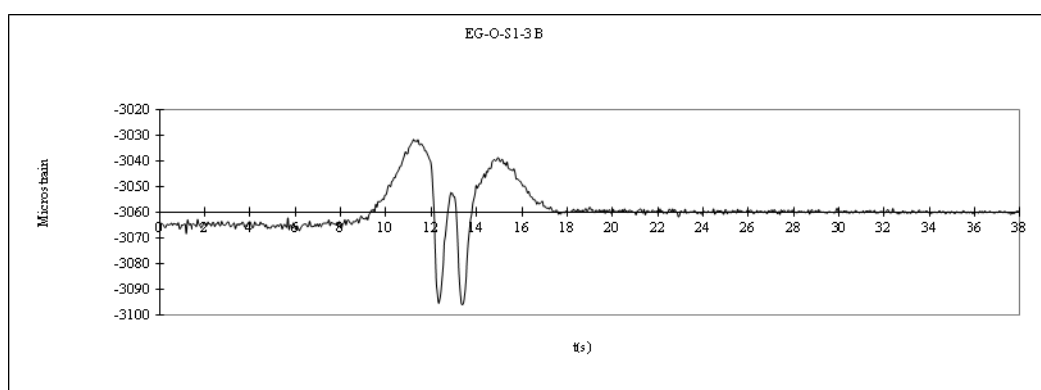


Figure B-7 Data of EG-O-S1-3 B, randomly selected track 0 pass on 8/01/2006 (embedded gage, overlay, test item S1, gauge 3, bottom of slab)



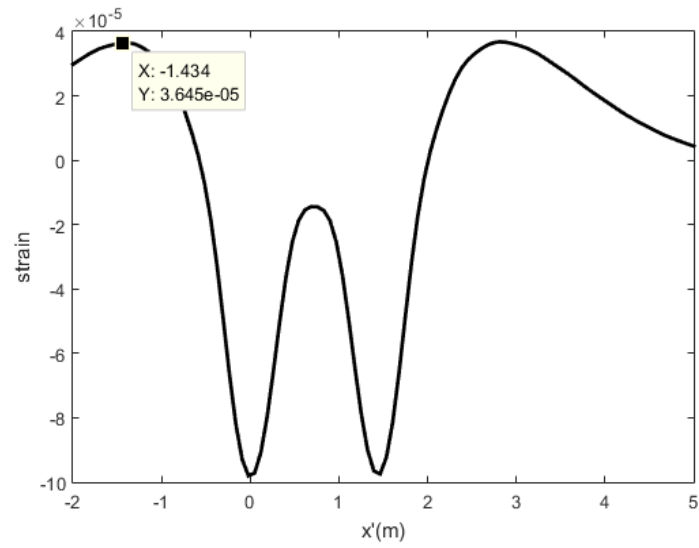


Figure B-8 Model Result of EG-O-S1, randomly selected track 0 pass on 8/01/2006 (embedded gage, overlay, test item S1, bottom of slab)

8/9/2006

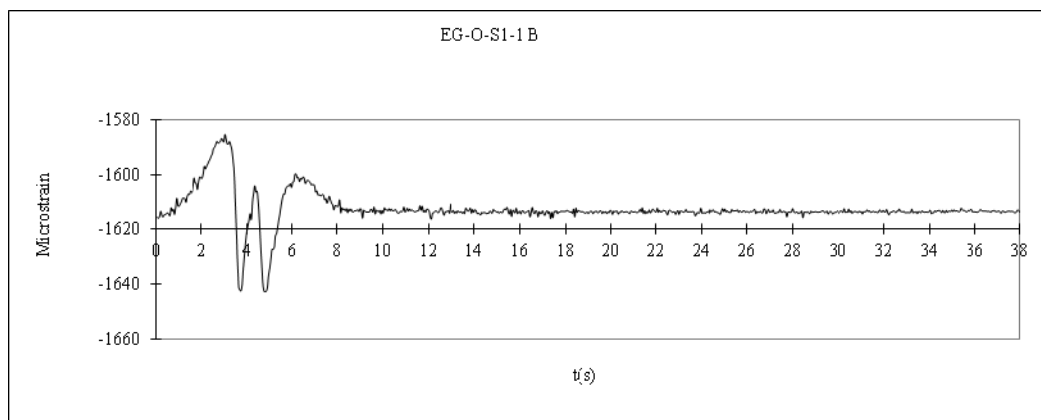


Figure B-9 Data of EG-O-S1-1 B, randomly selected track 0 pass on 8/09/2006 (embedded gage, overlay, test item S1, gauge 1, bottom of slab)

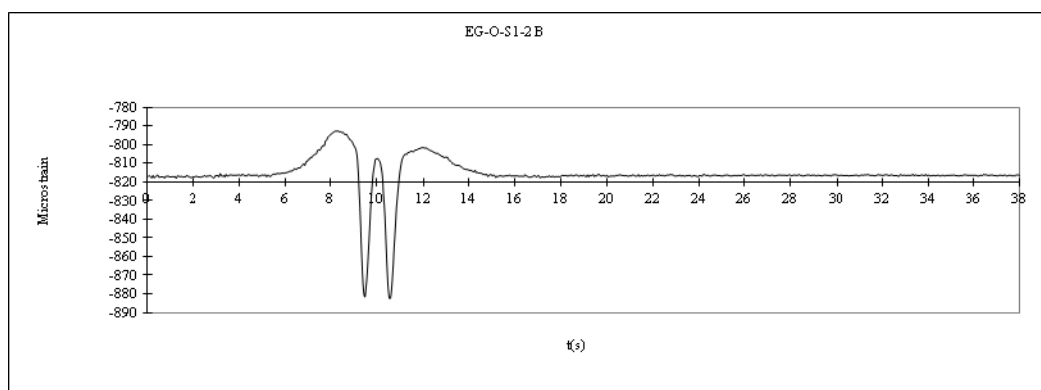


Figure B-10 Data of EG-O-S1-2 B, randomly selected track 0 pass on 8/09/2006 (embedded gage, overlay, test item S1, gauge 2, bottom of slab)

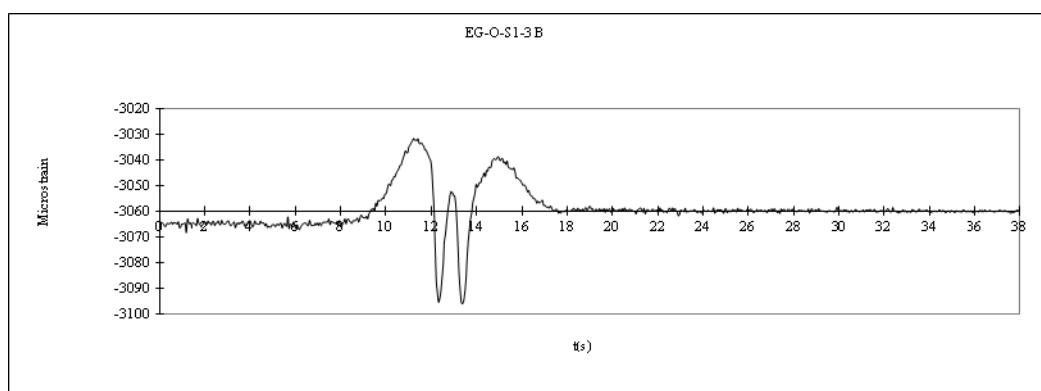


Figure B-11 Data of EG-O-S1-3 B, randomly selected track 0 pass on 8/09/2006 (embedded gage, overlay, test item S1, gauge 3, bottom of slab)

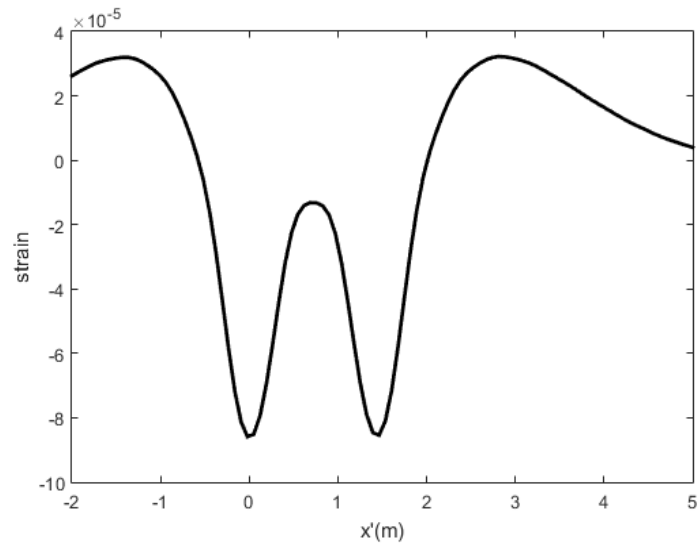


Figure B-12 Model Result of EG-O-S1, randomly selected track 0 pass on 8/09/2006 (embedded gage, overlay, test item S1, bottom of slab)

**APPENDIX C****STRAIN GAGE AND CALCULATED RESPONSES**

7/25/2006

N1

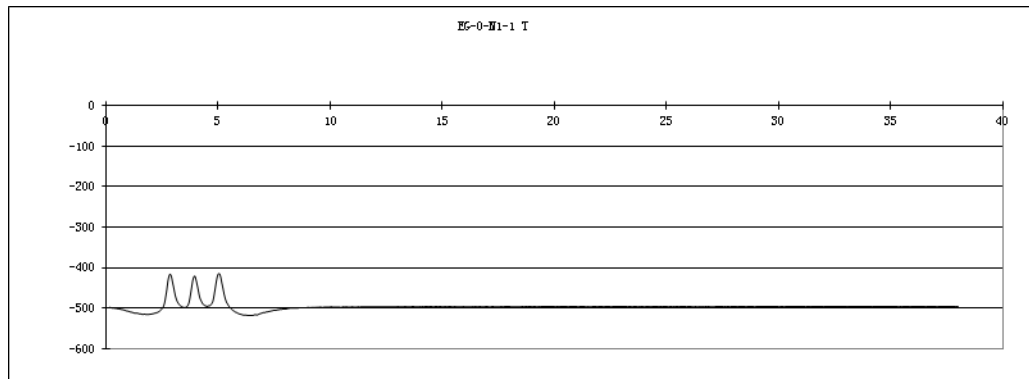


Figure C-1 Data of EG-O-N1-1 T, randomly selected track 0 pass on 7/25/2006 (embedded gage, overlay, test item N1, gauge 1, top of slab)

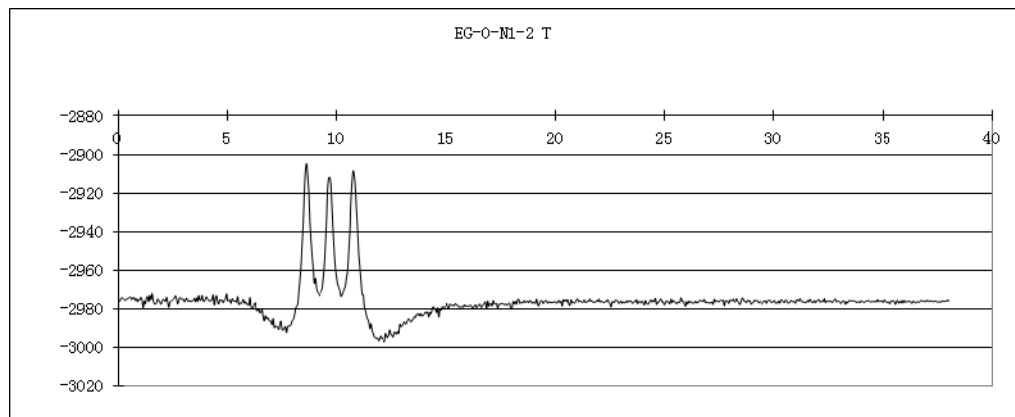


Figure C-2 Data of EG-O-N1-2 T, randomly selected track 0 pass on 7/25/2006 (embedded gage, overlay, test item N1, gauge 2, top of slab)

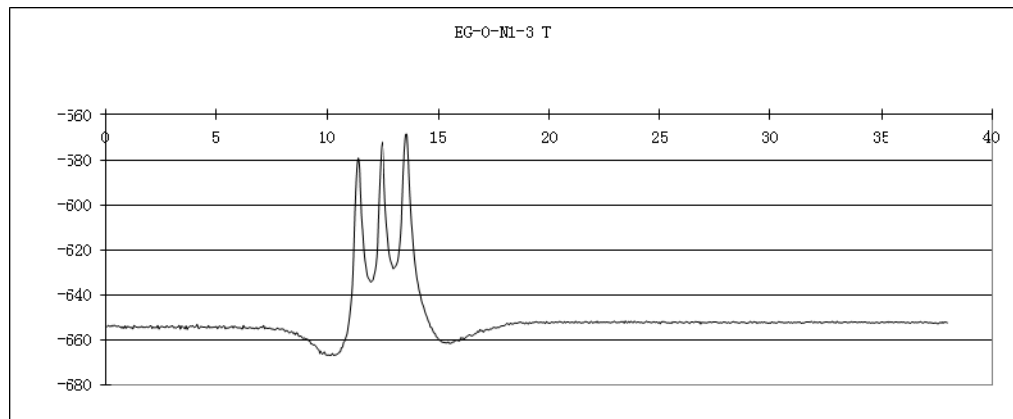


Figure C-3 Data of EG-O-N1-3 T, randomly selected track 0 pass on 7/25/2006 (embedded gage, overlay, test item N1, gauge 3, top of slab)

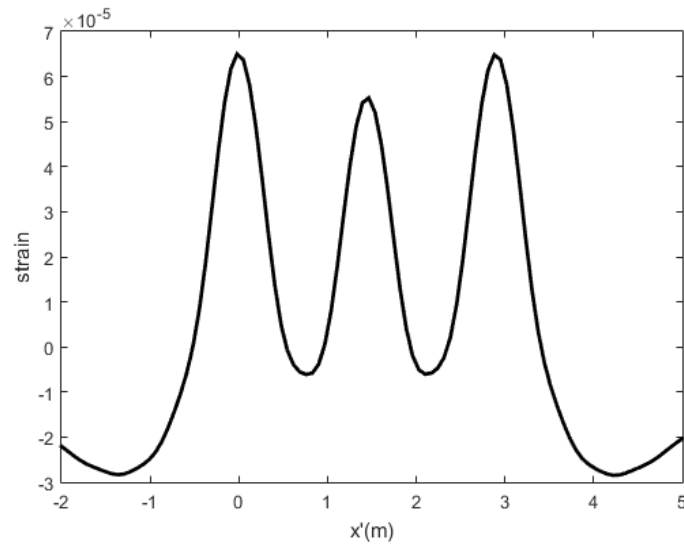


Figure C-4 Model Result of EG-O-N1, randomly selected track 0 pass on 7/25/2006 (embedded gage, overlay, test item N1, top of slab)

N2

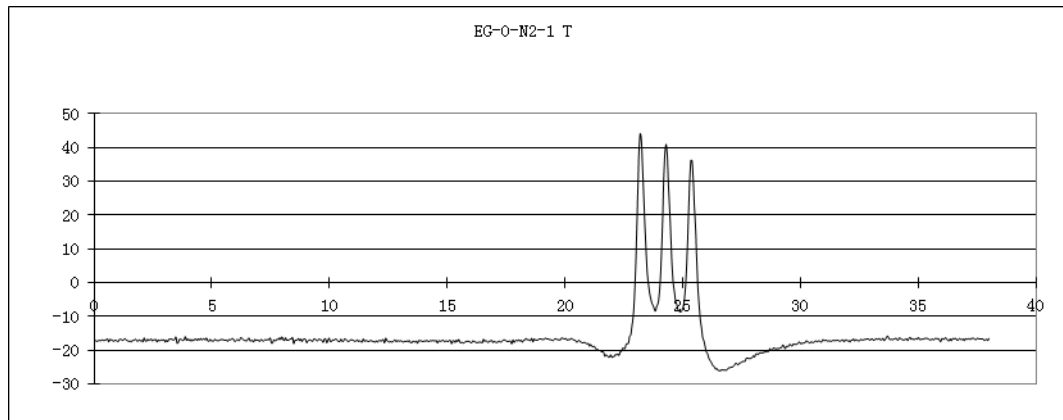


Figure C-5 Data of EG-O-N2-1 T, randomly selected track 0 pass on 7/25/2006 (embedded gage, overlay, test item N2, gauge 1, top of slab)

EG-O-N2-2 T data is random

EG-O-N2-2 T data is missed

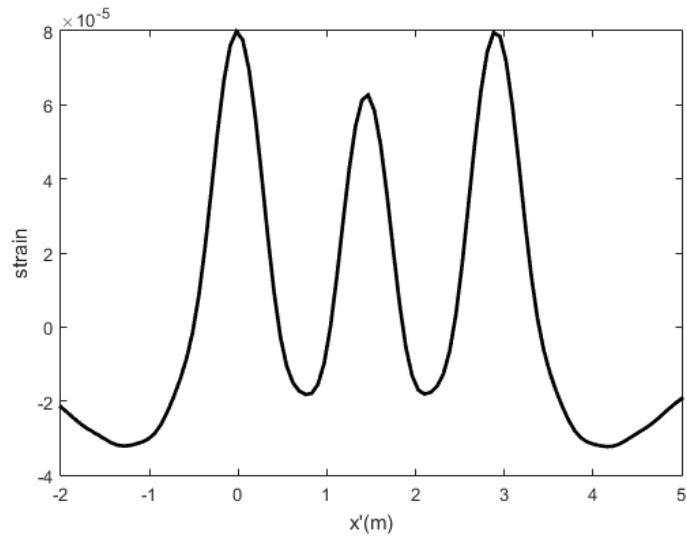


Figure C-6 Model Result of EG-O-N2, randomly selected track 0 pass on 7/25/2006 (embedded gage, overlay, test item N2, top of slab)

N3

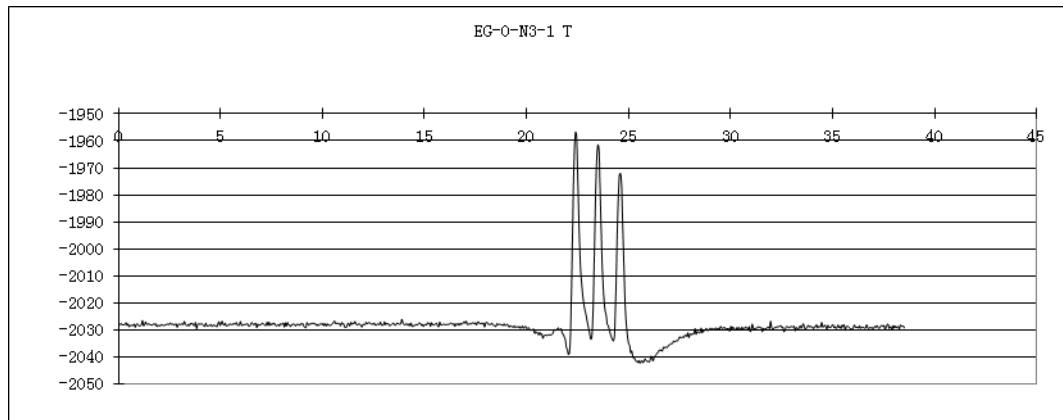


Figure C-7 Data of EG-O-N3-1 T, randomly selected track 0 pass on 7/25/2006 (embedded gage, overlay, test item N3, gauge 1, top of slab)

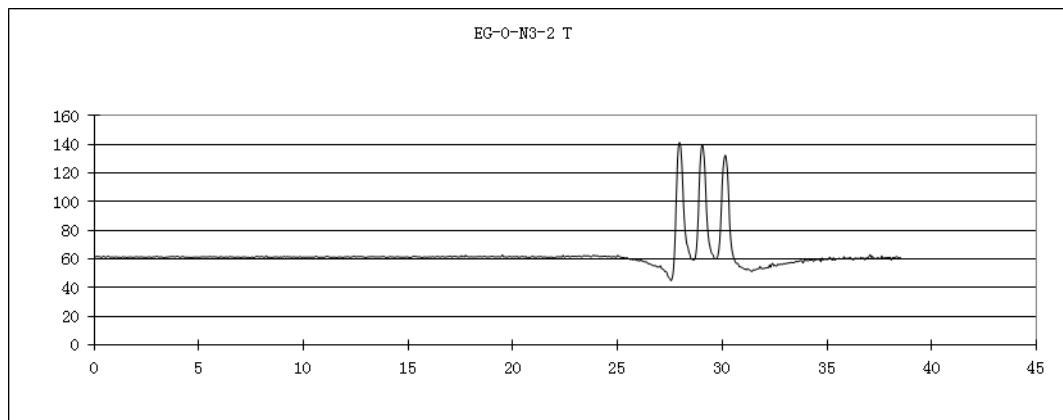


Figure C-8 Data of EG-O-N3-2 T, randomly selected track 0 pass on 7/25/2006 (embedded gage, overlay, test item N3, gauge 2, top of slab)

EG-O-N3-3 T data is missed

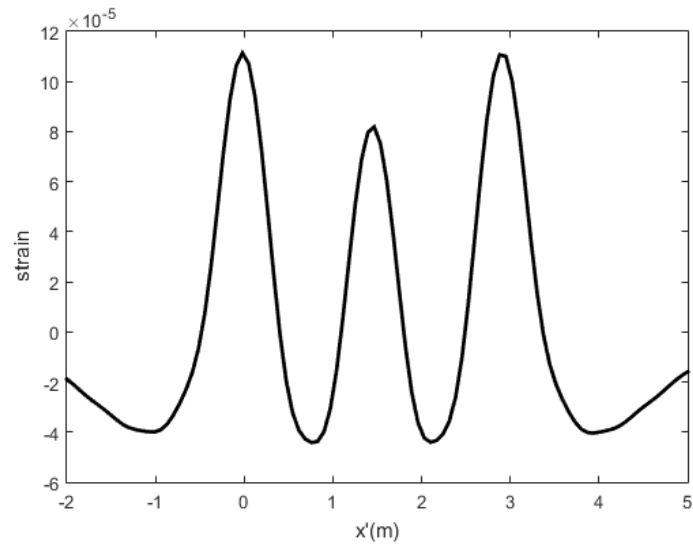


Figure C-9 Data of EG-O-N3, randomly selected track 0 pass on 7/25/2006 (embedded gage, overlay, test item N3, top of slab)



S1

EG-O-S1-1 T data is missed

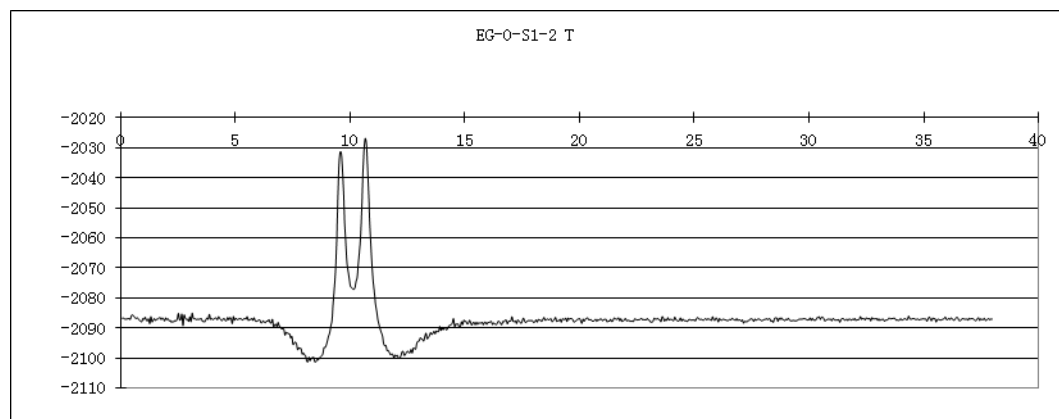


Figure C-10 Data of EG-O-S1-2 T, randomly selected track 0 pass on 7/25/2006 (embedded gage, overlay, test item S1, gauge 2, top of slab)

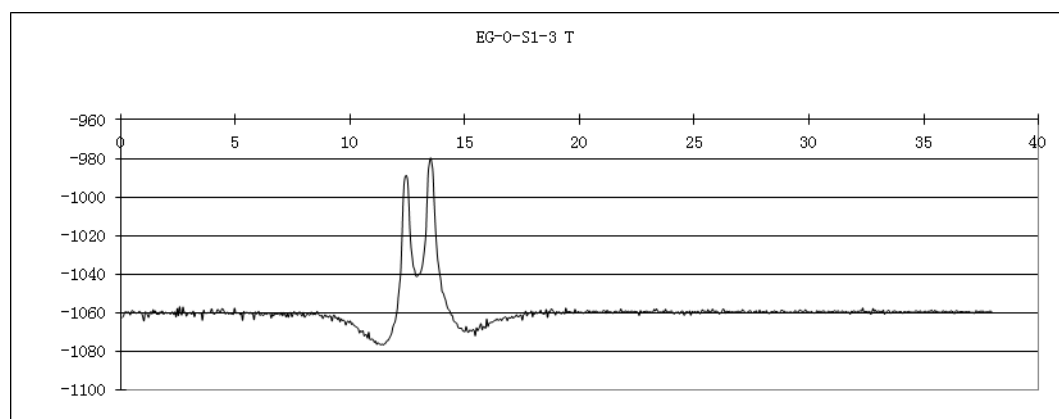


Figure C-11 Data of EG-O-S1-3 T, randomly selected track 0 pass on 7/25/2006 (embedded gage, overlay, test item S1, gauge 3, top of slab)

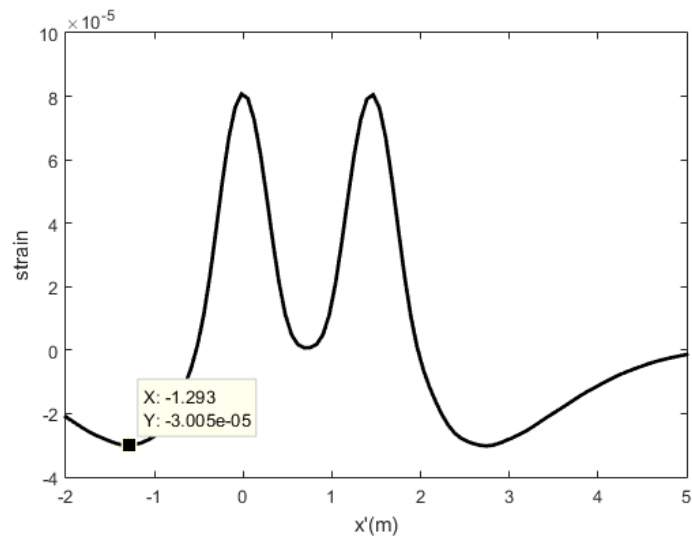


Figure C-12 Data of EG-O-S1, randomly selected track 0 pass on 7/25/2006 (embedded gage, overlay, test item S1, top of slab)

S2

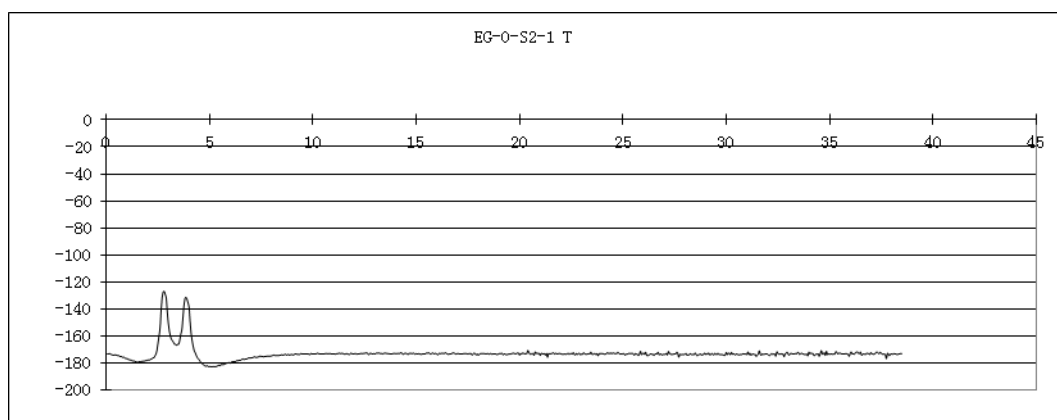


Figure C-13 Data of EG-O-S2-1 T, randomly selected track 0 pass on 7/25/2006 (embedded gage, overlay, test item S2, gauge 1, top of slab)

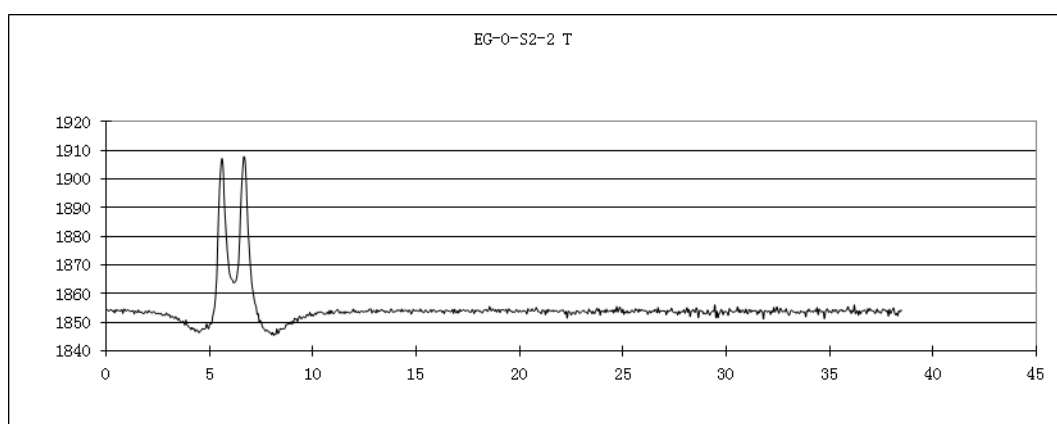


Figure C-14 Data of EG-O-S2-2 T, randomly selected track 0 pass on 7/25/2006 (embedded gage, overlay, test item S2, gauge 2, top of slab)

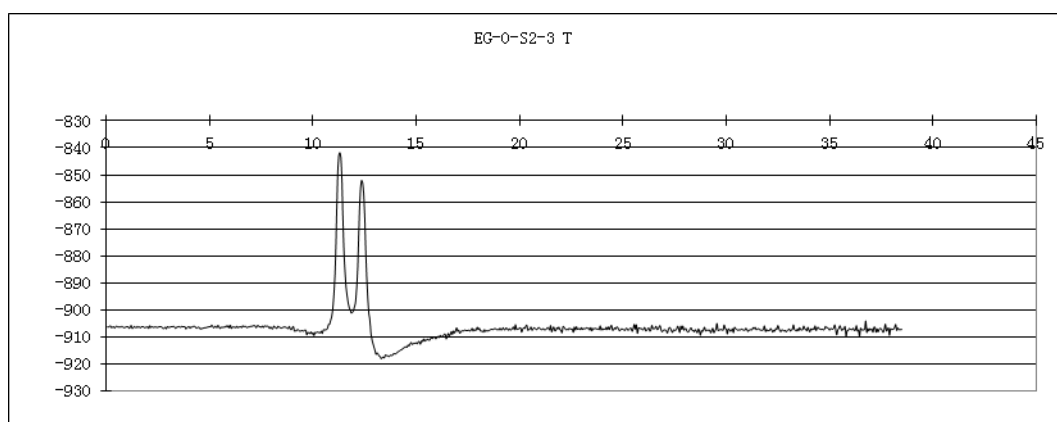


Figure C-15 Data of EG-O-S2-3 T, randomly selected track 0 pass on 7/25/2006 (embedded gage, overlay, test item S2, gauge 3, top of slab)

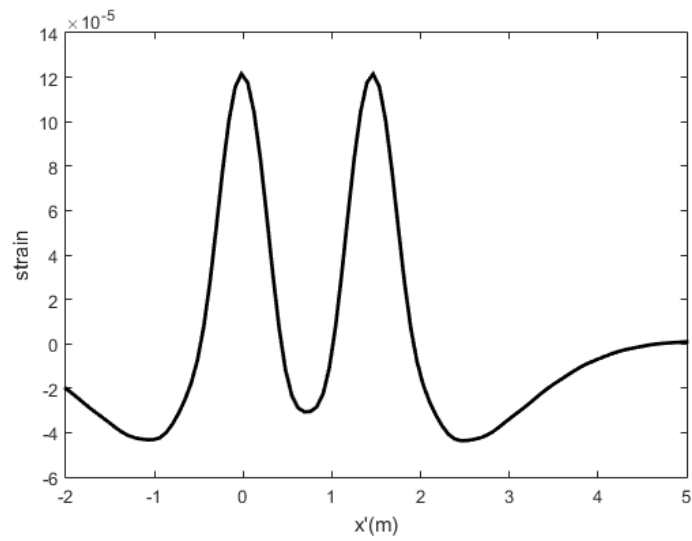


Figure C-16 Model Result of EG-O-S2, randomly selected track 0 pass on 7/25/2006 (embedded gage, overlay, test item S2, top of slab)

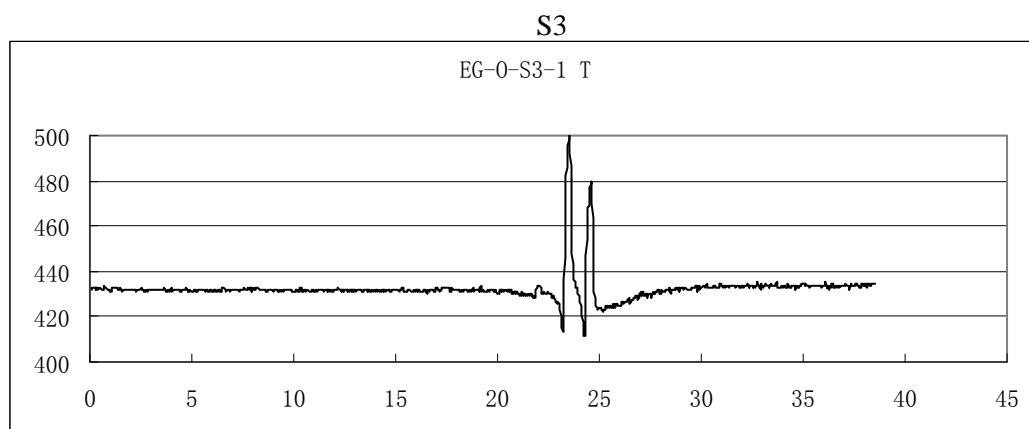


Figure C-17 Data of EG-O-S3-1 T, randomly selected track 0 pass on 7/25/2006 (embedded gage, overlay, test item S3, gauge 1, top of slab)

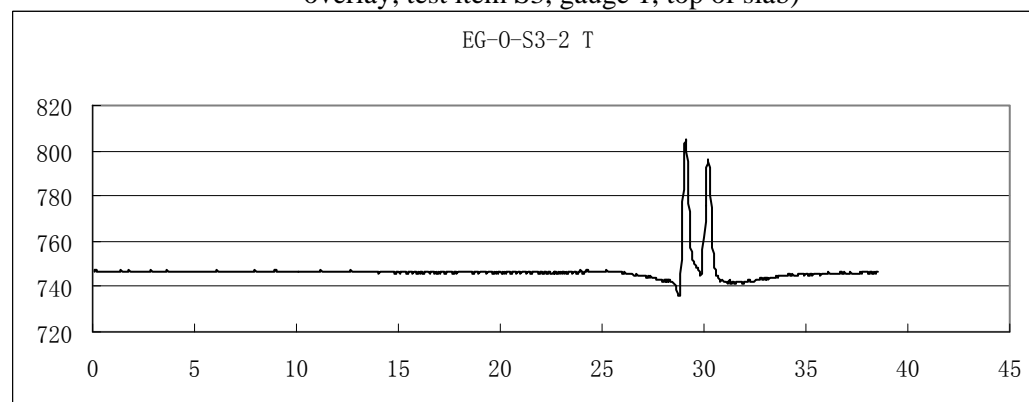


Figure C-18 Data of EG-O-S3-2 T, randomly selected track 0 pass on 7/25/2006 (embedded gage, overlay, test item S3, gauge 2, top of slab)

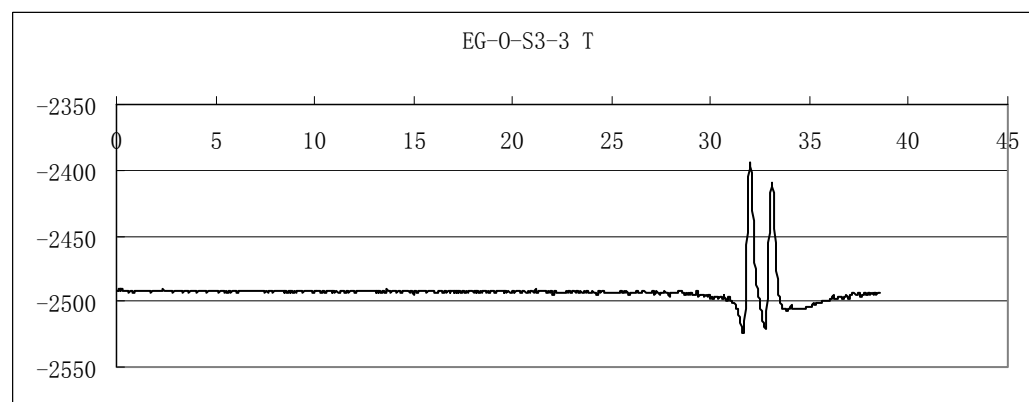


Figure C-19 Data of EG-O-S3-3 T, randomly selected track 0 pass on 7/25/2006 (embedded gage, overlay, test item S3, gauge 3, top of slab)

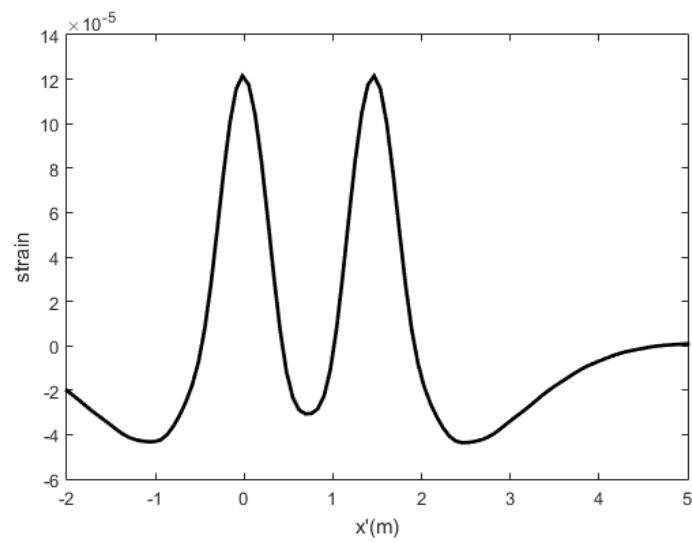


Figure C-20 Data of EG-O-S3, randomly selected track 0 pass on 7/25/2006 (embedded gage, overlay, test item S3, top of slab)

## APPENDIX D MATLAB CODE SAMPLE

```
%%%main function
```

```
xx=linspace(-2,5);
```

```
y=0;
```

```
y1=zeros(size(xx));
```

```
for ii=1:length(xx)
```

```
y1(ii)=kernal(xx(ii),y,1.0e+8,-15,15,-15,15);
```

```
end
```

```
plot(xx,y1)
```

```
%%%main function kernal
```

```
function w1=kernal(xx,y,Ks,c,d,e,f)
```

```
function W1=W1(Xi,k)
```

```
E1=4.14E+10; D1=36515228; D2=16813010;
```

```
h1=0.2179;h2=0.1605;V=1.341;m1=548.1818;
```

```
m2=387.7682;k1=9.48E+07;k2=7.60E+07;
```

```
l2=0.263144;da=1.4478;dt=0.263144;dw=1.3716;l1=0.263144;
```

```
P=-222411.024;z=0.5*h1;v1=0.15;
```

```
%E1=2.756E+10;v1=0.15;m1=708;h1=0.3048;Ks=0;V=11.11;P=-20E+3;%%%80KN
```

is the axle load

```
%D1=E1*h1^3/(12*(1-v1^2));
```

```

%l1=0.1778/2;l2=0.2032/2;dt=0.33;dw=1.88;da=1.32;D2=0;h2=0;m2=0;k1=136E+6;k
2=1;z=0.5*h1;

a=D1*(Xi.^2+k.^2).^2-(h1^2/4)*Ks*(Xi.^3+k.^3)*1i-m1*V^2*X1.^2+k1;

b=D2*(Xi.^2+k.^2).^2+(h2^2/4)*Ks*(Xi.^3+k.^3)*1i-m2*V^2*X1.^2+k2;

q=a.*b-(h1^2*h2^2/16)*Ks^2*(Xi.^3+k.^3).^2;

%North item

F=2*pi*P*sin(l2*k).*sin(l1*Xi).*(1+exp(-1i*da*Xi)+exp(-2i*da*Xi)).*(1+exp(-
1i*dt*k)+exp(-1i*dw*k)+exp(-1i*(dt+dw)*k))./(l1*l2*Xi.*k);

%South item

%F=2*pi*P*sin(l2*k).*sin(l1*Xi).*(1+exp(-1i*da*Xi)).*(1+exp(-1i*dt*k)+exp(-
1i*dw*k)+exp(-1i*(dt+dw)*k))./(l1*l2*Xi.*k);

%% W1=F.*b.*exp(1i*xx.*Xi).*exp(1i*y.*k)./(8*pi^3*q);

W1=-z/(1-v1^2)*((Xi.^2+v1*k.^2)-
v1*(v1*Xi.^2+k.^2)).*F.*b.*exp(1i*xx.*Xi).*exp(1i*y.*k)./(8*pi^3*q);

end

w1=integral2(@W1,c,d,e,f);

end

```